UNIVERSIDADE FEDERAL DO CEARÁ
CENTRO DE TECNOLOGIA
DEPARTAMENTO DE ENGENHARIA ELÉTRICA
PROGRAMA DE PÓS-GRADUAÇÃO EM ENGENHARIA ELÉTRICA

PAULO DAVING LIMA DE OLIVEIRA

INTELLIGENT MPP TRACKER FOR PHOTOVOLTAIC SYSTEMS UNDER UNIFORM IRRADIANCE AND PARTIAL SHADING CONDITIONS

FORTALEZA

2018

PAULO DAVING LIMA DE OLIVEIRA

INTELLIGENT MPP TRACKER FOR PHOTOVOLTAIC SYSTEMS UNDER UNIFORM IRRADIANCE AND PARTIAL SHADING CONDITIONS

Dissertação apresentada ao Programa de Pós-Graduação em Engenharia Elétrica da Universidade Federal do Ceará, como requisito parcial à obtenção do título de Mestre em Engenharia Elétrica. Área de concentração: Sistemas de Energia Elétrica.

Orientador: Prof. Arthur Plínio de S. Braga, Dr.
Coorientador: Prof. Fabrício G. Nogueira, Dr.

FORTALEZA

2018

Dados Internacionais de Catalogação na Publicação
Universidade Federal do Ceará
Biblioteca Universitária
Gerada automaticamente pelo módulo Catalog, mediante os dados fornecidos pelo(a) autor(a)

O49i Oliveira, Paulo Daving Lima de.
Intelligent MPP tracker for photovoltaic systems under uniform irradiance and partial shading conditions / Paulo Daving Lima de Oliveira. – 2018. 118 f. : il. color.

Dissertação (mestrado) – Universidade Federal do Ceará, Centro de Tecnologia, Programa de Pós-Graduação em Engenharia Elétrica, Fortaleza, 2018.

Orientação: Prof. Dr. Arthur Plínio de Souza Braga.
Coorientação: Prof. Dr. Fabrício Gonzalez Nogueira.

1. Sistemas Fotovoltaicos. 2. Rastreador de PMP. 3. Sombreamento Parcial. I. Título

CDD 621.3

PAULO DAVING LIMA DE OLIVEIRA

INTELLIGENT MPP TRACKER FOR PHOTOVOLTAIC SYSTEMS UNDER UNIFORM IRRADIANCE AND PARTIAL SHADING CONDITIONS

Master's dissertation presented to the Post-Graduate Program in Electrical Engineering of the Federal University of Ceará as partial requirement for the degree of Master in Electrical Engineering. Concentration area: Electrical Energy Systems.

Approved in September 26th, 2018.

EXAMINATION BOARD

Prof. Dr. Arthur Plínio de Souza Braga (Advisor)
Federal University of Ceará (UFC)

Prof. Dr. Fabrício Gonzalez Nogueira (Co-advisor)
Federal University of Ceará (UFC)

Prof. Dr. Paulo Peixoto Praça
Federal University of Ceará (UFC)

Prof. Dr. Paulo César Marques de Carvalho
Federal University of Ceará (UFC)

Prof. Dr. João Paulo Pordeus Gomes
Federal University of Ceará (UFC)

To academics, engineers, technicians and those with substantial interest in the elementary yet valuable understanding of photovoltaics.

ACKNOWLEDGEMENTS

First of all, I would like to express my sincere apologies in advance for any person, group, entity or institution I come to forget mentioning in these concise acknowledgement words. It is clearly improbable that such a significant effort could be performed all alone, thus I wish to thank everyone who devoted time or any other resource to help me with this accomplishment.

A special thank to my advisor, Prof. Arthur, whose dedication, guidance, mentoring and incontrovertible trust enabled this research path to be followed. To my co-advisor, Prof. Fabrício, my gratitude for the valuable contributions to both academic and personal fields of life. To both of you I am also thankful for the noble effort in helping me with my application for the master program of the electrical engineering department two years ago.

Additional thanks go to Prof. Paulo Carvalho and Ivonne Dupont from the Alternative Energies Laboratory whose solicitude is worth noting and whose help has allowed my research to go further. I also thank Prof. Paulo Praça for dedicating a slot of his time to provide me with relevant information with which I could take my research on. To all professors that I am glad to have met at the Research Group of Automation, Control and Robotics, my exceptional thank for the great time we shared, for the lessons learned, for the advices taken and, specially, for the availability I often took advantage of. I would not forget to thank Prof. Laurinda and Prof. Antônio Barbosa for the unmeasurable determination in helping me with my first conference publication.

My gratitude is also directed to all friends and colleagues whose personal, professional and scientific contributions I will take permanently through my lifetime. For all the times, conversations and fun we had together, for all technical and personal assistance each one of them somehow provided me with, and for the friendship and successful partnership we built, the alphabetically ordered list to which I give many thanks would include, but not constrains to: Adriano de Paula, Clauson Rios, Darielson Souza, Élio Segundo, Fábio Lobo, Félix Eduardo, Herivelton Alves, Jéssica Pessoa, Juliana Sobral, Magno Prudêncio, Marcus Davi, Marcus Vinicius, Renan Fonteles, René Olimpio, Silas Alysson, Stephanie Braga and Thiago Lima. For those I did not mention, I honestly apologize and kindly ask them to refer to the first paragraph of this text.

I have been searching for the right words to express my eternal gratitude for everything my family indiscriminately did for me, specially for the past couple of years, but all I have left was the words available in the English dictionary which can only vaguely describe the sentiment. For the inexhaustible attention, generosity, support and care, my everlasting gratefulness to my mother, Francisca. Despite the fact that she can barely comprehend what is being said in these lines with this weird language, I am positive that she can perfectly understand the feelings behind them. These very same feelings are the essence of my gratitude to my sisters, Poly and Paty, who also supported me through distinct times, strengthening our relationship, and reinforcing the concepts of fraternity. A special gratitude to Poly, who put her health at risk to recover mine and without whom I could not be writing these words at this moment. I am also grateful to my brother-in-law, José Ailton, for the attention devoted to me when no one else could do. I can not fail to thank my other brother-in-law, Wantier, for his countless assistances through all the years he has been part of my family. And to my beloved seven-year-old nephew, Marcos Paulo, I express my warm gratitude for all the time we enjoy together that allows me to continuously rediscover the pleasure in playing again. I also wish to thank my father, Davino, whose trust and investment in my education represented a substantial contribution to my edification.

I cannot but offer my heartfelt thanks to my girlfriend and partner, Révia, with whom I shared diverse and intense moments down this road. Her contributions extend far beyond the boundaries of an intimate relationship, reaching unexpected fields of life. I truly appreciate her care and confidence throughout these years, specially at those moments I could not correspond to the same extent.

Last, but not least, I would like to express my gratitude to CAPES for the financial aid available for the last two years which enabled the accomplishment of this research. This gratitude is also extendible to the Brazilian politicians who diligently believe in education – and the free access to it – as the only tool for the nation and human progress.

This study was financed in part by the Coordenação de Aperfeiçoamento de Pessoal de Nível Superior - Brasil (CAPES) - Finance Code 001.

“*We make our world significant by the courage of*
our questions and by the depth of our answers.”

Carl Sagan (‘Cosmos’, 1985)

RESUMO

Os sistemas fotovoltaicos de conversão de energia solar são uma alternativa de geração energética bastante atraente, uma vez que a fonte de energia – o recurso solar – está disponível abundantemente. Dado que o perfil de irradiância solar e a temperatura ambiente variam consideravelmente ao longo do dia, para que tais sistemas possam operar de maneira eficiente emerge a necessidade de realizar o seguimento do ponto de máxima potência (PMP) utilizando instrumentos dotados de algoritmos concebidos para esse fim. Nesse contexto, técnicas convencionais encontradas nos sistemas comercializados atualmente atingem esse objetivo de forma satisfatória quando todo o sistema fotovoltaico está submetido a condições uniformes de irradiância e temperatura. No entanto, esses algoritmos se revelam falhos nas situações em que há irregularidade na distribuição de irradiância nos componentes do sistema devido principalmente ao surgimento de sombras, forçando a operação do sistema fotovoltaico em um ponto de potência não máximo. Adicionalmente à baixa eficiência, o sombreamento parcial dos componentes pode provocar a inoperância do sistema conversor, sendo, portanto, um fenômeno cuja mitigação é de elevada importância. Para impedir que as células e/ou módulos fotovoltaicos sejam danificados quando submetidos a tal adversidade, diodos de passagem são inseridos na composição dos circuitos de associação. A presença desses diodos modifica a curva tensão versus potência (curva P-V) do arranjo fotovoltaico, revelando múltiplos pontos máximos, dentre os quais o desejado ponto global de máxima potência (PMP global). A proposta aqui apresentada consiste em oferecer um algoritmo baseado em inteligência computacional que seja capaz de rastrear o PMP tanto nas condições de irradiância uniforme como nas de sombreamento parcial. Devido à característica compacta do algoritmo proposto, a implementação do sistema rastreador inteligente é bastante adequada a dispositivos de processamento sequencial de baixo custo. Resultados de simulação apontam a relevante capacidade do sistema em rastrear o PMP, seja único ou global, em diversas condições de irradiância e temperatura.

Palavras-chave: Sistemas Fotovoltaicos. Rastreador de PMP. Sombreamento Parcial.

ABSTRACT

Photovoltaic systems for solar energy conversion are an attractive alternative in energy generation since the energy source – the solar resource – is widely available. Once the solar irradiance profile and the ambient temperature considerably vary along the daytime, for such systems to operate efficiently it becomes necessary to track the maximum power point (MPP) employing instruments that run algorithms conceived to this end. In this context, conventional techniques found in commercial tools nowadays perform this task satisfactorily when the entire photovoltaic system is subject to uniform irradiance and temperature conditions. Nevertheless, these algorithms reveal their drawbacks in the situations where irregular irradiance distribution occurs in the components of the system due mostly to the emergence of shadows, forcing the system to operate in a suboptimal power point. In addition to the lower efficiency, partial shading of the components may disrupt the conversion system, being, thereby, a phenomenon whose mitigation is of prominent importance. To avoid damaging the photovoltaic cells and/or modules when subject to such impairment, bypass diodes are inserted into the connection circuits of the components. The existence of these diodes modifies the power versus voltage curve (P-V curve) of the photovoltaic array, revealing multiple maxima, among which the desired global maximum power point (global MPP). The proposal herein presented consists in providing a computational intelligence-based algorithm that is capable of tracking the MPP at either uniform irradiance or partial shading conditions. Due to the compactness of the proposed algorithm, the implementation of the intelligent tracking system is highly suitable for low-cost serial processing devices. Simulation results point out the relevant ability of the system in tracking the MPP, being it unique or global, for several irradiance and temperature conditions.

Keywords: Photovoltaic systems. Intelligent MPPT. Partial Shading.

LIST OF FIGURES

LIST OF TABLES

ACRONYMS

a-Si	Amorphous Silicon [cells]
ABSOLAR	Associação Brasileira de Energia Solar
AC	Alternating Current
AM	Air Mass
ANFIS	Adaptive Neuro-Fuzzy Inference System
ANN	Artificial Neural Networks
BIPV	Building-Integrated Photovoltaics
c-Si	Crystalline Silicon [cells]
CCM	Continuous Conduction Mode
CdTe	Cadmium Telluride [cells]
CIGS	Copper Indium Gallium Selenide [cells]
CIS	Copper Indium Selenide [cells]
CPV	Concentrating Photovoltaics
CSP	Concentrating Solar Power
CZTS	Copper Zinc Tin Sulfide
DC	Direct Current
DCM	Discontinuous Conduction Mode
DE	Differential Evolution
DRCC	Digital Ripple Correlation Control
EHP	Electron-Hole Pair
EIA	U.S. Energy Information and Administration
FF	Fill Factor
FL	Fuzzy Logic
FPA	Flower Pollination Algorithm
FPGA	Field-Programmable Gate Array
GA	Genetic Algorithm
GaAs	Gallium Arsenide [cells]
GaInAs	Gallium Indium Arsenide [cells]
GaInAsP	Gallium Indium Arsenium Phosphide [cells]
GaInP	Gallium Indium Phosphide [cells]
GMPP	Global Maximum Power Point

HC	Hill Climbing
HCE	Heat Collection Element
IEA	International Energy Agency
I-V	Current versus Voltage [curve]
IncCond	Incremental Conductance
InGaAs	Indium Gallium Arsenide [cells]
InGaP	Indium Gallium Phosphide [cells]
InP	Indium Phosphide [cells]
LEA	Laboratório de Energias Alternativas
LMPP	Local Maximum Power Point
MPP	Maximum Power Point
MPPT	Maximum Power Point Tracker
mRMO	Modified Radial Movement Optimization
nc-Si	Nanocrystalline Silicon [cells]
NOCT	Normal Operating Cell Temperature
P-V	Power versus Voltage [curve]
P&O	Perturb and Observe
PSC	Partial Shading Condition
PSO	Particle Swarm Optimization
PV	Photovoltaic
PWM	Pulse Width Modulation
RMO	Radial Movement Optimization
TOPV	Transparent Organic Photovoltaic [cells]
UIC	Uniform Irradiance Condition

TABLE OF CONTENTS

1 INTRODUCTION

Renewable energy sources are those possessing the natural capability of replenishment or that are able to regenerate on the human timescale standpoint. According to U.S. Energy Information and Administration (EIA, 2017a), the most usual renewable energy sources are:

- Biomass: Energy stored in organic matter available from plants and animals;
- Hydropower: Energy available from moving water;
- Geothermal: Energy available from earth's inner heat;
- Wind: Energy available from moving air masses;
- Solar: Thermal and photovoltaic (PV) energies available from the sun.

Concerning the last source, solar thermal energy is that used for heating up fluids or environments, whilst photovoltaic solar energy relates to the photoelectric effect which converts sunlight into electricity. Other renewable sources with recent increase in capacity are marine energies, which include tidal, wave and ocean thermal energy (WORLDENERGY; OURWORLDINDATA, 2017).

1.1 Renewable Energies Outlook

All these sources of energy, together with the non-renewable nuclear power, are said to be alternative energy sources as they contrast the dominant fossil fuels, which include coal, oil and natural gas, historically the most used sources of energy. Figure 1.1 presents the yearly global energy consumption from fossil fuels for the past 20 years.

Figure 1.1 – Yearly global consumption, in terawatt-hours (TWh), for all fossil fuels.

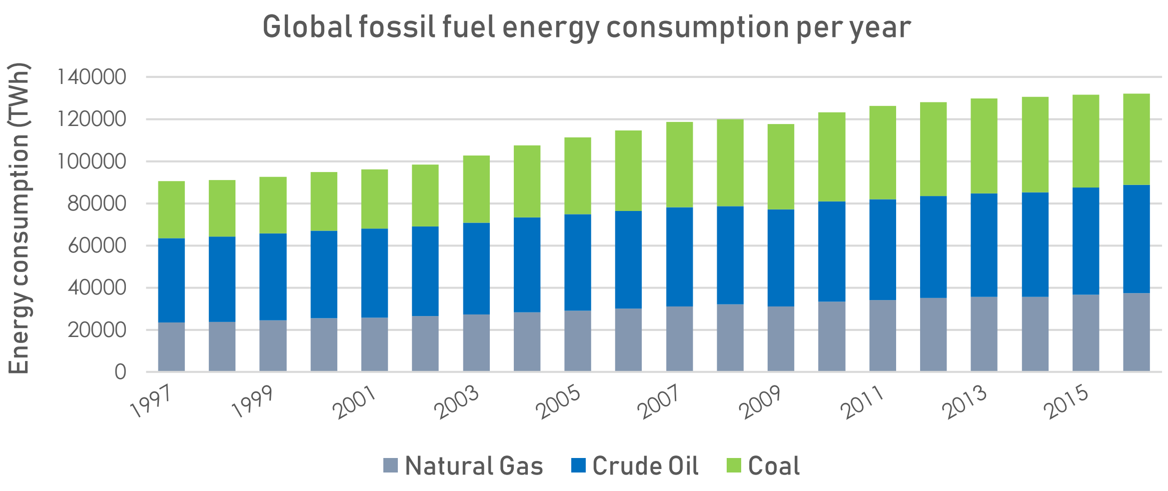

Source: Adapted from https://ourworldindata.org/fossil-fuels.

With less usage indices when compared to fossil fuels, renewable sources have shown an increasing consumption pattern over the past 20 years, except for traditional biofuels such as ethanol and biodiesel which show a slight drop, as depicted in Figure 1.2.

Figure 1.2 – Yearly global consumption, in terawatt-hours (TWh), for renewable sources. Traditional biofuels include ethanol and biodiesel. Other sources relate to modern biofuels, geothermal, wind, solar PV, and marine.

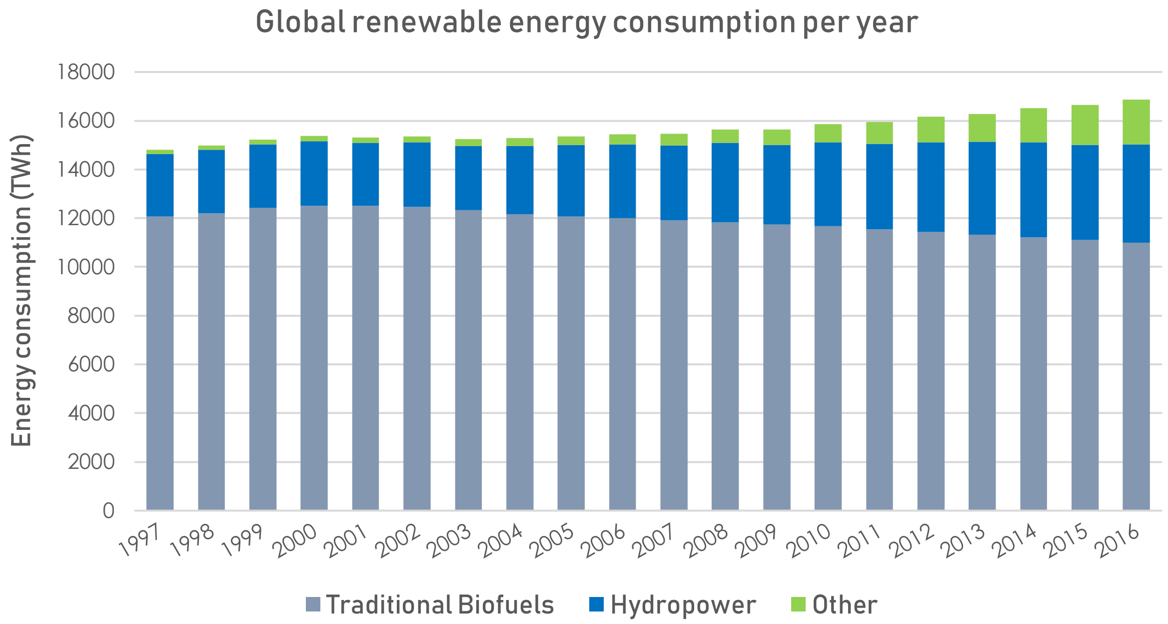

Source: Adapted from https://ourworldindata.org/renewables.

Biofuels, as seen, remain the largest energy source up to the moment. In contrast, when relating to electricity generation, hydropower plays a leading role against all other renewable sources, as noticeable from Figure 1.3.

Figure 1.3 – Global share of total electricity production from renewables. Other sources include solar PV, wind (onshore and offshore), geothermal and biomass.

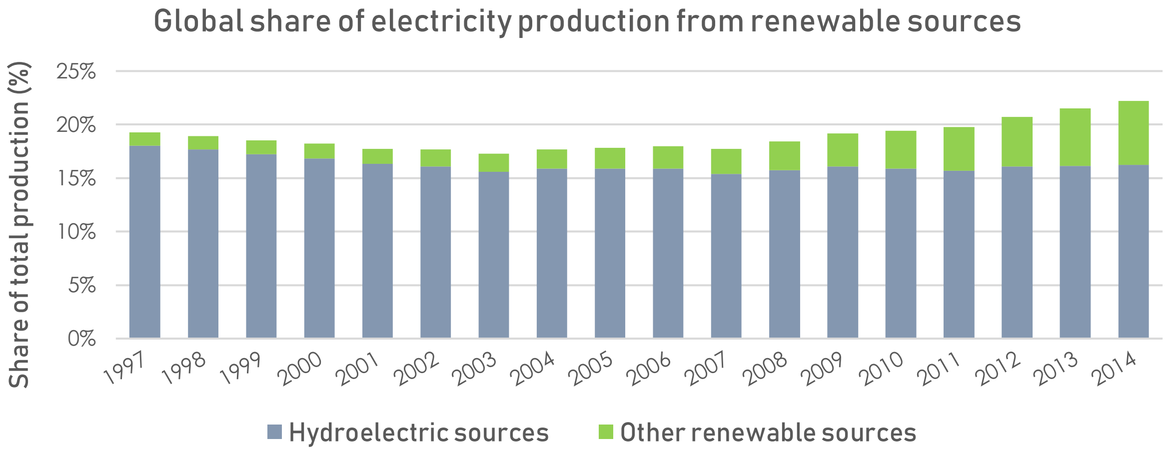

Source: Adapted from https://ourworldindata.org/renewables.

It is seen from the chart in Figure 1.3 that renewable energies are revealing an increasing trend in their share of electricity production worldwide. The International Energy Agency's 2017 report (IEA, 2017) brings the capacity increase, in gigawatts, for the main renewable sources. Their study also shows an optimistic forecast for the period 2017-2022. Figures 1.4 and 1.5 illustrate this information.

Figure 1.4 – Historical increase in electricity capacity, measured in gigawatts (GW), for renewable energy sources. IEA's forecast for the period 2017-2022 is led by the record performance of 2016.

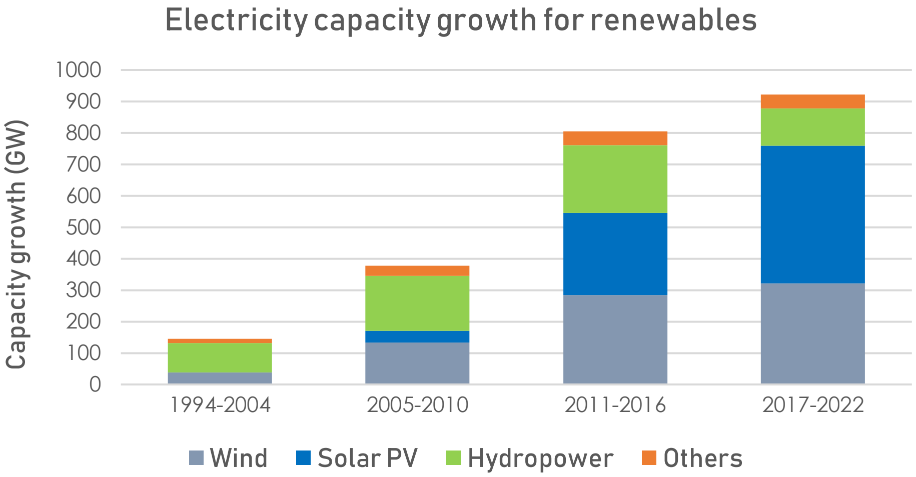

Source: Adapted from https://www.iea.org/publications/renewables2017/.

Figure 1.5 – Comparison of the recent capacity additions, in gigawatts (GW), for traditional fossil fuels and the growing renewables.

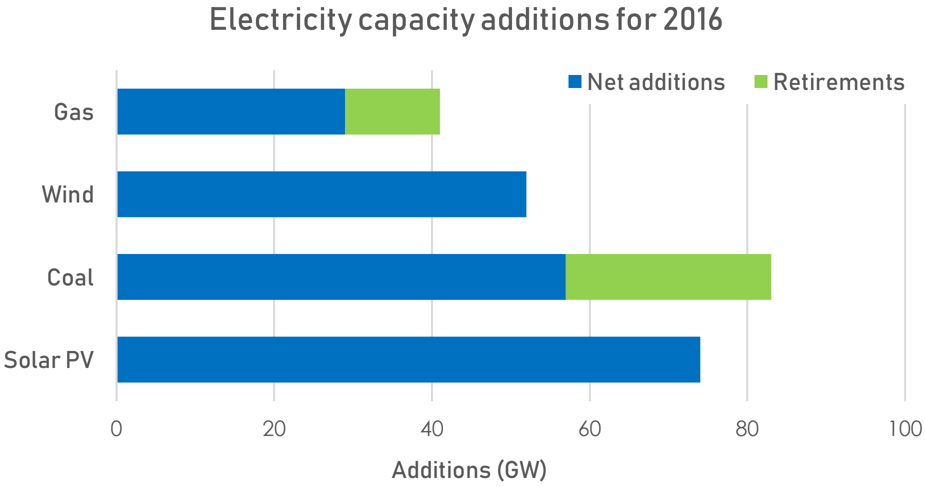

Source: Adapted from https://www.iea.org/publications/renewables2017/.

Considering local investments on renewables, Figure 1.6 shows that China is leading the world, which is probably due to its extensive policy support and market improvement, representing half of the global solar PV demand and component manufacturing capacity as well.

Figure 1.6 – Recent capacity growth, in gigawatts, by country/region. IEA's forecast for the period 2017-2022 is led by the record performance of 2016.

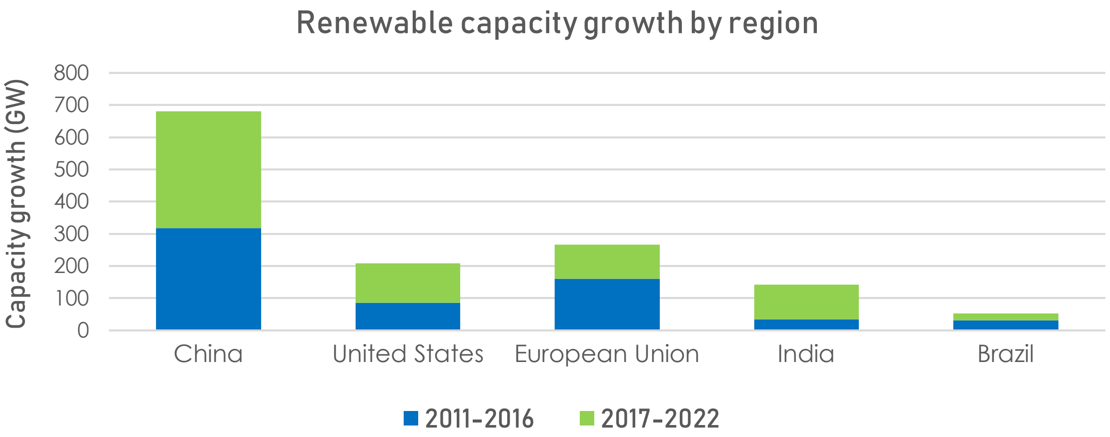

Source: Adapted from https://www.iea.org/publications/renewables2017/.

In the context of solar photovoltaic energy, a rhetorical question emerges: Is the label "alternative" still suitable for such renewable source? Governed by intense and continuous cost reductions and global policy support, and proven by the data in Figure 1.5, solar PV represents the largest annual capacity increase which could be driving an imminent outgrowth.

Even though Brazil exhibits a moderate, and maybe unpretentious[1], renewable energy program, it is reasonable to note its substantial increase in demand for solar PV energy for the past years, as seen in Figure 1.7.

Figure 1.7 – Yearly solar photovoltaic energy consumption, in gigawatt-hours, in Brazil.

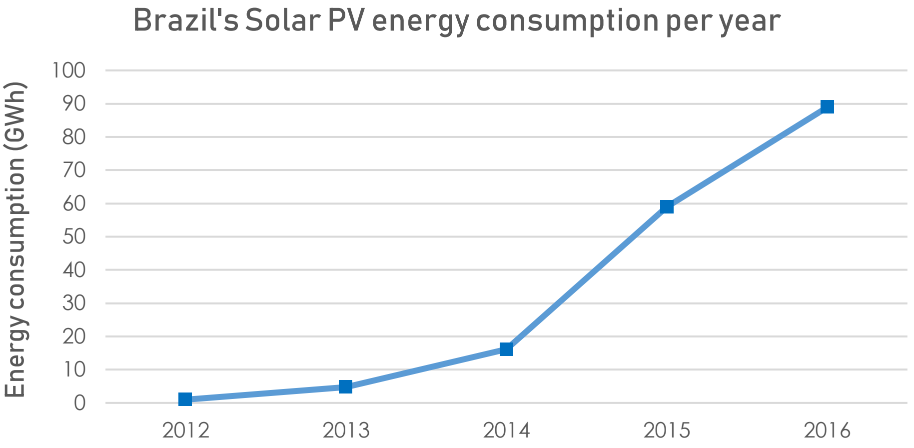

Source: Adapted from https://ourworldindata.org/renewables.

Brazil follows the global trend in boosting the solar PV market, with installed

---

[1] When compared to global leaders in the solar market as China, United States, Germany and India, with energy capacities ranging from 10 to 80 times greater than Brazil's, as of 2016 (OURWORLDINDATA, 2017).

capacity reaching the 1 GW range as of the early 2018 (ABSOLAR, 2018). Its first solar PV farm was installed in 2012, in the northeast state of Ceará, and rapid growth has been observed since then, especially in the southeast region. Although late, Brazil's investment in the solar PV sector has been driven continuously and is probably due to the same reasons that triggered all other countries to dive deep into this promising market: the global effort in reducing greenhouse gas emissions and increase the diversification of energy sources; intense government support and incentives; and continuous technology cost reductions that made solar PV attractive to industrial, commercial and residential sectors (IEA; OURWORLDINDATA, 2017). Regarding cost reductions, Figure 1.8 brings the historical drop in solar photovoltaic module prices, measured in US$ per watt-peak[2].

Figure 1.8 – Yearly solar photovoltaic module prices measured in 2016 US dollar per watt-peak.

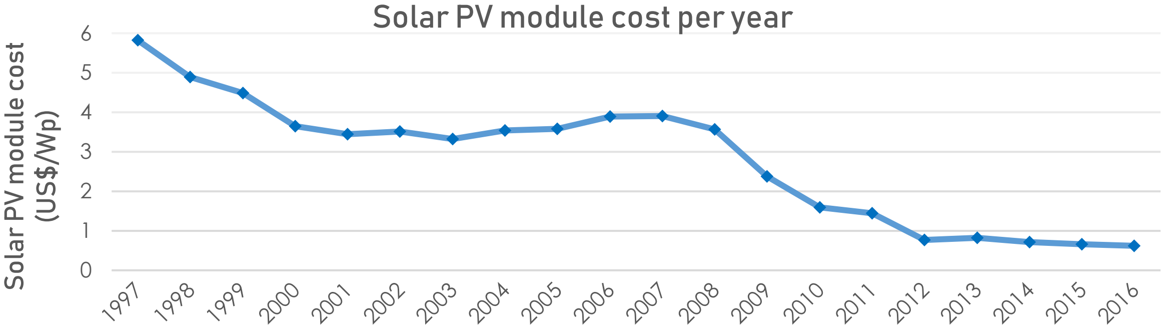

Source: Adapted from https://ourworldindata.org/renewables.

As an essentially clean and renewable energy source, along with a 10-fold decline in component costs within 2 decades, solar PV energy conversion systems become progressively attractive to meet – economically and environmentally – the modern society demands. This, in addition to the global upward trend of the demand and supply of solar PV energy, underpins IEA's optimistic previsions for the next five years, reflecting the worldwide movement towards an even more carbon-constrained future.

1.2 Motivation

While the panorama, as seen from the previous pages, portrays a strong acceptance and widespread usage of photovoltaics, technological maturity is still in progress. The solar resource reveals regular unavailability and is not precisely predictable along the time it becomes available. Furthermore, photovoltaic cells – the basic units that convert sunlight into electricity – have relatively low efficiency when compared to other sources of energy, regardless of the

---

[2] Watt-peak (Wp) is the nominal energy flow that a PV component can supply under standard test conditions.

technology employed for the cell production. Table 1.1 relates the main PV cell/module[3] technologies and their efficiencies.

Table 1.1 – Cell/module efficiencies for different technologies measured under standard test conditions.

	Technology	Efficiency (%)		Technology	Efficiency (%)
Cells	**Silicon**		***Modules***		
	Si (crystalline)	26.7		Si (crystalline)	24.4
	Si (multicrystalline)	22.3			
	a-Si (amorphous)	10.2			
	GaInP/GaAs/Si (multijunction)	35.9		Si (multicrystalline)	19.9
	GaInP/Si (multijunction)	32.8			
	III-V Semiconductors				
	GaAs (multicrystalline)	18.4		GaAs (thin film)	25.1
	InP (crystalline)	24.2			
	5 junctions	38.8			
	InGaP/GaAs/InGaAs (multijunction)	37.9		CIGS (thin film)	19.2
	GaInP/GaAs (multijunction)	32.8		CdTe (thin film)	18.6
	Thin Film				
	CIGS	21.7			
	CdTe	21.0		Organic	8.7
	CZTS	10.0			
	a-Si/nc-Si/nc-Si (multijunction)	14.0		InGaP/GaAs/InGaAs	31.2
	a-Si/nc-Si (multijunction)	12.7			
	Other Classes				
	Perovskite	20.9		**With Concentrator Optics**	
	Die sensitized	11.9			
	Organic	11.2		Si	20.5
	Perovskite/Si (multijunction)	23.6			
	With Concentrator Optics				
	Si	27.6			
	GaAs	29.3		Si (large area)	21.7
	CIGS (thin film)	23.3			
	GaInP/GaAs (multijunction)	46.0			
	GaInAsP/GaInAs (multijunction)	46.0		Three junction (3j)	35.9
	GaInP/GaAs/GaInAs (multijunction)	45.7			
	InGaP/GaAs/InGaAs (multijunction)	44.4		Four junction (4j)	38.9
	GaInAsP/GaInAs (multijunction)	35.5			

Source: Adapted from (GREEN *et al.*, 2017).

---

[3] A photovoltaic module, or popularly known as solar panel, is a series/parallel packaged assembly of photovoltaic cells.

It is observed from Table 1.1 that module efficiencies do not reach 40% even with top-ranked technologies such as III-V multijunction cells with concentrator optics. Actually, the most commercially available solar PV modules have efficiencies ranging from 5% to 15% according to (EIA, 2017b).

Apart from relatively low efficiencies obtained from cells/modules, terrestrial solar PV conversion systems are susceptible to weather conditions, e.g., cloudy days severely reduces the input solar irradiance and, hence, the output power. Moreover, PV systems are not uncommonly installed on rooftops and walls, specially in residential applications, and this leads to another issue: full/partial shading due to surrounding buildings, trees, or any other object.

Another noteworthy topic is the operating point of the solar PV conversion systems. Since irradiance and temperature unpredictably change through daytime, the operating point must be continuously adjusted so to extract the maximum power from the solar panels under variable conditions. This characteristic is similarly present in wind energy systems, where wind speed and availability are the uncertain sources (OLIVEIRA JUNIOR, 2016).

Addressing such issues is intrinsically related to making solar PV an economically viable energy source. Technological enhancements in cell manufacturing have allowed both improved conversion efficiencies and reduced cost productions, as pointed out by (GREEN *et al.*, 2017). Engineering strategies such as 1- or 2-axis sun trackers (SRI VASTAV *et al.*, 2016; AL NABULSI *et al.*, 2012) and panel cleaning/cooling systems (WABLE *et al.*, 2017; SULAIMAN *et al.*, 2018) help extracting most of the energy that is possible from solar modules. Sun trackers enhance the input irradiance by continuous- and optimally pointing the panels towards the sun in the course of the day. Cleaning and cooling systems prevent panels from accumulating dust and from overheating. Dust and high cell temperatures have negative impacts on the extracted power (NDIAYE *et al.*, 2013). Distinct array[4] topologies have recently been proposed in order to mitigate shading effects, specially over large solar farms (BELHAOUAS *et al.*, 2017). Last, but not least, maximum power point tracking systems (MPPTs) have always represented a strong concern for industry and academia once they are conceived to pursue the best operating point of the conversion system.

Historically, conventional MPPTs dominate the solar power industry, with a myriad of brands and vendors available worldwide. Their effectiveness, however, dramatically decreases as soon as partial shading starts occurring. In light of that, it has been long studied

---

[4] A photovoltaic array is a series/parallel assembly of photovoltaic modules.

MPPT techniques/algorithms that could successfully overcome the problem of tracking the optimal operating point under such a challenging and unavoidable condition. And it is in this context that computational intelligence techniques, specifically evolutionary/swarm-based algorithms, attempt to provide a solution for the MPPT problem, as can be seen in section 2.4.

1.3 Objectives: General and Specific

Based on the aforementioned circumstances, it becomes essentially important to propose and investigate tools, techniques and strategies that are capable of delivering efficiency improvements to solar photovoltaic energy systems.

This work focuses on the investigation of a maximum power point tracking algorithm based on computational intelligence theories that, differently from conventional MPPTs, is able to detect the global optimal operating point when shading phenomena occur. To pursue that, a fast swarm-based evolutionary algorithm is assessed in its original proposal as well as in a modified version specifically targeted to the MPPT problem.

It is also an interest of this research work to provide the fundamentals on photovoltaic systems and their associated challenges concerning partial shading conditions. With current widespread usage of terrestrial solar PV energy systems, it is imperative to address such a stochastic phenomenon so that optimal operation is achieved. A dedicated chapter will treat the underlying theory of photovoltaics with a special subsection for the partial shading effect. It is expected that this approach will help students, engineers and any other professional in better understanding the solar photovoltaic area.

1.4 Methodology

As a first approach, a theoretical review is going to be presented to both provide the fundamentals on the research object and to also discuss the current scope of the scientific community towards MPPT in photovoltaic systems.

Radial Movement Optimization (RAHMANI & YUSOF, 2014) – a stochastic swarm-based optimization algorithm – is discussed along with other similar techniques heavily adopted in the literature. Their implementation is evaluated on MATLAB software tool using several captured profiles of operating conditions. Performances are then compared in order to validate the proposed algorithm, both its original and modified versions.

Conventional MPPT techniques, such as Perturb&Observe (P&O) and Incremental Conductance (IncCond), are also exercised to provide a baseline for comparison with the proposed intelligent tracker system. It is expected that under partial shading conditions, the later behaves accordingly, detecting and setting the operating point to the global optimal one with minimum failure indices.

Online operation of the proposed algorithm is going to be assessed using the simulation environment of Simulink. Real-world input data are employed to observe how the algorithm behaves under natural and varying weather conditions. This assessment is also compared to the classical P&O algorithm subjected to the same conditions. These real-world data refer to irradiance and temperature profiles captured from the solar PV plant available at the Alternative Energies Laboratory of the Federal University of Ceará, during March 2018. This approach is supposed to highlight the possible contributions of the proposed algorithm against conventional methods under real operating conditions.

1.5 Text Organization

This research work is divided into six main chapters, each of which are going to be further explained as follows.

The first chapter provides a broad outlook of the solar photovoltaic energy around the world and particularly in Brazil. The aim is to locate the reader into the current perspectives and challenges of the subject, and also indicate what motivated this research.

A deeper yet concise theory review is going to be presented in the second chapter along with the state-of-the-art in MPPT techniques for photovoltaics. This helps formalizing the problem that is addressed in this work. Chapter 3 details about intelligent optimization algorithms that are commonly used in a variety of applications, namely Particle Swarm Optimization and Differential Evolution algorithms. The recently proposed Radial Movement Optimization is also discussed in its general – and original – proposal.

The modified version of the intelligent algorithm, targeted to maximum power point tracking of photovoltaic systems, is introduced in chapter 4. Its implementation and integration in the whole simulated system is also presented. The simulation results for the offline and online test approaches are provided in the fifth chapter.

Concluding observations from the attained results and potential future works are presented in the final chapter. These conclusions and guidelines might help other research efforts towards efficiency improvement of solar photovoltaic energy systems, a constantly sought activity to guarantee operational and economic viability.

2 THEORY AND LITERATURE REVIEW ON PHOTOVOLTAICS

The solar energy can be harnessed in diverse ways. According to (IPCC, 2012), direct solar energy technologies are divided into four main groups, namely (*i*) solar thermal; (*ii*) solar photovoltaic; (*iii*) concentrating solar power (CSP); and (*iv*) solar fuel. Among these, the ones involved in electricity generation are the solar photovoltaic and CSP. This research work focuses only in the former, while the latter is shortly defined in the footnote of this page[5].

At this point, the reader has already been introduced to the broad panorama of renewable energies around the world and the promising insertion of the solar photovoltaic into the mainstream sources. As such, the idea behind this chapter is to briefly present the fundamentals on photovoltaics so to provide the background for a proper comprehension of the object under investigation.

After discoursing on the photovoltaic theory, the reader will be exposed to the literature review on recent and some legacy techniques for tracking the maximum power point in solar PV systems. This helps enlightening what are the contemporary directions of the academic research on the matter and where the present work stands.

2.1 Solar Photovoltaic Energy

Comprehending solar photovoltaic energy conversion systems implies basically understanding the properties of sunlight, the physics behind the conversion from the solar to the electrical form of energy, and how solar cells and other components work.

2.1.1 The Solar Resource

The power from the sun represents a clean, intense, and unlimitedly available energy source. As a matter of fact, the sun indirectly generates most of the other energy sources on earth (PINHO *et al.*, 2014). Roughly speaking, winds are a product of the differences in temperature and pressure over the surface of seawater and land. In turn, evaporation originates the water cycle that involves precipitation and the consequent creation of water reservoirs. Fossil fuels are plant and animal residuals that once developed using the sun as their energy source. Finally, it is through photosynthesis that organic materials use the solar resource to

---

[5] Concentrating solar power (CSP) technologies harness the energy from the sun to generate heat. High temperatures, ranging from 400 to 1000 °C, can be achieved, and this heat is then used to drive an electrical generator, e.g., a steam turbine. They employ parabolic reflectors that concentrate the solar irradiation onto a heat-collection element (HCE). Further details can be found in (IPCC, 2012).

develop and posteriorly turn into biofuels.

With its surface temperature of about 5778 K, the sun generates its energy by the nuclear reaction that converts Hydrogen into Helium, and this energy is radiated uniformly in all directions in compliance to Planck's blackbody radiation formula (DI PIAZZA, 2013):

$$W_\lambda = \frac{2\pi hc^2}{\lambda^5\left(e^{\frac{hc}{\lambda kT}} - 1\right)}. \tag{2.1}$$

Eq. (2.1) relates the power density, expressed in W/m², for all wavelengths (λ) that compose the sunlight spectrum, where h is the Planck's constant and is equal to 6.63x10^{-34} J.s; k is the Boltzmann's constant equal to 1.38x10^{-23} J/mol.K; c is the speed of light valued at 3x10^{8} m/s; and T is the blackbody temperature in Kelvin. Figure 2.1 shows the extraterrestrial blackbody spectrum available on the top of the Earth's atmosphere.

Figure 2.1 – Extraterrestrial blackbody spectrum with additional AM 1 (air mass = 1) spectrum after atmospheric absorption/scattering effects and its cumulative power density for all wavelengths.

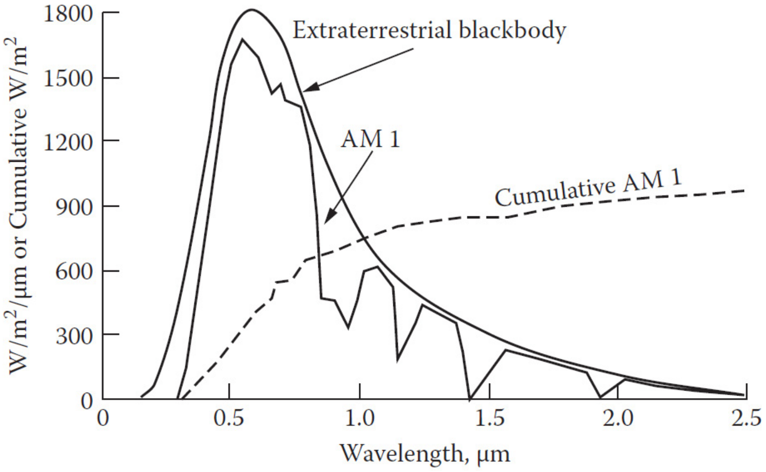

Source: (MESSENGER *et al.*, 2010).

Before reaching the Earth's atmosphere, the energy available from the sun has a power density of about 1367 W/m². This quantity is referred to as the *solar constant*. But from that boundary on, ozone, water vapor and carbon dioxide absorb energy at some wavelengths in the ultraviolet, visible and infrared regions of the spectrum. Molecules and greater particles in suspension in the atmosphere also cause scattering. Rayleigh's theory states that scattering is a function of the wavelength and inversely proportional to its fourth power. This phenomenon is responsible for the blue color of the sky during daylight. Mie's theory describes the scattering for all wavelengths by larger particles and clouds (PINHO, 2014). Scattering also allows the sun to shine in the north when it is in the south. By reaching the ground level, sunlight can be absorbed and/or reflected. Scattered sunlight is referred to as *diffuse radiation*, while *direct radiation* is the light that reaches the Earth's surface without scattering. Reflected sunlight is called *albedo*, and the sum of all these components is known as the *global radiation* (DI PIAZZA, 2013).

The *air mass* (AM) concept, mentioned in Figure 2.1, is related to the path sunlight takes before reaching ground. Conventionally, for vertical incidence, the air mass equals 1 and is referred to as AM 1. Angled incidence increases the air mass – the length of the path – and its coefficient. For AM 1, the power density from the sun is around 1000 W/m². However, the solar photovoltaic industry has adopted the standard air mass as 1.5, which is an averaged angle of 48,19° formed between the sun rays and the perpendicular line to the Earth in a particular point. This convention is based on the average latitude of the countries in the north hemisphere and does not reflect every part of the world (VILLALVA, 2010). Figure 2.2 illustrates different values of air mass.

Figure 2.2 – Different values for the AM coefficient.

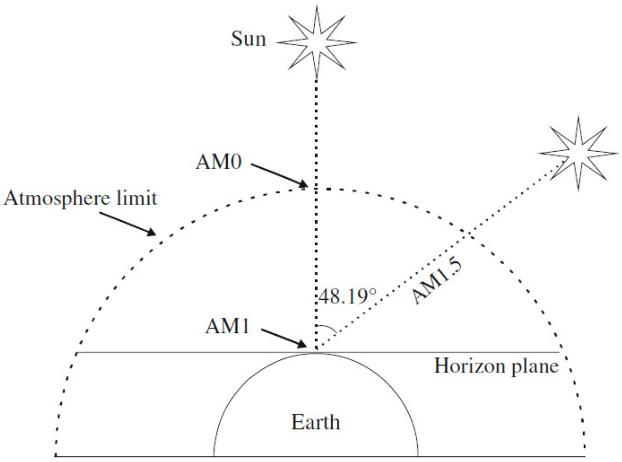

Source: (DI PIAZZA *et al.*, 2013).

At this point, the reader must be familiar with the terminology commonly used in the solar photovoltaic domain. In addition to what has been said so far, an important distinction must be made between the terms *irradiance* and *irradiation*. The former means an instantaneous measure of the power density and is expressed in W/m². The latter is the integral of the former over time, which means that *irradiation* is the energy density, expressed in kWh/m².

2.1.2 The Photoelectric Effect

The conversion of the energy radiated from the sun into its electrical form is governed by the photoelectric effect, which roughly means that when a material is exposed to light, electrons are emitted from it. This interaction of electromagnetic radiation with matter was first observed by Heinrich Hertz in 1887 who stated that the energy of the emitted electrons is directly proportional to the frequency, rather than to the intensity, of the radiated wave.

According to Einstein's quantum theory, in 1905, light is composed of small packets of energy called *quanta* – later known as *photons*. This discrete unit holds an energy that is proportional to the frequency of the electromagnetic wave, with the coefficient of proportionality being the Planck's constant, as in Eq. (2.2):

$$E = h\nu \, , \tag{2.2}$$

where E is the energy of a single *quantum*, or photon, expressed in Joules; h is the Planck's constant equal to 6.63 x 10^{-34} J.s; and ν is the frequency of the electromagnetic wave in Hertz (MESSENGER *et al.*, 2010; DI PIAZZA *et al.*, 2013). Since ν is the speed of light, in meters per second, over the wavelength, in meters, it is convenient to rewrite Eq. (2.2) to conform to the standard wavelength unit, µm, and to the atomic energy unit, electronvolt[6]. Such manipulation results in Eq. (2.3):

$$E\ [\text{eV}] = \frac{1.243}{\lambda\ [\mu\text{m}]} \, . \tag{2.3}$$

For each atom, there is a frequency threshold, f_0, below which no electrons are ejected from it. It, thus, follows that the maximum energy of the ejected electron, kinetic energy, is given by:

$$E_k = h(\nu - f_0) \ \therefore \ E_k = h\nu - hf_0 \, . \tag{2.4}$$

The quantity hf_0 is called the *work function* and is the minimum energy required to overcome the binding energy of a given metal atom/solid, i.e., the photoelectric threshold for metals equals the work function. For non-metals, the forbidden gap energy plus the electron affinity[7] define the photoelectric threshold (BARAGIOLA, 2002a; BARAGIOLA, 2002b).

Inside any atom, the energy levels are grouped in bands, where the main bands are the valence and the conduction bands, separated by a forbidden gap with different energy values

---

[6] 1 electronvolt is the elementary charge multiplied by 1 volt: 1 [eV] = 1.6 x 10^{-19} [C] x 1 [J/C] = 1.6 x 10^{-19} [J].

[7] For non-metals, *electron affinity* is the difference, in energy, between the vacuum level and the bottom of the conduction band and is typically below 1 eV. The *work function* is defined as the difference between the vacuum level and the Fermi level for metals and non-metals. The *binding energy* is the same as the *photoelectric threshold* in this context. For further information, the reader may refer to (BARAGIOLA, 2002a; BARAGIOLA, 2002b).

for distinct atoms. These different energy gaps (E_g) define the conductivity of each element. For insulators, the forbidden gap has a large energy, whereas in a semiconductor, smaller energy values exist. For conductors, the valence and conduction bands are overlapped. Figure 2.3 illustrates the structure of these gaps.

Figure 2.3 – Representation of the forbidden gaps (or bands) for (a) insulator, (b) semiconductor, and (c) conductor.

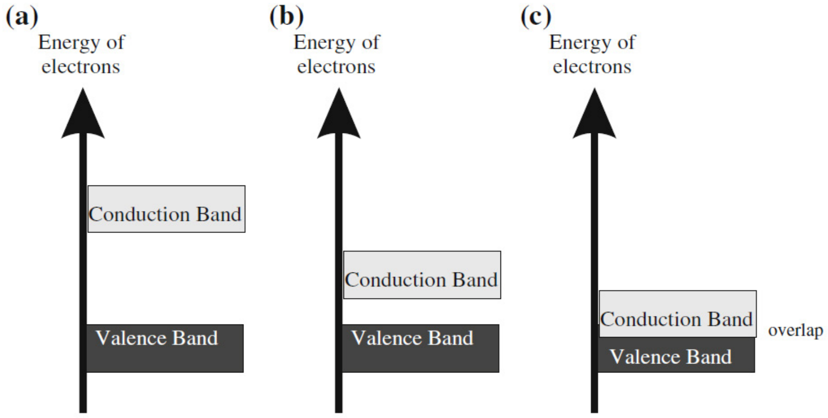

Source: (DI PIAZZA *et al.*, 2013).

The energy values of these forbidden gaps (E_g) slightly vary with temperature. For example, for a silicon atom, E_g is defined by Eq. (2.5). It is notable that as the temperature increases, the energy of the forbidden gap decreases.

$$E_g = 1.17 - \frac{(0.000473)T^2}{T + 636}. \tag{2.5}$$

If we consider the blue component of the visible sunlight, which has an approximate wavelength of 0.5µm, it is derived from Eq. (2.3) that a single photon has an energy of 2.48 eV. For a silicon atom with E_g = 1.12 eV at T = 300 K, and considering an electron affinity of 1 eV, that would result in a photoelectric threshold of about 2.12 eV. Since the photon energy for the given wavelength exceeds the binding energy, a photoelectric emission takes place and the resultant kinetic energy of this ejected electron, calculated through Eq. (2.4), is 0.36 eV. It should be noted that for a silicon dioxide (SiO_2), with a forbidden gap of 9 eV, the same photon could not detach any electron from the compound. That is clearly expected since it refers to an insulator in which neither thermal energy, electromagnetic radiation nor an electric field with reasonable magnitude can raise the energy of an electron towards the conduction band.

Once a photoelectric emission – or photon absorption – occurs, an electron in the conduction band and the corresponding hole in the valence band are created. This free electron-hole pair (EHP) is then able to participate in the conduction process in the material as charge carriers as long as any phenomenon occur to make them move. Recalling basic electronics lessons, diffusion in the *pn* junction of two semiconductor materials causes a current to flow from the *p*-side to the *n*-side when tied by a wire, and such current is proportional to the number of EHPs generated by photon absorption. A photovoltaic cell, depicted in Figure 2.4, is a specially designed *pn* junction device whose properties are discussed in the next subsection.

Figure 2.4 – A photovoltaic cell diagram.

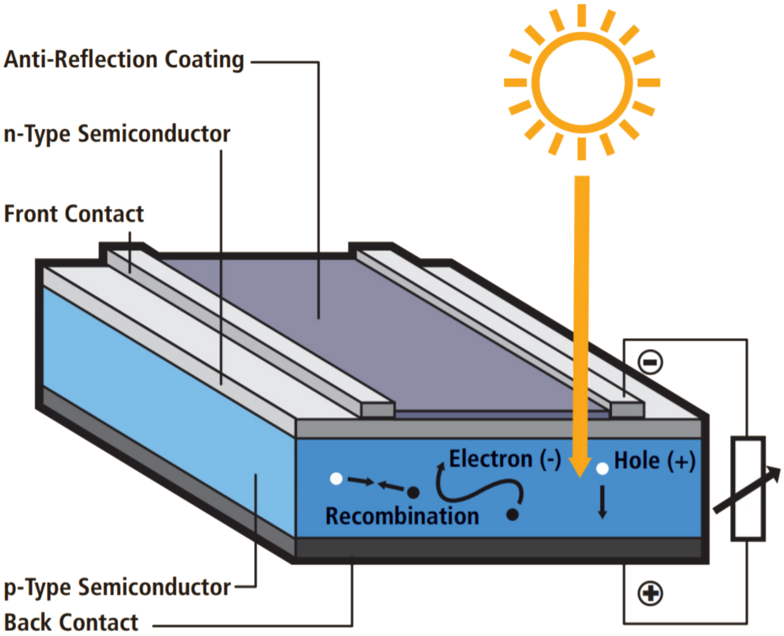

Source: Adapted from (IPCC, 2012).

2.1.3 Photovoltaic Cells

Before stepping into the subject and for the benefit of didactics, redundancy should be allowed to explain the terminology used hereinafter.

2.1.3.1 Terminology

The elementary unit that converts sunlight into electricity is the *photovoltaic cell* (PV cell). The commercially available device made up of series/parallel connection of PV cells enclosed in a housing is the *PV module*. PV modules are popularly known as solar panels, although such terminology is hardly used within this document. In a similar way to cells, PV modules can also be arranged in series/parallel circuitry to serve higher power demands. This arrangement is called *PV array*. Figure 2.5 describes these conceptual terms with images.

Figure 2.5 – Diagram of the different photovoltaic components.

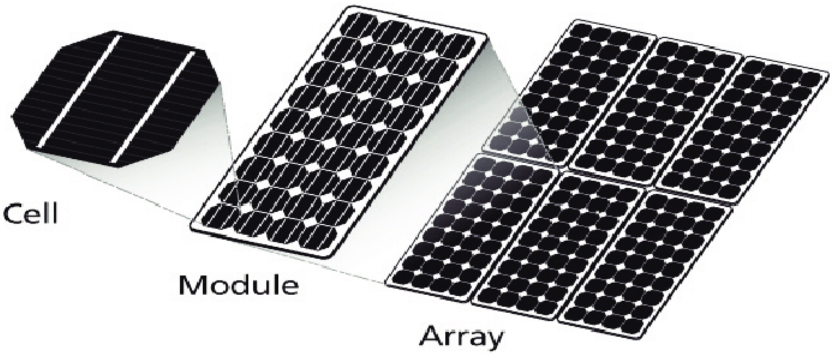

Source: (SRI VASTAV *et al.*, 2016).

2.1.3.2 Technological Development

Concerning PV cells, despite of the huge advances in cell technologies historically experienced and shown in Table 1.1, the most common type remains the silicon-based cells for a number of reasons, among which raw material abundance, high conversion efficiency and technological maturity (PINHO *et al.*, 2014).

The cell technologies can be grouped into three main generations. The first generation refers to crystalline silicon cells (c-Si), either mono- or multicrystalline ones, and they are the dominant technology in the market. The monocrystalline silicon cells are the most efficient of its class, but energy-intensive in the production. Multicrystalline/polycrystalline[8] cells emerged to overcome this disadvantage at the cost of reduced conversion efficiencies.

The second generation is the so-called thin-film technology. They are termed as so due to the smaller thickness of the substrates, 1 to 2 μm, whereas providing higher photon absorption rates compared to c-Si technologies[9]. Examples are amorphous silicon (a-Si), gallium arsenide (GaAs), indium phosphide (InP), copper indium gallium diselenide (CIGS), cadmium telluride (CdTe) and copper zinc tin sulfide (CZTS). They typically reveal lower conversion efficiencies compared to first-generation cells, but even less energy-intensive manufacturing processes. Production costs are also significantly reduced due to the minimal amount of material used.

---

[8] Microcrystalline is a structure with a grain size less than 1 μm, while polycrystalline is sized less than 1 mm and multicrystalline less than 10 cm (DI PIAZZA *et al.*, 2013).

[9] A comparison of the current density per optical path length for thin films (a-Si, CdTe, CIS) and silicon is available in (MESSENGER *et al.*, 2010). The reader is referred to Figure 11.1 on page 408 of the referenced book.

The third generation comprises Perovskite[10], die-sensitized and organic solar cells; concentrator photovoltaic cells (CPV); and multijunction cells. While die-sensitized and organic cells exhibit low efficiencies, according to (GREEN *et al.*, 2017), Perovskite cells provide similar efficiency compared to the dominant monocrystalline silicon technology, but at a reduced cost and less complex manufacturing process (WANG, 2014). Regarding CPV and multijunction alone, as well as the combination of both technologies, record efficiencies have been achieved at the solar cell and solar module levels. Other improvements to these technologies and different proposals can be investigated in specialized literature. The interested reader is encouraged to refer to section 11.6.4, on page 442 of (MESSENGER *et al.*, 2010).

One of the most recent technologies, worth mentioning in this short review, is on transparent organic photovoltaic, TOPV, cells (BULOVIC *et al.*, 2018). Although still under intense laboratory research & development, the authors claim that commercially available devices will be soon realized (GENT, 2017). Their current efficiencies range from 0.5% to 5%, achieving transparencies from 53% to over 70%. What drains attention into this technology is the possibility of inexpensive and widespread adoption in diverse applications, mainly architectural glass for building-integrated photovoltaics, BIPV (SHUKLA *et al.*, 2017).

2.1.3.3 Electrical Characteristics

Accurately modeling a PV cell behavior allows for its proper emulation under varying operating conditions, which enables, for example, advanced system analysis for power converters and MPPT algorithms without necessary access to an actual PV plant.

Starting from the analytical solution of the minority carrier diffusion equations, a mathematical expression for the current-voltage relation of an ideal PV cell is given by:

$$I = I_{ph} - I_{s1}\left(e^{\frac{qV}{kT}} - 1\right) - I_{s2}\left(e^{\frac{qV}{kT}} - 1\right), \qquad (2.6)$$

in which:

I is the PV cell output current;

I_{ph} is the photo-generated current;

I_{s1} is the dark saturation current due to recombination in the quasi-neutral region;

I_{s2} is the dark saturation current due to recombination in the space charge region;

q is the elementary charge, 1.6 x 10^{-19} C;

---

[10] A special structured compound with organic-inorganic material as the light absorption layer.

k is the Boltzmann's constant, 1.38 x 10^{-23} J/K;

V is the PV cell output voltage; and

T is the PV cell temperature.

This represents the basic double diode model to be adapted accordingly. The first adaptation refers to the ideality factor of both diodes, A_1 and A_2. The ideality factor ranges from 1 to 2, where 1 suits diodes dominated by recombination in the quasi-neutral region, and 2 for those dominated by recombination in the space charge region. Eq. (2.6) becomes:

$$I = I_{ph} - I_{s1}\left(e^{\frac{qV}{A_1 kT}} - 1\right) - I_{s2}\left(e^{\frac{qV}{A_2 kT}} - 1\right). \tag{2.7}$$

However, in a real PV cell some series/parallel parasitic resistances contribute to the reduction of the output current. Series resistances, R_s, are primarily due to inherent resistances of the *n* and *p* layers, front and back contact resistances, and the resistance of the metal grid. Leakage currents of the *pn* junction due to manufacturing defects, for instance, local short-circuits in the *n*-layer, account for the parallel resistances, R_p. Figure 2.6 presents a more approximated circuit model of a PV cell. Conforming to this analysis, Eq. (2.7) becomes:

$$I = I_{ph} - \underbrace{I_{s1}\left(e^{\frac{q(V+IR_s)}{A_1 kT}} - 1\right)}_{I_{d1}} - \underbrace{I_{s2}\left(e^{\frac{q(V+IR_s)}{A_2 kT}} - 1\right)}_{I_{d2}} - \frac{V + IR_s}{R_p}. \tag{2.8}$$

Figure 2.6 – General model of a PV cell with parasitic resistances.

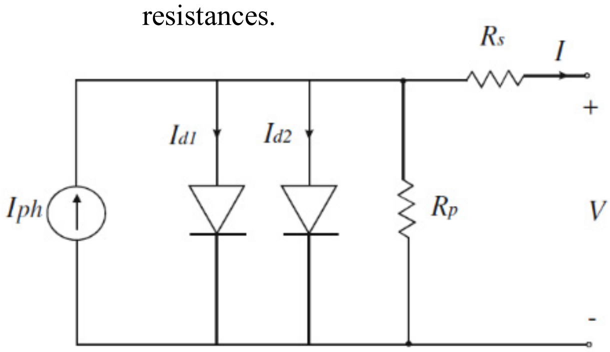

Source: (DI PIAZZA *et al.*, 2013).

Eq. (2.8) is the generalized double diode model with parasitic series and parallel resistances considered. This accurate model is very suitable for investigating cell manufacturing optimization processes. However, for PV power systems analysis, a simpler approach can be used. Conventionally, the dark saturation current due to recombination in the space charge region is neglected, thus I_{d2} can be removed from Eq. (2.8) leading to:

$$I = I_{ph} - I_{s1}\left(e^{\frac{q(V+IR_S)}{A_1kT}} - 1\right) - \frac{V + IR_s}{R_p}. \qquad (2.9)$$

This quite general model in Eq. (2.9), known as the single diode model, is still suitable for most of the cell types. Furthermore, due mainly to the predominant use of silicon, the omission of the term "-1" is a typical simplification since the dark saturation current is much smaller than the exponential component. The resultant expression is:

$$I = I_{ph} - I_{s1}\left(e^{\frac{q(V+IR_S)}{A_1kT}}\right) - \frac{V + IR_s}{R_p}. \qquad (2.10)$$

The model in Eq. (2.10) is, to some extent, accurate, especially for silicon cells. Additional simplification may still be applied by considering R_p very large once leakage currents tend – and are desirable – to be very small. This leads to the four-parameter model:

$$I = I_{ph} - I_{s1}\left(e^{\frac{q(V+IR_S)}{A_1kT}}\right), \qquad (2.11)$$

rewritten as

$$I = I_{ph} - e^{(V+IR_S)B_1+B_2} \qquad (2.12)$$

to emphasize the four parameters, where

$$\begin{gathered} {}^{q}/_{A_1kT} = B_1; \\ I_{s1} = e^{B_2}. \end{gathered} \qquad (2.13)$$

To obtain the cell output voltage on the basis of the current, Eq. (2.11) or (2.12) can be solved for V, as follows:

$$V(I) = \frac{\ln(I_{ph} - I) - B_2}{B_1} - IR_s\,. \qquad (2.14)$$

By knowing the four parameters I_{ph}, R_s, B_1 and B_2, the PV cell characteristics can be analyzed. A typical current versus voltage curve – the I-V curve – is shown in Figure 2.7. From the curve, three points are highlighted, namely, the open-circuit voltage point (V_{oc}), the short-circuit current point (I_{sc}), and the maximum power point (MPP). The last one has V_{MP} and I_{MP} as its coordinates. Another relevant parameter of a PV cell is the fill factor (FF). All these parameters are explained as follows.

The open-circuit voltage V_{oc}, as the name suggests, takes place when the PV cell is not connected to any load, or to a high impedance, which drives all the photo-generated current through the diode (or diodes), dropping the PV cell output current to zero ($I = 0$). Based on Eq. (2.14), it is seen that $V = V_{oc}$ depends logarithmically on the photo-generated current, which in turn, varies linearly with the solar irradiance. The effect is that smaller variations are experienced by V_{oc} than it is by the photo-generated current due to a change in the irradiance. The effect of the cell temperature, however, is much more significant to V_{oc} than it is to the output current of a PV cell.

Figure 2.7 – Typical I-V curve of a PV cell showing V_{oc}, I_{sc} and the MPP.

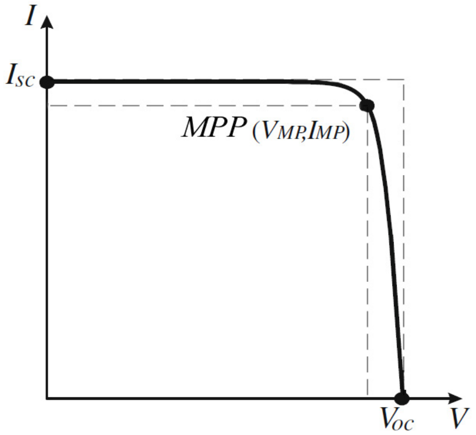

Source: Adapted from (DI PIAZZA *et al.*, 2013).

The short-circuit current I_{sc} is the maximum current available from a PV cell when it is connected to a load with very low impedance. When this happens, almost all the photo-generated current flows through the load, and the diode (or diodes) is not biased, which makes the output voltage to approach zero ($V = 0$). I_{sc} is linearly dependent on the solar irradiance and slightly increases with cell temperature. Figure 2.8 presents I-V curves for different solar irradiance and cell temperature scenarios to illustrate the behavior of V_{oc} and I_{sc}.

Figure 2.8 – I-V curves for a particular cell at (a) different cell temperatures; and (b) varying solar irradiances.

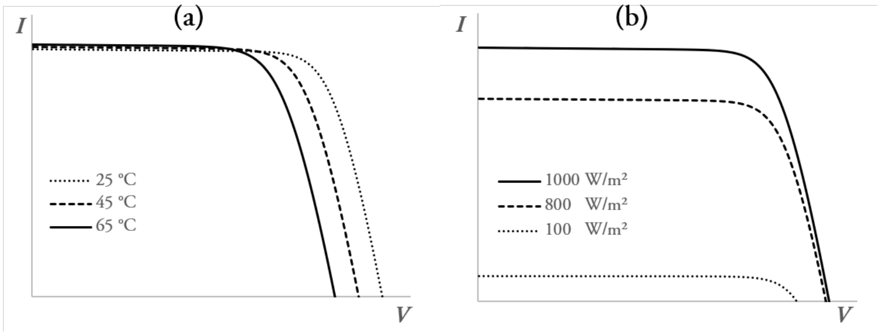

Source: The author.

As the name also suggests, the maximum power point of a PV cell is the one where the product of the cell current with the cell voltage is at a maximum. Although it is shown in

Figure 2.7, it is much clearly noticeable in a power versus voltage curve, P-V curve. The power produced by a cell is obviously null at V_{oc} and at I_{sc}, and positive for all intermediate points. Figure 2.9 plots the P-V curve over the I-V curve of Figure 2.7.

Figure 2.9 – The P-V curve of a cell.

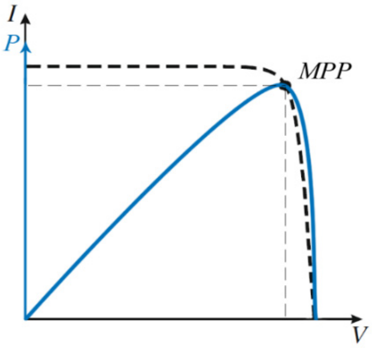

Source: The author.

The fill factor (FF) of a PV cell is related to its efficiency and is defined as the ratio between the maximum power and the product of V_{oc} and I_{sc}, in other words, the ratio between the areas of the rectangles highlighted in Figure 2.7, as in Eq. (2.15):

$$FF = \frac{P_{max}}{V_{oc}I_{sc}} = \frac{I_{MP}V_{MP}}{V_{oc}I_{sc}}. \tag{2.15}$$

FF is usually one of the parameters specified in most datasheets provided by PV cell manufacturers. It is closely related to the cell efficiency as:

$$\eta(\%) = FF\frac{V_{oc}I_{sc}}{GA} \times 100, \tag{2.16}$$

in which η is the cell efficiency, G is the solar irradiance, in W/m^2, and A is the cell area, in m^2.

The fill factor of a PV cell is affected by the parasitic resistances, R_p and R_s, and by the ideality factor of the diode, A_1. Their effects on the I-V curves are depicted in Figure 2.10.

Figure 2.10 – The maximum power point and FF changed by (a) R_p, (b) R_s and (c) A_1.

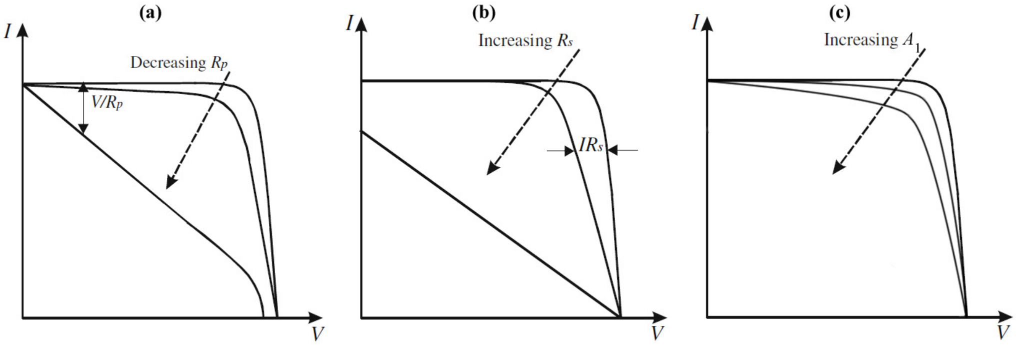

Source: Adapted from (DI PIAZZA et al., 2013).

2.1.3.4 Cell Association

Photovoltaic cells can be associated either in series, parallel, or combined series and parallel to form PV modules. Assuming identical cells and uniform irradiance and temperature conditions over all cells, the resulting circuit/association equations can be the same as those previously analyzed, but taking into account the number of series connected cells, N_s, and the number of parallel connected cells, N_p.

Considering the single diode model of Eq. (2.9), although the analysis can be extended to the full model of Eq. (2.8), the general equation for the cells association is:

$$I = N_p I_{ph} - N_p I_{s1}\left(e^{\frac{q(V+IR_sN_s/N_p)}{N_sA_1kT}} - 1\right) - \frac{V + IR_sN_s/N_p}{R_pN_s/N_p}. \tag{2.17}$$

The parallel association adds up all the N_p individual currents, either the photo-generated or the dark saturation currents, whereas the series association adds up the voltages. The equivalent resistances of the series/parallel association are also considered in this general equation. Figure 2.11 depicts the equivalent circuit models of the associations.

$$V = V_1 + V_2 + \cdots + V_{Ns}; \text{ and } I = I_1 = I_2 = \cdots = I_{Ns}; \text{ for series association.} \tag{2.18}$$

$$I = I_1 + I_2 + \cdots + I_{Np}; \text{ and } V = V_1 = V_2 = \cdots = V_{Np}; \text{ for parallel association.} \tag{2.19}$$

Figure 2.11 – Equivalent circuit models for a (a) series association, (b) parallel association, and (c) combined series-parallel association of PV cells, where Rp, Rs, Iph and Id1 are the individual parameters of a single cell.

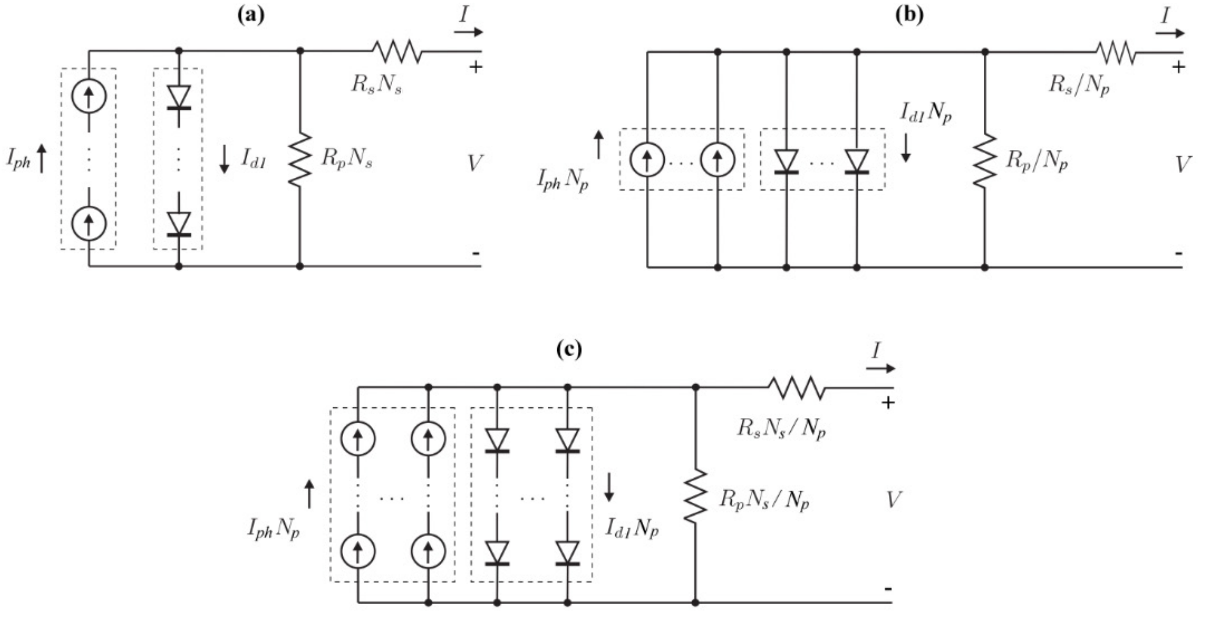

Source: Adapted from (VILLALVA, 2010).

2.2 Solar Photovoltaic Systems

2.2.1 Organization

As already stated, PV cells are associated to form PV modules, which in turn, can be further associated into PV arrays to serve whatever high power demands they are intended to. A PV system, to meet these needs, in addition to the energy conversion source, can be composed of energy storage units, charge controllers, power conditioning devices etc., depending on the specific purpose of the system.

Concerning functional, operational and interconnection requirements, PV systems are typically classified into two main categories: Grid-connected systems and stand-alone systems (VILLALVA; MESSENGER *et al.*, 2010). The former is also known as *utility-interactive systems* and are designed to operate interconnected to the electric utility grid, opposing stand-alone PV systems which are not.

With independent operation of the utility grid, stand-alone PV systems can either be direct-coupled – in which the PV array is directly connected to the load – or interfaced with energy storage units and/or other components to supply DC or AC electrical loads.

Grid-connected systems require, at least, a power conditioning unit to convert the output DC power of the photovoltaic sources into a consistent AC power with utility grid-level quality. They can operate with battery backup or be straight grid-connected, the latter being the most common utilization strategy.

Hybrid systems, either grid-connected or stand-alone ones, employ auxiliary energy sources, like wind power or fuel-based generators, in parallel with the solar PV array.

Whichever the category/type of PV system, one of the most relevant components demanding attention in this research work is the maximum power point tracker (MPPT). They can be employed in stand-alone or grid-connected systems with the purpose of constant provisioning of the maximum power available from the PV sources. They represent a crucial and mandatory aspect of the design of grid-connected systems, while being optional, although recommended, for direct-coupled stand-alone systems. Detailed analysis of the different MPPT techniques are presented in a dedicated subsection. But before moving on to it, understanding environmental conditions and how they affect a solar PV system is of primary importance.

2.2.2 Environmental Effects on PV Systems

2.2.2.1 Uniform Irradiance Conditions

Solar irradiance, i.e., the power density from sunlight, varies unpredictably during daytime as does the ambient temperature, which in turn, affects the solar cell temperature. Despite of this stochastic nature, when considering PV systems formed by multiple PV cells/modules, these quantities can either be uniformly distributed, or exhibit an uneven distribution over all PV components due to whatever source of interference/malfunction. The former event is called uniform irradiance condition (UIC) and is considered the ideal operating scenario for a PV system. Figure 2.12 presents the I-V curve of a PV array composed of 6 series-connected modules under UIC.

Figure 2.12 – I-V curve for a 6-series module array under UIC, where G = 1000 W/m² and T = 25 °C.

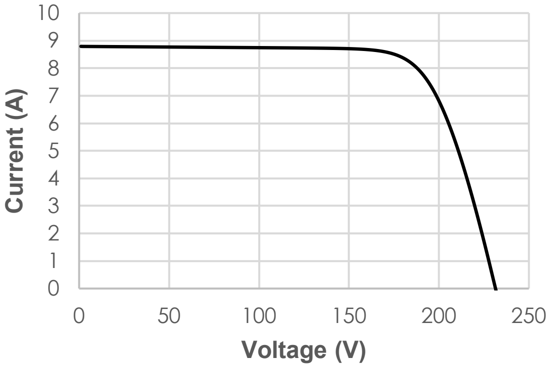

Source: The author.

In Figure 2.12, G is the solar irradiance hitting the PV array under UIC, and T is the PV cell temperature, not the ambient temperature. It is noteworthy that the cell temperature, T, relates to the ambient temperature, T_a, by:

$$T = T_a + G\left(\frac{NOCT - 20}{800}\right), \tag{2.20}$$

in which the *Nominal Operating Cell Temperature*, NOCT, is specified by the PV cell/module manufacturer and corresponds to the temperature the cells will reach when the irradiance is 800 W/m² and the ambient temperature is 20 °C with wind speeds no more than 1 m/s.

2.2.2.2 Partial Shading Conditions

A partial shading condition (PSC) occurs when an uneven distribution of solar irradiance, and thus, cell temperature, hits the PV array due to clouds, shadows from neighboring buildings and other objects, tree leaves and any other material covering a small portion of the modules etc. In this case, not all modules composing the array receive the same amount of energy from the sun. This imposes not only a loss in efficiency and output power, but can also cause irreversible damage to the PV system if not properly addressed, which is typically performed by inserting *bypass diodes* in the association.

On the occurrence of PSC in a series assembly of PV components, the cells/modules affected by the shading will limit the overall current flowing through the circuit, reducing, thereby, the output power of the system (ALONSO-GARCÍA *et al.*, 2006). Figure 2.13 illustrates this phenomenon on the I-V curve of a series-connected array.

Figure 2.13 – The effect of PSC on the I-V curve of an array with and without bypass diodes.

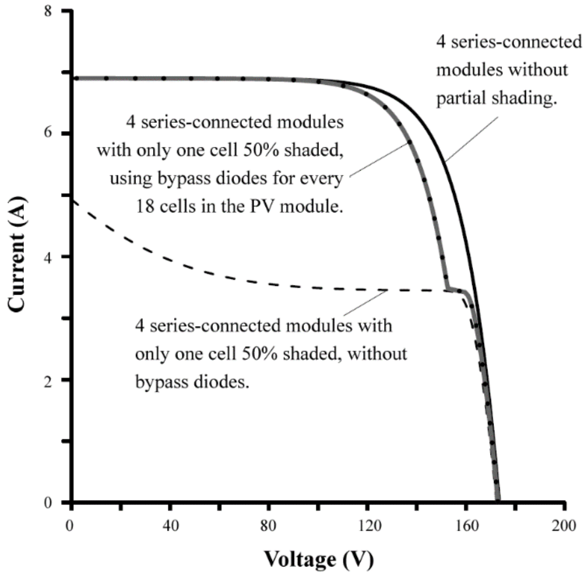

Source: Adapted from (PINHO *et al.*, 2014).

In the I-V curves of Figure 2.13 it is seen that without bypass diodes in the series association of four PV modules, the current flowing through the modules (dashed line) is significantly reduced when compared to the situation without shading. This is caused by an intentional shading of half a single cell in one of the modules.

Depending on the number of cells that compose the module – or the modules that compose the array – under PSC, the shaded cells – or modules – will be highly reverse biased, causing what are called *hot spots* and consequent damage to the module – or array. To overcome such an undesirable phenomenon, bypass diodes are inserted in the circuits, although they modify the power-voltage curve of the system by creating multiple maxima. Deep studies on the effects of bypass diodes under PSC can be appreciated in (QUASCHNING *et al.*, 1996; SILVESTRE *et al.*, 2009). The reverse biasing of the shaded cells within a module cause them to consume power instead of generating and can be understood by the diagram in Figure 2.14.

Figure 2.14 – Reverse biasing of a shaded cell in a series assembly.

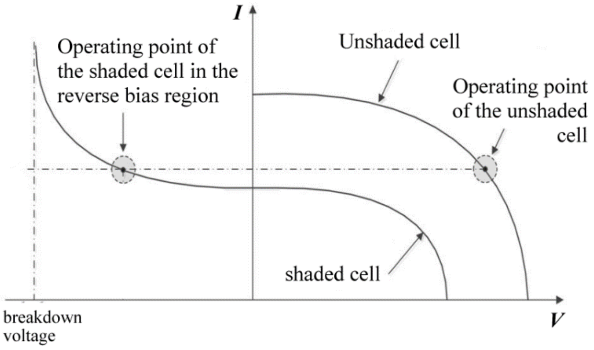

Source: Adapted from (SEYEDMAHMOUDIAN *et al.*, 2015).

Because of the series association, the current flowing through the circuit is the same for all cells. When a cell is shaded it is forced to operate in the reverse bias region in order to maintain the same current flowing, dissipating power in the form of heat. Once the breakdown voltage is reached, the PV cell is permanently damaged, and an open circuit is established. Figure 2.15 exposes a real case of PSC occurring in a module during a period of the day.

Figure 2.15 – Partial shading of cells in a PV module. Snapshots taken at (a) 12:17 p.m., (b) 12:56 p.m. and (c) 13:31 p.m.

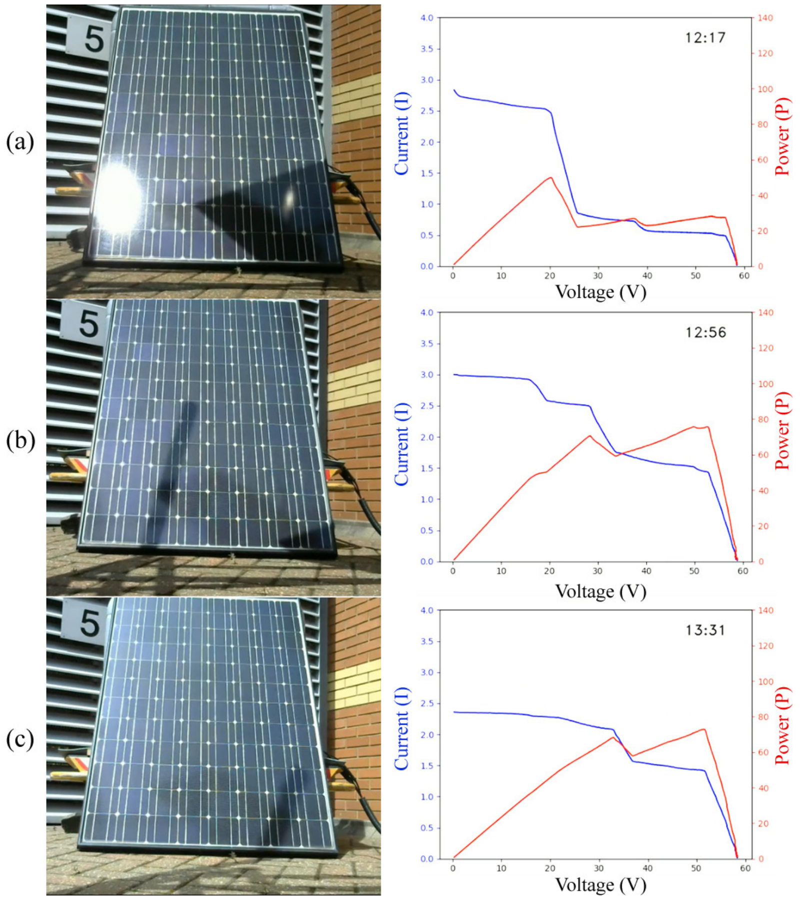

Source: Captured from (https://www.youtube.com/watch?v=t-Np7kvmj1s).

2.2.3 Solar Photovoltaic Arrays

2.2.3.1 Association

PV modules are associated to compose arrays. Following the same procedure as for cell association, they can be arranged into series, parallel or a hybrid combination. When more than one module are connected in series, they form what is called a *string*. Multiple strings may then be connected in parallel. A PV array can be either a single string or the parallel combination of strings. Recalling the association equations for cells, the same equations apply for module association, which are:

$$V = V_1 + V_2 + \cdots + V_{Ns};\ \text{and}\ I = I_1 = I_2 = \cdots = I_{Ns};\ \ \text{for series association.} \qquad (2.21)$$

$$I = I_1 + I_2 + \cdots + I_{Np};\ \text{and}\ V = V_1 = V_2 = \cdots = V_{Np};\ \ \text{for parallel association.} \qquad (2.22)$$

In Eqs. (2.21) and (2.22), N_s and N_p correspond, respectively, to the number of series-connected modules and the number of strings in parallel. The I-V curves of the associations, either under UIC or PSC, are illustrated in Figure 2.16.

In PV arrays, the use of blocking and bypass diodes is essentially recommended. The next subsections will shortly discuss the operation of these devices.

Figure 2.16 – I-V curve composition for (a) two series-connected modules under UIC; (b) two parallel-connected modules under UIC; and (c) two series-connected modules under PSC.

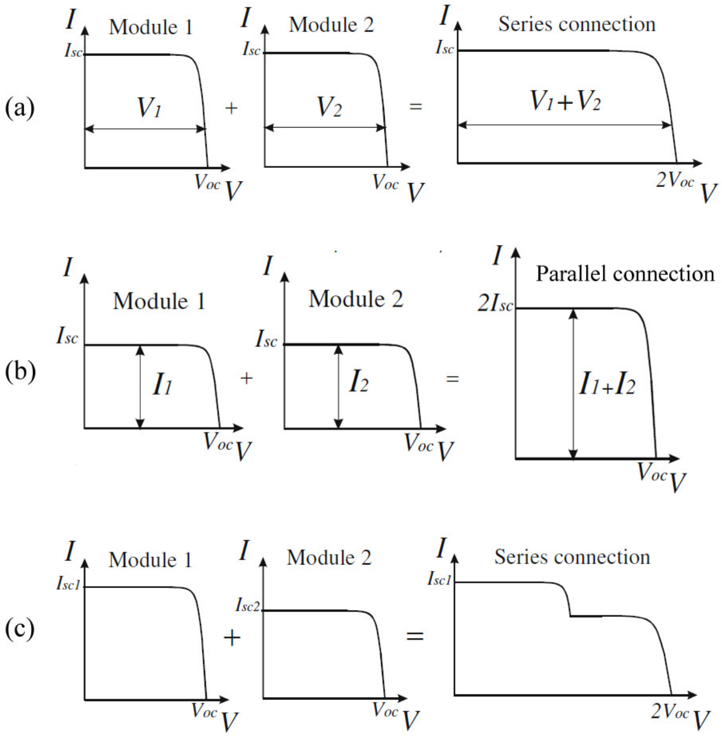

Source: Adapted from (DI PIAZZA *et al.*, 2013).

2.2.3.2 Blocking Diodes

These diodes are used to avoid undesirable current flow in parallel configurations subjected to PSC, i.e., one string feeding other strings, or reverse current flowing from the energy storage system to the PV array in battery-backup PV systems during nighttime, although this practice has been reported as deprecated by (GREACEN *et al.*, 2001). The diagram in Figure 2.17 depicts the operation of the blocking diode in a PV array.

The blocking diodes are series connected to strings and cause a power loss of $V_{th} \times I$, where V_{th} is the voltage threshold of the diode and I is the PV string current. They must be capable of undertaking reverse voltages equal to the open circuit voltage of the string and forward currents equal to the maximum current available from the string.

2.2.3.3 Bypass Diodes

These diodes are used to protect PV strings from any current mismatch, such as is the case in PSC. They are, in the ideal case, parallel connected to each module in the string to provide an alternative path to the current that cannot flow through the shaded PV module. In actual PV systems, however, due to the increased cost of inserting a bypass diode for each module in the array, it is a common practice to adopt a group of modules to be under the protection of one bypass diode. There is a tradeoff between cost and performance under mismatching conditions for determining the number of bypass diodes in a module or array. For a deep understand of the subject, see (QUASCHNING *et al.*, 1996; SILVESTRE *et al.*, 2009). The diagram in Figure 2.17 depicts the operation of the bypass diode in an ideal PV array subject to PSC.

Figure 2.17 – Operation of (a) bypass diodes and (b) blocking diodes under PSC.

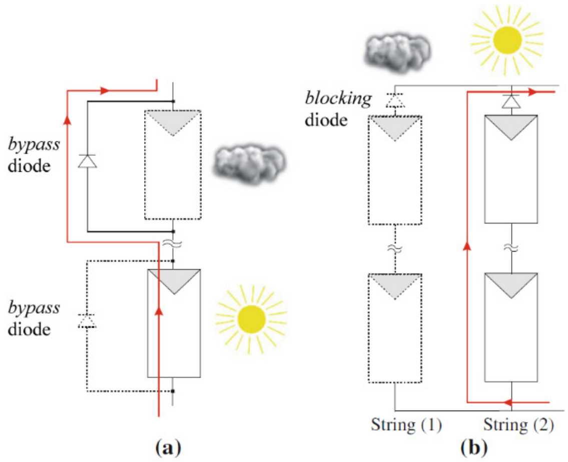

Source: Adapted from (DI PIAZZA *et al.*, 2013).

2.3 Maximum Power Point Tracking

2.3.1 Introduction

No matter the amount of financial investment applied into a solar photovoltaic energy system, it is expected that such system can efficiently operate under uniform and varying whether conditions, which means that the system must be able to deliver the maximum energy as possible during its operation. This circumstance allowed the development of maximum power point trackers (MPPT) or maximum power point (MPP) tracking techniques that, as the name generously suggests, have the purpose of constantly search for the MPP so to set it as the operating point of the PV system during its operation.

The maximum power point depends on the available irradiance, temperature and mismatching condition that a PV system undergoes. It is clearly observable in the power-voltage curve, P-V curve, of the photovoltaic source. This curve exhibits a single maximum under uniform irradiance conditions and multiple local maximum points when partial shading affects the PV components, either at the cell level or at the module level, under bypass diode protection. Figure 2.18 exhibits two P-V curves for a typical PV system at UIC and PSC.

Figure 2.18 – Power-voltage curves for a typical PV array subjected to (a) uniform irradiance conditions and (b) partial shading conditions.

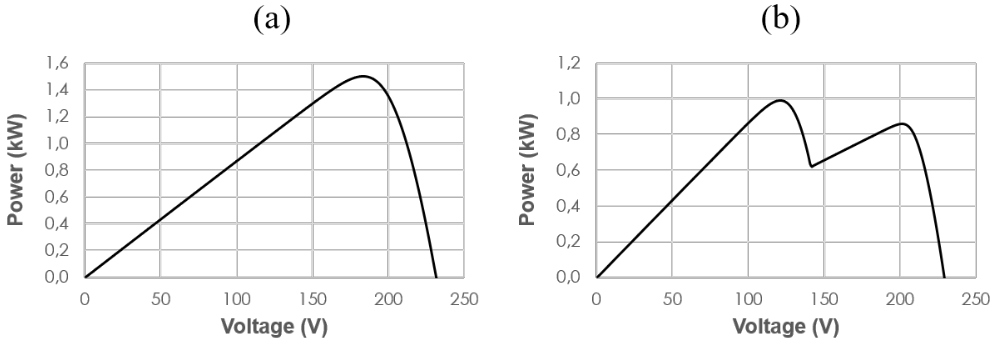

Source: The author.

The MPP in Figure 2.18(a) is unique, but multiple local maxima appear in Figure 2.18(b), where the global MPP (GMPP) occurs at about 120 V, and one local MPP (LMPP) at about 200 V. The MPPT must, therefore, be able to track the unique MPP when operating under UIC, or the GMPP under PSC, distinguishing it from the local MPPs that might exist.

2.3.2 Assessing MPPT techniques

On the basis of the aforementioned circumstances, some criteria for assessing MPPT techniques would include (LYDEN *et al.*, 2016):

i. Ability in differentiating local and global maximum points;
ii. Ability to locate the global maximum point;
iii. Celerity in tracking the MPP under varying environmental conditions;
iv. Stability or minimal oscillation in the steady-state;
v. Dependability on system-specific parameters; and
vi. Complexity or cost of the solution.

These criteria will eventually be used to assess the MPPT techniques discussed in this research work.

2.3.3 Classical Techniques

In this work, classical MPPTs refer to those techniques conventionally employed in most commercially available devices. They often include MPP estimation and hill climbing methods which are briefly explained as follows.

2.3.3.1 Maximum Power Point Estimation

These algorithms are mainly based on empirical or analytical estimation of the MPP in relation to collected samples of the voltage and current in a PV system. The most simple forms are called *fractional open-circuit* voltage and *fractional short-circuit current* in which the MPP is supposed to lie in a fraction of the V_{oc} or the I_{sc} as in:

$$V_{MP} = k_1 V_{oc}\,, \tag{2.23}$$

$$I_{MP} = k_2 I_{sc}\,. \tag{2.24}$$

In Eqs. (2.23) and (2.24), the constants of proportionality are typically set within 0.71-0.78 for k_1, and 0.78-0.92 for k_2 (LYDEN *et al.*, 2016). These techniques are dependent on the measured values of V_{oc} and I_{sc} which leads the PV system into zero-power states during operation.

Improvements to such techniques often increase the number of samples used to provide better estimations of the MPP location. Other methods use a model-based approach with a number of samples, including V_{oc} and I_{sc}, to approximate the electrical model of the PV system and then estimate the MPP accordingly.

These techniques are not designed to operate under non-uniform irradiance conditions or any other mismatching condition. Another disadvantage is the fact that they can force the PV system to provide no power during short periods of operation.

2.3.3.2 Hill Climbing Methods

Hill climbing techniques lie on the characteristic nature of the power-voltage curve that exhibits a maximum point around which the power decreases in either direction. These algorithms essentially measure the change in power due to a perturbation in a control variable, typically the voltage or the duty cycle of the power converter that interfaces the PV system. That change in power defines the direction of the next perturbation until the MPP is found. The most notable examples of the hill climbing technique are the Perturb & Observe (P&O) and the Incremental Conductance (IncCond) algorithms.

Perturb & Observe is based on the following approach:

Table 2.1 – Operation principle of the P&O method.

Perturbation	Effect on PV Power	Direction of Perturbation
positive	positive	must be maintained
positive	negative	must be reversed
negative	positive	must be maintained
negative	negative	must be reversed

Source: The author.

Considering the voltage as the control variable, Table 2.1 is mathematically described as:

$$\frac{dP}{dV} > 0 \text{ (this occurs on the left of the MPP),} \tag{2.25}$$

$$\frac{dP}{dV} < 0 \text{ (this occurs on the right of the MPP).} \tag{2.26}$$

The point where the derivative of the power with respect to the voltage is zero is the maximum power point. P&O essentially exhibits a hovering nature on the MPP, which means it oscillates around this point, repeatedly and unceasingly. Figure 2.19 presents the flowchart of the P&O algorithm.

The incremental conductance algorithm is based on the same principle of the P&O method, i.e., they depend on the derivative of the power with respect to the voltage, but IncCond operates on the concepts of instantaneous conductance and incremental conductance (the reciprocal of resistance), and continuously measures the current and voltage of the PV source to determine the direction of the next perturbation on the control variable. Mathematically:

Figure 2.19 – Flowchart of the Perturb & Observe (P&O) algorithm.

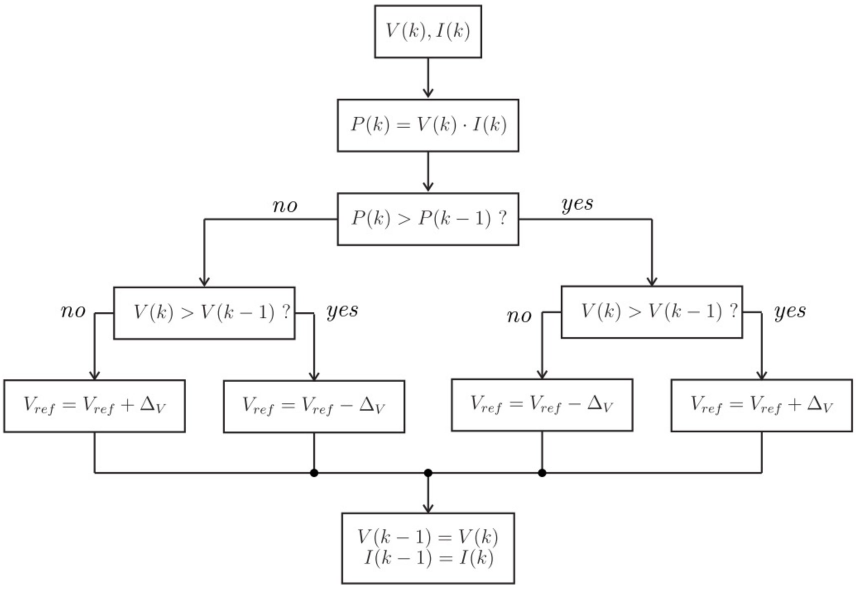

Source: Adapted from (VILLALVA, 2010).

$$\frac{dP}{dV} = \frac{d[IV]}{dV} = I + V\frac{dI}{dV} \approx I + V\frac{\Delta I}{\Delta V}, \tag{2.27}$$

which means

$$\frac{\Delta I}{\Delta V} > -\frac{I}{V} \text{ (this occurs on the left of the MPP),} \tag{2.28}$$

$$\frac{\Delta I}{\Delta V} = -\frac{I}{V} \text{ (this occurs at the MPP),} \tag{2.29}$$

$$\frac{\Delta I}{\Delta V} < -\frac{I}{V} \text{ (this occurs on the right of the MPP).} \tag{2.30}$$

With the information from Eqs. (2.28) to (2.30), in other words, by comparing the instantaneous conductance (I/V) with the incremental conductance ($\Delta I/\Delta V$), the algorithm determines the direction of the next perturbation. A flowchart of the operation of IncCond is depicted in Figure 2.20.

IncCond algorithm, as opposed to P&O, has one stopping criterion which avoids oscillations around the MPP, depending on the perturbation size. Both P&O and IncCond present a tradeoff between step size and speed of convergence towards the MPP. Improvements to such algorithms are mainly based on making the step size variable. Similarly to MPP estimation techniques, hill climbing methods render inefficient under PSC.

Figure 2.20 – Flowchart of the Incremental Conductance (IncCond) algorithm.

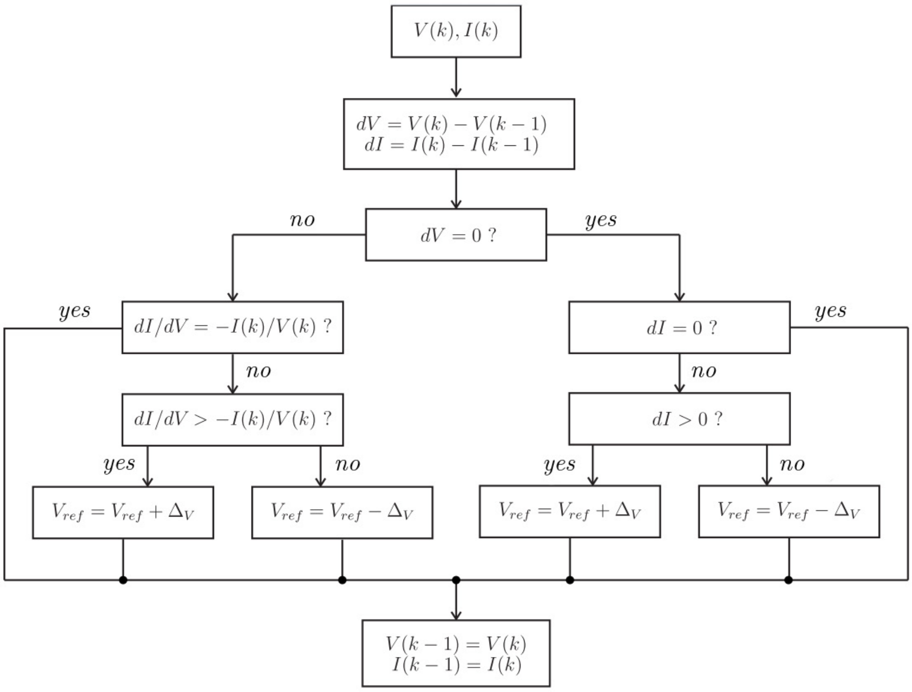

Source: Adapted from (VILLALVA, 2010).

2.3.4 Intelligent Techniques

There are many ways, widely explored in the literature, in which intelligent techniques can be used in the MPPT problem. Some of these are briefly presented as follows.

2.3.4.1 Adaptation of the Classical Techniques

This category comprises all artificial intelligence algorithms working as an adaptation tool for the classical hill climbing methods. They are mainly used to define a variable perturbation size with the purpose of improving accuracy and reducing steady-state oscillations.

Fuzzy logic techniques are employed as an inference engine to derive a proper perturbation size, either by Mamdani or Takagi-Sugeno approaches. These inference systems, although very efficient in defining the step sizes, are generally system-specific and may require high computational power. Artificial Neural Networks (ANNs) do not require previous knowledge of the system since they have the ability to learn, but the computational cost they add is the price to pay for the gain in efficiency.

These techniques still lack the ability to locate the global MPP when operating under non-uniform irradiance conditions, once they are just an adaptation of the classical methods.

2.3.4.2 Methods Based Purely on Artificial Intelligence

These methods include the use of ANNs and optimization algorithms. ANNs can be employed to model the PV system and properly define the MPP based on the input information of the irradiance and temperature levels. This can be quite efficient, but as the cells and other components of the system degrade by any possible means, the mapping loses its representation and the MPPT may no longer locate the maximum power point. In addition, this technique turns out to be inefficient under partial shading conditions, where the mapping previously learnt may not represent this environmental phenomenon.

Optimization algorithms, instead, provide high efficiencies under all environmental conditions by locating the global MPP with significant probability. One of the algorithms heavily explored in the literature for such purpose is the Particle Swarm Optimization (PSO). PSO and other similar optimization techniques are dependent on some internal parameters that must be previously defined, and their efficiency rely on the setting of the initial population. They offer a somewhat fast convergence to the GMPP and present low probability of reaching a local maximum instead of the global one. These reasons make them the choice of most intelligent techniques dedicated to overcoming the MPP tracking under PSC. Chapter 3 provides a detailed background of the most usual optimization algorithms.

2.3.4.3 Hybrid Methods

These are mainly based on a multiple step approach, in which an optimization algorithm performs the GMPP tracking, with reduced accuracy but faster execution, in a first step and then a classical hill climbing method is invoked to pursue the exact GMPP location.

The addition in complexity may be balanced with the increase in efficiency, in either uniform or non-uniform irradiance conditions, but the execution time is penalized.

2.4 Current Scope of the Research on MPPT

Concerning maximum power point tracking for solar photovoltaic systems over the last decade, countless works have been published and, as this writing is on course, many more still arise. In attempt to summarize these various proposals, a brief description of what has been done since 2005 will be presented in the next paragraphs.

In (KIMBALL & KREIN, 2008), an optimization technique based on the ripple of power switching devices was applied to seek the MPP. The proposed Ripple Correlation Control (DRCC) is the digital version of its analog counterpart, previously proposed for tracking the

MPP in solar PV plants. This technique exploits the inherent characteristic of switching devices in power electronic converters to obtain the gradient of a cost function. Diverging from any other method, it has a fast execution because it does not need to wait for the voltage and current to stabilize before the next sampling can be done. Excellent results could be achieved with this technique, but it still depends on the derivative of a unimodal cost function, which means that for partial shading conditions, it would fail in tracking the GMPP.

Different approach was adopted in (GOKSENLI *et al.*, 2016) to find the maximum power point in uniform irradiance conditions. They modeled a PV system with the so-called Akbaba modeling technique that uses the incoming irradiance and open-circuit voltage as the inputs, delivering the corresponding maximum power current and voltage of the system, from which the maximum power is calculated. From a practical perspective, the need for continuous measurements of the open-circuit voltage represents a significant hindrance. Besides, when considering partial shading conditions, multiple irradiance sensors should be used which invalidates the proposal due to the high cost of accurate pyranometers.

In the field of intelligent techniques, (OCRAN *et al.*, 2005) proposed an artificial neural network (ANN) for mapping the inputs to the voltage that leads to maximum power. They continuously measured the open-circuit voltage of the PV system and used this information with the current time of the day as inputs to the multi-layered ANN. Although presenting relevant capability for predicting the corresponding MPP voltage, it is quite uncertain that it will render efficient at real operating conditions. Moreover, constant measure of the open-circuit voltage implies constant disconnection of the PV system with the load or battery system it is attached to.

Following the neural network approach, (ÇELIK & TEKE, 2017) proposed a hybrid system with an artificial neural network and the classical P&O algorithm in a two-stage method. The first one tries to estimate the location of the MPP through the ANN and then narrow down the search space for the next stage, performed by P&O. The authors ran simulations for uniform irradiance conditions with rapid variations, but failed in providing a true experiment under a partial shading condition. Judging by the strategy used, it is quite certain that this approach is not able to properly track the GMPP in such non-uniformity.

With respect to partial shading, a hybrid approach was proposed in (PATEL & AGARWAL, 2008), in which the classical perturb & observe (P&O) technique was extended to cope with multimodal power-voltage curves. A complex algorithm with many branches is supposed to detect the global MPP with the help of P&O. The authors claim that a trend exist in the power-voltage curve under partial shading conditions and use this information to locate the GMPP amongst local MPPs. Despite of being inexpensive in terms of processing power, which allows easy implementation in low-cost microprocessors, the algorithm lies on constant measurements of the open-circuit voltage of the PV system, the same drawback as in (OCRAN *et al.*, 2005).

Similar approach was adopted by (BRADAI *et al.*, 2017), where a first identifying loop is executed to estimate the location of the GMPP and then a P&O-like algorithm is ran to fine-tune the estimated GMPP. The authors claim that the approach offers high probability in detecting the GMPP under several shading profiles experimented. Although speed is alleged to be one of the highlights of the algorithm, the numerous steps within both loops are time-consuming and may explain the benefit in accuracy to the detriment of speed.

A hybrid system of fuzzy logic with a three-layered artificial neural network is developed in (SYAFARUDDIN *et al.*, 2009) to detect the global MPP under PSC. The neural network is trained with a number of partial shading profiles and is able to estimate the global maximum power point accordingly. The fuzzy controller determines the proper control signal for the power converter so that the voltage reference, provided by the ANN, is reached. In addition to the high computational power demanded for ANN plus a fuzzy logic controller, estimating the GMPP under partial shading conditions does not seem to be a good practice since these circumstances are stochastic in nature and, thus, hard to predict. This means that the MPPT has a considerable chance to underestimate the power of the PV array.

The Fuzzy technique is also employed in (AL NABULSI *et al.*, 2012) for the MPPT problem, but with a different purpose from that of the previously mentioned work. In this one, the classical P&O algorithm is adapted by the fuzzy logic to provide a variable perturbation step size, so the oscillations around the MPP are minimized. The maximum power from the PV system is also increased by the use of a two-axis solar track. The system, however, does not deal with partial shading conditions.

Yet in the domain of Fuzzy logic, (SOLTANI & KOUHANJANI, 2017) proposed a type-2 fuzzy inference system to control a PV plant and, thus, determine the MPP under uniform conditions. The Type-2 Fuzzy controller provides quick and smooth responses to the DC-DC boost converter when compared to its Type-1 counterpart. Better accuracy in detecting the appropriate MPP is also achieved with the proposed controller. The high complexity of type-2 fuzzy logic discourages its implementation in a practical sense.

In (CHEKIRED *et al.*, 2014), four different intelligent techniques for MPPT are assessed and implemented in a physical device, namely Artificial Neural Networks (ANN), pure Fuzzy Logic (FL), Adaptive Neuro-Fuzzy (ANFIS) and Fuzzy optimized by Genetic Algorithm (FL-GA). All of them exhibit similar performances, although FL-GA tend to be faster and the most accurate of them. They are used to model the PV system in order to estimate the MPP and do not cope with partial shading conditions, which means that they seem to perform well under controlled and known conditions only.

Adaptive Neuro-Fuzzy inference system had also its application into the GMPP search problem. (BELHACHAT & LARBES, 2017) proposed an ANFIS combined with a switching array topology mechanism to both mitigate partial shading effects and locate the GMPP. The ANFIS is trained offline with a large set of PV array configurations and shading patterns and once trained, it works as an estimator of the exact GMPP location. It is, thereby, a system-dependent MPPT requiring complete configuration of the array it is installed in.

Another hybrid intelligent technique, employing Differential Evolution (DE) and Particle Swarm Optimization (PSO), called DEPSO, is proposed in (SEYEDMAHMOUDIAN *et al.*, 2015) to search for the GMPP under uniform and partial shading conditions. Although a somewhat complex algorithm, the proposal achieves very good results under some uniform and non-uniform scenarios. This represents one of many applications of PSO into the MPPT problem. Other works, such as (CHOWDHURY *et al.*, 2010), (ISHAQUE *et al.*, 2012), (ISHAQUE *et al.*, 2013) and (LIAN *et al.*, 2014) also propose adaptations to the original PSO algorithm and offer remarkable results in locating the GMPP under most shading profiles. With the potential benefit in accuracy, implementation complexity in these PSO and hybrid PSO-P&O methods becomes an important issue.

In (CHAIEB & SAKLY, 2018), a hybrid proposal comprised of a modified PSO and a classical hill climbing (HC) method is designed. As a first step, the HC is executed and once a condition is reached, the so-called hybrid simplified accelerated PSO is invoked to better track the GMPP. Both the perturbation step size in the HC algorithm and the condition to switch to PSO are system-dependent and obtained with exhaustive simulations. It is clear that depending on the starting point of the HC, it will hardly find the GMPP, so it is not a good practice to use an HC method to narrow down the search space before an optimization algorithm can be executed.

In (SEYEDMAHMOUDIAN *et al.*, 2016) a new optimization-based algorithm is used to track the GMPP under uniform and partial shading conditions. The proposed algorithm, called RMO (Radial Movement Optimization), a straight application of the original proposal in (RAHMANI & YUSOF, 2014), supposedly outperforms the traditional PSO in detection speed of the GMPP. Furthermore, it reveals to be less memory-intensive than other optimization techniques. Although not many shading profiles were provided to validate its advantages against traditional swarm-based techniques, the results seem to endorse the proponent's claims.

Another swarm-based optimization, called Frog Leaping Optimization, is adapted to the MPPT problem in (SRIDHAR *et al.*, 2017). In their proposal, the global MPP is located by a population of "frogs", similar to what happens in PSO or other algorithms. Comparisons of the proposed algorithm with PSO, DE and the classical P&O are presented highlighting a good accuracy and convergence speed to the GMPP under a couple of partial shading scenarios. The implementation, however, is highly system-dependent and requires irradiance sensors for every PV module in the system, which contribute to the practical infeasibility of the technique.

In (MAO *et al.*, 2018), an adapted PSO is combined with a Frog Leaping Optimization (FLO) algorithm to properly detect the GMPP under PSC. The hybrid intelligent algorithm is applied to a PV plant where every module has its own DC-DC power converter. The MPPT is then distributed for every single module in the array and works in a module-by-module fashion. Aside from being highly system-dependent, the proposed modifications to the PSO and FLO are memory-consuming and slightly complex. Therefore, the balance between system-dependency, algorithm complexity and performance reveals not much attractive.

In the proposal of (ZAKI DIAB & REZK, 2017), a bio-inspired optimization algorithm based on the flower pollination process is applied into the MPP search in a PV system subjected to partial shading phenomena. The Flower Pollination Algorithm (FPA) resembles the operation of the Differential Evolution (DE) technique and also achieves great performance in numerous shading scenarios. With a few more steps than DE, this algorithm can be considered, to some extent, memory-consuming and complex, demanding slightly higher computational power than those the authors used for comparison purposes.

To summarize all these research efforts, it has been a trend in the recent literature, with the noteworthy exception of (BRADAI *et al.*, 2017), the use of any form of swarm-based optimization algorithm, either hybridized or isolated, in the quest for an accurate, robust, fast and feasible MPPT to address the current PV industry demands, especially for the ever-growing application of BIPVs (Building-integrated Photovoltaics) which is tremendously affected by shading phenomena.

In view of these demands, the work herein presented focuses on the application of an intelligent MPP tracker based on the Radial Movement Optimization technique, originally proposed by (RAHMANI & YUSOF, 2014) and studied in (SEYEDMAHMOUDIAN *et al.*, 2016). A modification of the original proposal, suitable for MPPT in PV systems, is suggested and assessed under uniform and non-uniform environmental conditions. The proposed MPPT intends to be accurate, less memory-intensive, system-independent, relatively fast and able to distinguish and locate the global maximum power point amongst the local ones, complying to most of the criteria mentioned in section 2.3.2.

The next chapter provides the fundamentals on population-based optimization algorithms and introduces, in detail, the Radial Movement Optimization in its original proposal.

3 EVOLUTIONARY AND SWARM-BASED OPTIMIZATION

Evolution is an optimization process through which any organism is able to adapt in constantly changing environments. In turn, swarm intelligence is a property in which a global functional pattern emerges from the interaction of social organisms with the environment surrounding them (ENGELBRECHT, 2007).

In the domain of computer sciences, Evolutionary Computing and Computational Swarm Intelligence are, thereby, algorithmic representations of these natural processes aimed at modeling the interactions among agents, and between agents and the environment in order to solve complex problems. They differ, in the theoretical viewpoint, by the means through which individuals evolve, but in a practical sense, they hold some similarities, especially in what concerns information recombination/exchange to achieve solutions. Substantiated by the characteristics in which they bear resemblance, they fall into the major category of problem-solving strategies called *metaheuristics*, a higher-level form of heuristic in which information is incorporated (BIANCHI *et al.*, 2009).

Commonly inspired in nature, a plentiful quantity of algorithms has emerged from these concepts. Two of them are selected for discussion in the following subsections based on their popularities within the scientific community, namely Differential Evolution (DE) and Particle Swarm Optimization (PSO). Representing the object of research in the present work, a relatively novel technique, another swarm-based intelligent tool called Radial Movement Optimization (RMO), is also discussed in its original formulation.

3.1 Differential Evolution (DE)

3.1.1 Introduction

Developed by Storn and Price, in 1995, Differential Evolution is a stochastic evolutionary search algorithm in which evolution is based on the differences between the individuals of a population. It diverges from other evolutionary algorithms in the sense that mutation is applied prior to crossover operations and uses a differential approach instead of a random one.

For mutation, DE employs what are called *target* and *donor* vectors and designates the offspring, after crossover, as *trial* vector. These individuals are evaluated according to a fitness function and are selected to compose the next generation based on their fitness.

3.1.2 Mathematical Description

Mutation in DE can be calculated by more than one method. Considering a population of N individuals (vectors), for each donor vector d_i, at each generation g, the mutation operator is applied by the following rule as the basic method:

$$d_i(g) = t_{r1}(g) + F[x_{r2}(g) - x_{r3}(g)]\,, \tag{3.1}$$

where $i = 1, \dots, N$; $r1 \neq r2 \neq r3$ are indices in the same interval as i; and $F \in (0, \infty)$ is the scale factor that weights the differential. The target vector, t_{r1}, is randomly chosen among the N individuals as do the other vectors, x_{r2} and x_{r3}. This method is, by convention, named *DE/rand/1*, which means it utilizes a random target vector and only one differential term.

Another method to compute the mutation is given in Eq. (3.2):

$$d_i(g) = t_i(g) + F[x_{best}(g) - t_i(g)] + F[x_{r1}(g) - x_{r2}(g)]\,. \tag{3.2}$$

This is referred to as *DE/target-to-best/2*, where 2 differentials are used and *target-to-best* means that the first differential involves one target vector, sequentially chosen, along with the fittest individual of the current population. The second difference vector is obtained as in Eq. (3.1), that is, two distinct randomly selected vectors.

After calculating the donor vector, the crossover operator is then applied. Being $CR \in [0,1]$ the so-called *Crossover Rate*, and D the dimension of the vectors, the trial vector $u_{i,j}$ is obtained as:

$$u_{i,j}(g) = \begin{cases} d_{i,j}(g), & \text{if } r \leq CR \text{ and } j = s \\ t_{r1,j}(g), & \text{if } r > CR \text{ and } j \neq s \end{cases}, \tag{3.3}$$

in which r is a random number within $[0, 1]$, s a random index within $[1, D]$ and $j = 1, \dots, D$ indicates each element of the referred vectors. In this operation, at least one element of the trial vector originates from the donor vector, whereas the remaining ones come from the target.

The evaluation of the offspring will take place after all trial vectors have been generated, i.e., $i = N + 1$. The fitness function, which is a problem-dependent feature, will associate a fitness value for every individual of the offspring. The next step is then the selection of the fittest individuals to compose the next generation population.

3.1.3 Flowchart

Figure 3.1 explains the operation of the Differential Evolution algorithm.

Figure 3.1 – Flowchart of the DE algorithm.

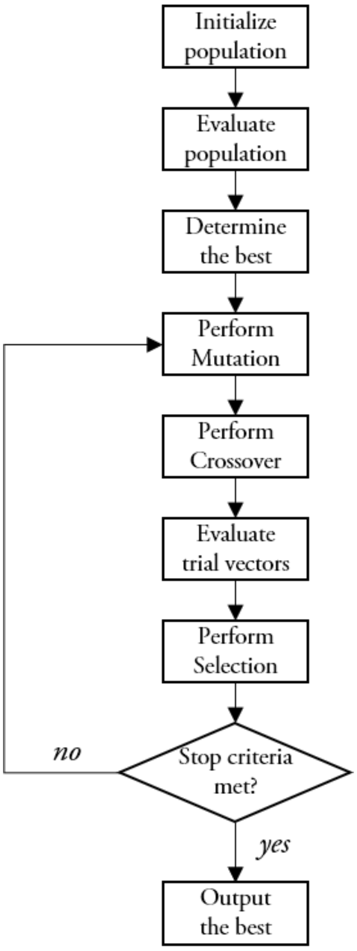

Source: The author.

3.2 Particle Swarm Optimization (PSO)

3.2.1 Introduction

Particle Swarm Optimization was introduced by Kennedy and Eberhart, in 1995, on the idea of emulating the social behavior of birds within a flock. In this stochastic optimization algorithm, particles – corresponding to individuals in evolutionary algorithms – fly through the search space, and their movements are influenced by the experience of the neighbors. A consequence of this behavior is that optimal regions can be discovered and that is how PSO converges to an optimal solution.

The movements of the particles are driven by a velocity vector generated from the information of an individual best and a global best positions. That means the velocity vector and, thus, the positions of the particles are updated based on a cognitive and a social component representing individuality and collectivity, respectively. A fitness function is also used to determine the best positions ever experienced by each particle and by the whole swarm. The mathematical approach to PSO is presented as follows.

3.2.2 Mathematical Description

The implementation of PSO can be realized in two forms that differ in the size of the neighborhood. The so-called *gbest PSO* defines the whole swarm as the neighborhood of every particle, whereas in *lbest PSO*, each particle has a limited number of neighbors.

For the *gbest PSO* implementation, the velocity vector for each dimension $j = 1, \dots, D$, of each particle $i = 1, \dots, N$, is calculated as:

$$v_{i,j}(g+1) = wv_{i,j}(g) + c_1 r1_{i,j}(g)[pbest_i(g) - p_i(g)] + c_2 r2_{i,j}(g)[gbest_i(g) - p_i(g)]. \quad (3.4)$$

In Eq. (3.4), g indicates the current iteration of the algorithm; w is the inertia weight and defines the amount of influence on the current velocity by the past velocity; c_1, c_2 are the cognitive and social learning rates, respectively; $r1$, $r2$ are random numbers in $[0,1]$; $pbest$ and $gbest$ are the personal and global best positions of each particle, respectively; and p is the current position of the referred particle.

The term $wv_{i,j}$ is the weighed inertia component of the velocity. If w is set to zero, subtle change in the directions of the particles can be experienced. On the other hand, if $w > 1$, particles will hardly change their directions. It is then reasonable to set w within [0,1].

The cognitive component, $[pbest_i - p_i]$, weighed by $c_1 r1$, is related to the particle's individual memory of the best position it ever visited and influences the velocity in the sense that particles should be attracted by their own experiences, with c_1 determining how much but stochastically weighed by $r1$.

The social component, $[gbest_i - p_i]$, weighed by $c_2 r2$, is related to the tendency of the particles to move by the influence of their neighbors' experiences, with c_2 determining how much but stochastically weighed by $r2$. Therefore, the values assigned to c_1 and c_2 will give a balance between collectivity and individuality to the general behavior of the particle's movements, while the stochastic weights would guarantee diversity.

Finally, the positions of the particles can be updated using the new velocity, as in:

$$p_i(g+1) = p_i(g) + v_{i,j}(g+1). \quad (3.5)$$

The *lbest PSO* will not be covered in this work since it is not implemented to serve as reference in the next chapters. Should the reader be interested, see (ENGELBRECHT, 2007).

3.2.3 Flowchart

A basic flowchart of the operation of PSO is found in Figure 3.2.

Figure 3.2 – Flowchart of the PSO algorithm.

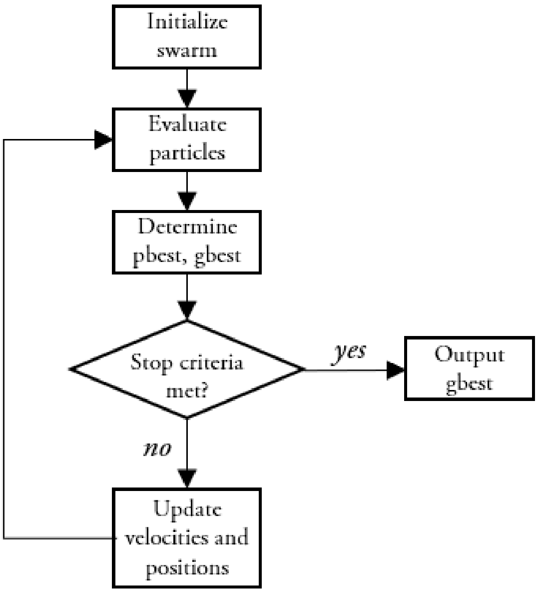

Source: The author.

3.3 Radial Movement Optimization (RMO)

3.3.1 Introduction

Recent studies on alternative metaheuristics led to a new swarm-based algorithm called Radial Movement Optimization, proposed by (RAHMANI & YUSOF, 2014). It shares similarities with the traditional and heavily adopted PSO in the sense that a population of particles are spread over a search space and their movements are governed by social and individual contributions.

The main difference of this novel algorithm lies in the nature and organization of the movement of the particles. The swarm is spread within a radius around a center point which is updated at each iteration (or generation). This way, positions and velocities for every particle are not transferred between generations, but the center location. Hence, it tends to reduce the memory requirement while offering comparable optimization efficiency.

The center location updating rule considers a local (called *radial*) best and a global best component, similarly to the velocity update equation in PSO. Cognitive and social coefficients guarantee a desirable balance between these two attributes. RMO has been applied into a variety of engineering problems, such as in (VANITHASRI *et al.*, 2016), (SEYEDMAHMOUDIAN *et al.*, 2016) and (VANITHASRI *et al.*, 2017).

3.3.2 Mathematical Description

Being N the number of particles in the swarm, and D the dimensionality of the search space, the initialization of the particles can be set as:

$$x_{i,j} = min_j + r_{i,j}(max_j - min_j)\,, \tag{3.6}$$

for a random distribution, where r is a random number within [0,1], or

$$x_{i,j} = \begin{cases} min_j & , \quad \text{if } i = 1 \\ x_{i-1,j} + step_j\,, & \text{if } i > 1 \end{cases}, \tag{3.7}$$

for a fixed-step distribution over the entire search space, where in both equations, $i = 1, \ldots, N$; $j = 1, \ldots, D$; min_j and max_j are, respectively, the minimum and maximum allowed values for the referred dimension; and

$$step_j = \frac{max_j - min_j}{N}\,. \tag{3.8}$$

After initialized, the particles are then evaluated according to a fitness function and a global best is determined, that is, the best evaluated particle, *Gbest*. The initial center position is assigned to this global best as well.

The velocity of each particle at the generation g is updated by:

$$v_{i,j}(g) = w(g) \times S_{i,j} \times Vmax_j\,, \tag{3.9}$$

where $S_{i,j}$ is a random number within [0,1] and

$$w(g) = w_{max} - g\left(\frac{w_{max} - w_{min}}{g_{max}}\right), \tag{3.10}$$

$$Vmax_j = \frac{max_j - min_j}{k}\,. \tag{3.11}$$

In Eq. (3.11), $Vmax_j$ becomes a constant for each dimension of the search space and k is a predefined constant, reasonably chosen before the algorithm starts execution. The maximum velocity defines the boundaries for the sprinkle of the swarm as it is inversely proportional to k. max_j and min_j are the maximum and minimum allowed values for the particles in the corresponding dimension.

The linearly decreasing inertia weight is defined in Eq. (3.10), in which w_{max} and w_{min} are the desirable maximum and minimum weights, and g_{max} is the predefined maximum number of generations (or iterations) the algorithm might take.

The position of the particles at the generation g is obtained by:

$$x_{i,j} = v_{i,j}(g) + c_j(g)\,, \tag{3.12}$$

in which $c_j(g)$ is the center location for the referred dimension at the current generation. Figure 3.3 illustrates how the swarm is sprinkled.

Figure 3.3 – Particles are sprinkled around a center point.

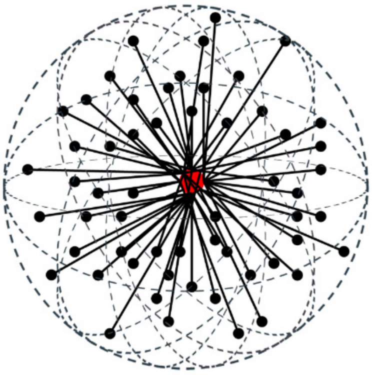

Source: Adapted from (RAHMANI & YUSOF, 2014).

An evaluation of this new swarm takes place and determines the local best particle, i.e., the *Rbest*. The center position must then be updated following Eq. (3.13):

$$c_j(g+1) = c_j(g) + c_1\left(Gbest(g) - c_j(g)\right) + c_2\left(Rbest(g) - c_j(g)\right), \tag{3.13}$$

where c_1 and c_2 are the social and cognitive learning rates, respectively, defined within $(0,1]$. Figure 3.4 shows the update procedure of the center and the new positions of the particles at the next generation.

Figure 3.4 – The update of the center through consecutive generations.

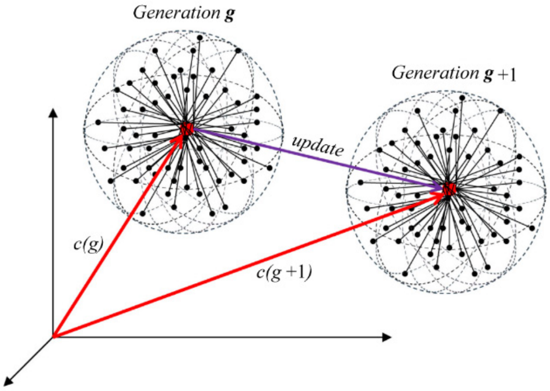

Source: Adapted from (RAHMANI & YUSOF, 2014).

After updating the center position, *Gbest* becomes

$$Gbest(g+1) = \begin{cases} Rbest(g)\,, & \text{if } \ fit(Rbest) > fit(Gbest) \\ Gbest(g)\,, & \text{otherwise} \end{cases}. \tag{3.14}$$

3.3.3 *Flowchart*

The flowchart of the RMO algorithm is explained in the illustration of Figure 3.5.

Figure 3.5 – Flowchart of the RMO algorithm.

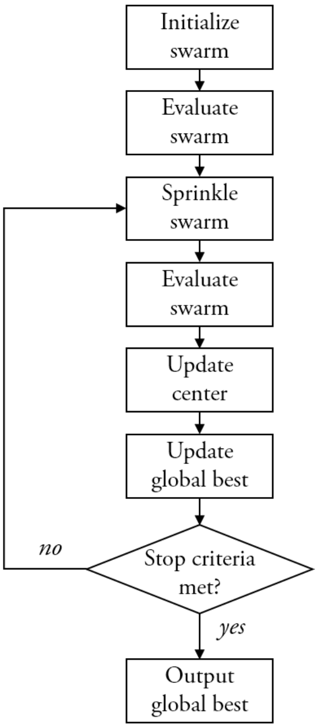

Source: The author.

3.4 Metaheuristics and the MPP tracking

As seen in section 2.4, metaheuristics like the ones presented in the current chapter have long been explored in the MPPT subject, precisely when it concerns the mitigation of the Partial Shading phenomenon. The reason for such interest lies on the nature of the problem, which can be viewed as an optimization effort of the energy that can be collected from a photovoltaic system at a moment in time.

In a PV system under partial shading, the emergence of a multimodal curve on the Power versus Voltage relation opens huge space for an optimization algorithm to work on. This work considers the voltage range of the PV array (or the duty cycle range; refer to 4.4.1) as the search space with dimensionality equal to 1, and the fitness function given by the product of a voltage "candidate" – determined by the algorithm – with its measured current. Finding the optimal operating point – i.e., the fittest candidate – may be achieved by any of the metaheuristics widely known in the academia. However, for the reasons explained in the next chapter (subsection 4.4.1), the author has proposed a variant of the relatively recent RMO.

4 THE INTELLIGENT MPP TRACKER

4.1 Overview

Noticeable from what has been studied in the previous sections, finding the maximum power point in a photovoltaic system can be seen from the point of view of an optimization problem which evolutionary or swarm-based algorithms reveal high advantage in dealing with. In this regard, an intelligent MPPT is proposed in this work, developed around the concepts of the Radial Movement Optimization algorithm.

Understanding how an MPPT achieves its objectives requires comprehending the role of each component in a PV system. Basically, the solar photovoltaic array connects to a power converter, and the MPPT acts on the converter parameters so to impose the optimal operating point of the array. Figure 4.1 depicts the interconnection of the basic components within a PV system with MPP tracking capabilities.

Figure 4.1 – Diagram of an MPPT-controlled PV system.

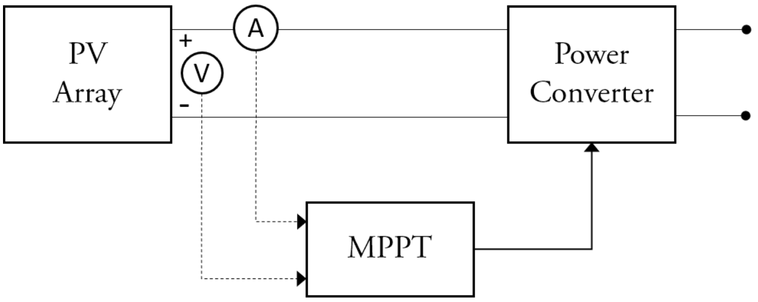

Source: The author.

The scope of this research, however, is solely limited to the MPPT subsystem, but essential understanding of the other components becomes necessary. The next subsections will present some brief explanation thereof.

4.2 The PV Array

The source of power that converts sunlight into DC electricity is herein referred to, in a generic form, as the PV Array. As seen in chapter 2, arrays are an association of PV modules with the purpose of delivering higher voltages and currents than a single module could do. Series association means that the voltages from each module are added, while parallel association adds up the currents. It is commonplace the combination of these two schemes, especially in large PV arrays.

The PV array studied in this research, available at the Alternative Energies

Laboratory (LEA – *Laboratório de Energias Alternativas*) of the Federal University of Ceará, is composed of a single string of six modules with a total capacity of 1.5 kWp (kilowatt-peak). Each module has the set of parameters specified in Table 4.1.

Table 4.1 – Electrical parameters of the module YL250P-29b from Yingli Solar.

Characteristic	**Value**	**Unity**
Module efficiency	15.3	%
Output power	250 −0/+5	W
Voltage at max power	30.4	V
Current at max power	8.24	A
Open-circuit voltage	38.4	V
Short-circuit current	8.79	A
NOCT	46 ±2	°C
Temperature coefficient of V_{OC}	−0.33	%/°C
Temperature coefficient of I_{SC}	0.06	%/°C
Operating temperature range	−40 to +90	°C

Source: (YINGLY SOLAR, 2013).

Each module, as seen in Figure 4.2, is manufactured with 60 series-connected multicrystalline silicon cells providing a total efficiency of 15.3% of solar energy conversion. Since the array is made of 6 modules in series, the open-circuit voltage of the array becomes $6 \times 38.4\ \mathrm{V} = 230.4\ \mathrm{V}$ while the short-circuit current remains the same, as in Table 4.1.

Figure 4.2 – One of the YL250P-29b modules that compose the array at LEA/UFC.

Source: (YINGLY SOLAR, 2013).

4.3 The Power Converter

The converter in a PV system is responsible not only for the power conditioning of the output signals but also for interfacing the PV array and the MPPT circuitry in such a way that the operating point of the PV source can be controlled.

In grid-connected systems, an inverter (DC to AC conversion) may directly interface the PV array and the utility grid, but this connection can also be accomplished in a two-stage approach, in which a DC/DC conversion is performed first and then the conditioning to the AC power grid takes place. This allows for more flexibility in the design and safety in the operation of the PV system since the DC source is decoupled from the utility grid or any other AC load. In fact, most of the PV systems employs a DC/DC converter to allow the MPP tracking while further conditioning may be applied conveniently in later stages. Topologies of PV systems have been deeply investigated in (VILLALVA, 2010; PINHO *et al.*, 2014) and is out of the scope of this work.

As for DC/DC converters, the three basic topologies extensively used in photovoltaic systems are: buck, boost, and buck-boost. They operate by reducing and/or increasing the output voltage while maintaining the energy conservation principle. When applied to MPP tracking, the role of the DC/DC converter, regardless of its topology, is to be perceived as a variable resistive load by the PV array, thus interfering on the output voltage and current of this power supply. Figure 4.3 illustrates this principle.

Figure 4.3 – The DC/DC converter working as a variable resistance as seen by the PV array.

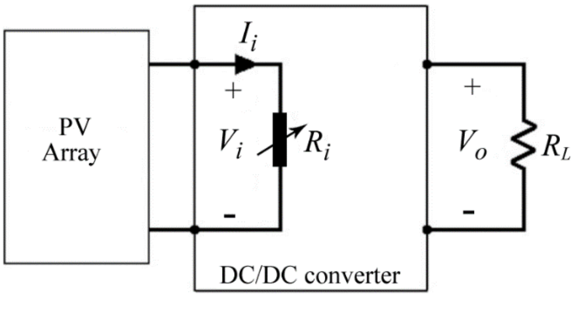

Source: Adapted from (ENRIQUE *et al.*, 2007).

The input resistance, R_i, is dependent on the load resistance, R_L, and the duty cycle[11] of the switching device. Therefore, considering a fixed load resistance, the input resistance – and, consequently, the output voltage and current of the PV array – can be adjusted

---

[11] Duty cycle, sometimes duty ratio, is the ratio between the period a switching device is kept closed (ON) and the total switching period (ON+OFF). It can be expressed in % or in the range [0, 1].

by changing the duty cycle, d, of the converter. Each converter topology has its own rules to govern this relation and they are expressed in Table 4.2.

Table 4.2 – Dependence of R_i on d and R_L for different DC/DC converter topologies.

Topology	**Input resistance, R_i, (CCM)**	**Input resistance, R_i (DCM)**	K_{crit}
Buck	$\frac{R_L}{d^2}$	$\frac{R_L}{4}\left(1+\sqrt{1+\frac{4K}{d^2}}\right)^2$	$1-d$
Boost	$R_L(1-d)^2$	$\frac{4R_L}{\left(1+\sqrt{1+\frac{4d^2}{K}}\right)^2}$	$d(1-d)^2$
Buck-Boost	$\frac{(1-d)^2R_L}{d^2}$	$\frac{KR_L}{d^2}$	$(1-d)^2$

Source: Adapted from (ENRIQUE *et al.*, 2007).

Considering the switching nature of the converters, there is a constant K for each topology that commands its operation mode either in the continuous conduction (CCM) or in the discontinuous conduction modes (DCM). K is a function of the equivalent inductance (L_{eq}) of the converter, the load resistance (R_L) and the switching period (T_S), as in Eq. (4.1):

$$K = \frac{2L_{eq}}{R_L T_S}. \tag{4.1}$$

Whenever $K < K_{crit}$, the converter will operate in DCM, that is, the current flowing through the inductor will periodically be zero. Conversely, in CCM this will not happen, which allows for simpler analysis of the operation of the converters.

When in CCM, the output to input voltage and current relations for the three converter topologies are expressed in Table 4.3:

Table 4.3 – Output to input relation of voltages and currents for the different converter topologies.

Topology	${V_o}/{V_i}$	${I_o}/{I_i}$
Buck	d	$\frac{1}{d}$
Boost	$\frac{1}{1-d}$	$1-d$
Buck-Boost	$-\frac{d}{1-d}$	$-\frac{1-d}{d}$

Source: Adapted from (COELHO *et al.*, 2009).

The choice for the converter topology or its variants may be led by a number of reasons that escape the purpose of the present research. Despite that, valuable studies, as in (ENRIQUE *et al.*, 2007; COELHO, *et al.*, 2009; COELHO *et al.*, 2010) analyzed different converters applied to the MPPT problem and concluded that the buck-boost topology, extended to the Ćuk, SEPIC and ZETA variants, reveal better performances than the single buck or boost ones. By their analysis, these step-down and step-up converters could fail in tracking the MPP on certain conditions, a limitation that the combined circuit does not hold. For that reason, the buck-boost topology was adopted in this research work.

4.4 The MPPT

4.4.1 Introduction

In the previous subsection it was shown that the power converter plays an important role in the MPP tracking effort by imposing the operating point of the PV source according to a change in the duty cycle of the switching element that is part of it. It is, thereby, a straight association that the MPPT strategy should work directly on the switching behavior of these devices. Nevertheless, many MPPT solutions propose to indirectly manipulate the duty cycle by employing a controller before the converter while working on different control variables, such as the voltage or the current of the PV array. Such strategies are aimed at improving the transient responses and minimizing the settling time of the PV source attached to the power converter, however to the detriment of simplicity and overall cost of the solution. Figure 4.4 depicts both strategies within the system.

Figure 4.4 – Different control strategies with (a) direct and (b) indirect duty cycle manipulation. The Pulse Width Modulation (PWM) block generates the proper signal to drive the switching device of the power converter according to the input duty ratio, d.

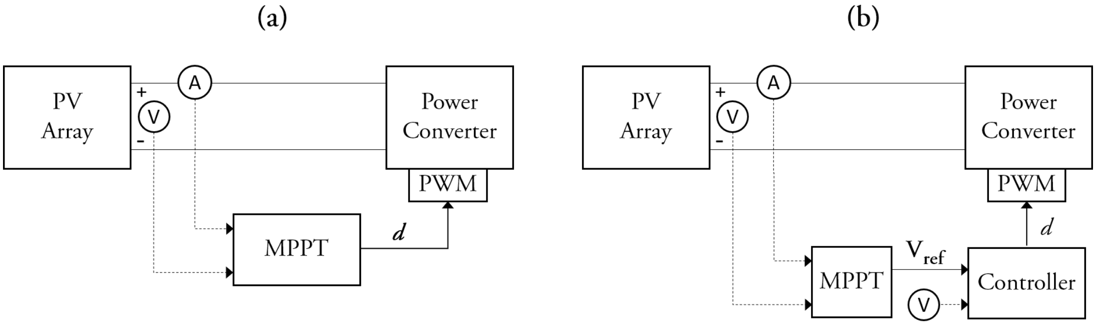

Source: The author.

It is far from the scope of this research to investigate which strategy performs better, especially because this leaves much room for another research. For example, in (VILLALVA,

2010) it is supported that one should ideally try to use the controller strategy, whereas in (ELGENDY *et al.*, 2014), both approaches are assessed, revealing that the direct duty cycle manipulation has its benefits while still showing some drawbacks, pretty much the same with the controller approach.

In spite of that and taking into account the criteria stated in subsection 2.3.2 for assessing MPPT techniques, a brief analysis can be made to support the choice for one or another strategy:

i. *Ability in differentiating local and global maximum points*: The proposed algorithm is based on an optimization technique that inherently distinguishes local and global maxima by using a fitness function. The strategy for duty cycle manipulation does not interfere with this characteristic.

ii. *Ability to locate the global maximum point*: As in the previous topic, there is an inherent characteristic of the proposed algorithm in converging to the global maximum point. Again, it is independent from the strategy for duty cycle manipulation.

iii. *Celerity in tracking the MPP under varying environmental conditions*: This parameter is highly dependent on the settling time of the PV source plus the power converter systems. This implies that the indirect duty cycle manipulation, that is, the controller approach, provides better performance since the settling time of the system can be reduced and, consequently, fast convergence to the maximum power point can be achieved. As for the algorithmic strategy, the Radial Movement Optimization technique proposes faster convergence when compared to other evolutionary or swarm-based optimization algorithms.

iv. *Stability or minimal oscillation in the steady-state*: This represents an issue when considering classical MPPT techniques, such as P&O, but most of the intelligent approaches overcome the oscillatory characteristic around the MPP. Concerning the control strategy, (ELGENDY *et al.*, 2014) claim that the direct duty cycle manipulation improves the stability of the MPP.

v. *Dependability on system-specific parameters*: This is directly related to the control strategy. Working on the system voltage or current – as is the case with indirect duty cycle control – means that the open-circuit voltage and/or the short-circuit current of the PV array must be known in advance to guarantee proper operation of the MPPT algorithm. This imposes a large dependence on the PV system from which maximum power must be extracted. Direct duty cycle manipulation surmounts this dependence by setting a predefined range of operation within]0, 1[.

vi. *Complexity or cost of the solution*: Indirect duty cycle manipulation requires an additional effort of designing a suitable control strategy for the converter system. This controller, either in hardware or software forms, implies enhanced complexity and also increases the overall cost of the MPPT system. On the other hand, direct duty cycle manipulation eliminates the need for a controller interfacing the power converter, which simplifies the design and allows for low-cost microprocessors to be employed in the MPPT solution.

Based on this analysis, the direct manipulation of the duty cycle adheres with most of the criteria exposed and, thus, it is the choice for the present work. As for criterion (iii), the absence of the controller entails an increase in the settling time of the PV array. Such loss in celerity can be balanced with the fast convergence characteristic of the RMO algorithm. Hence, the overall convergence speed of this solution can be comparable with conventional intelligent strategies that usually employ slower algorithms.

Concerning the Radial Movement Optimization algorithm, essentially fast in the generalized proposal, when used in this specific application, some considerations and improvements can be suggested. They are highlighted in the next subsection.

4.4.2 Modified Radial Movement Optimization (mRMO)

Applied to the MPPT problem and assuming a direct duty cycle manipulation, the unidimensional, i.e., $j = 1$, search space is represented by the variable d that is constrained in the interval $0 < d < 1$. Therefore, considering Eq. (3.7) with a slight modification, the initialization of the N particles can be performed as:

$$x_i = \begin{cases} step & , \text{ if } i = 1 \\ x_{i-1} + step , & \text{ if } i > 1 \end{cases} ; \text{with } i = 1, \ldots, N, \tag{4.2}$$

in which

$$step = \frac{1}{N+1} . \tag{4.3}$$

From the viewpoint of an optimization algorithm, N should be sufficiently large to maximize the probability of finding the global optimal point. Notwithstanding, when applied to the MPPT problem, it is important that N does not grow large since it could represent exceeded convergence time in detecting the global MPP. In the literature, it is common to use less than 10 particles as a tradeoff between accuracy and speed.

Another consideration refers to the velocity of the particles, defined in Eqs. (3.9)–(3.11). The maximum velocity defines the boundaries of the sprinkle and depends on a constant k. Considering the length of the search space, k would be ideally set to 2, leading Eq. (3.11) to:

$$Vmax = \frac{1}{k}\text{, where } k = 2. \tag{4.4}$$

4.4.2.1 Proposed Modifications

In addition to the aforementioned considerations that must be made, the modifications proposed to the original RMO algorithm can be summarized as:

i. Extend the range of the random values: Better distribution of the particles positively affects the quality/accuracy of the search;

ii. Propose a Lorentzian decay, as in Eq. (4.5), for the weight variable: The proposed curve shape allows continuous exploration all over the search space during the initial iterations and rapid convergence thereafter. This helps reducing the probability of the algorithm to fall into a local maximum (when PSC occur) in the beginning of the execution, while simultaneously accelerates convergence;

iii. Rearrange the *center* and the *global best* update steps: Seeks to improve the convergence speed by forcing the new center position to be attracted with increased strength towards the best particle of each iteration.

Eq. (3.9) suggests a random value, S, within [0, 1] in the equation of the velocities, but that would constrain the sprinkle of the particles to lie solely on the right side of the center, wherever it should be located. Therefore, the interval of the random number S would ideally be [-1, 1] to conform the locations of the particles on both sides of the center point. These two modifications are graphically visualized in Figure 4.5:

Figure 4.5 – The proposed modifications allows the sprinkle of particles to lie on both sides of the center point, c, along the radius defined by V_{max}.

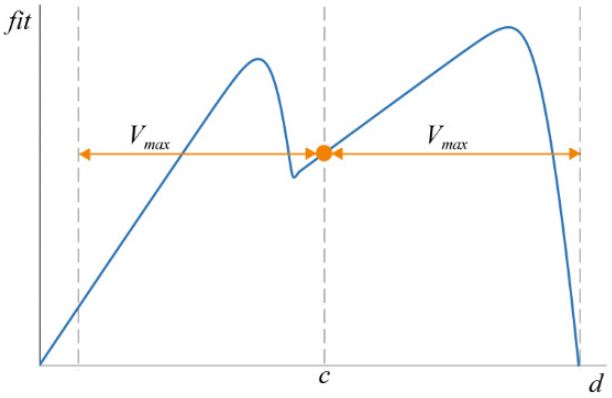

Source: The author.

Yet in Eq. (3.9), it defines an inertia weight that shrinks the radius V_{max} at each iteration. Eq. (3.10) defines a linear decaying method for the inertia weight, but a more adequate behavior considering the MPPT problem would be given by the following equation:

$$w(g) = \frac{1}{1 + \left(\frac{g}{0.25 \times g_{max}}\right)^{10}}. \tag{4.5}$$

The idea of using such decaying behavior is to allow the algorithm to continuously spread the swarm within the whole search space for the first iterations and then rapidly constrain the search scope to accelerate convergence to the MPP. It is assumed that after about 10% of the maximum number of iterations, the algorithm has already found a region within which there is a high probability of the GMPP to exist. Figure 4.6 depicts the decaying of the inertia weight for the original RMO and for the modified version, considering g_{max} = 100 iterations.

Figure 4.6 – Proposed weight decaying and the original linear decaying.

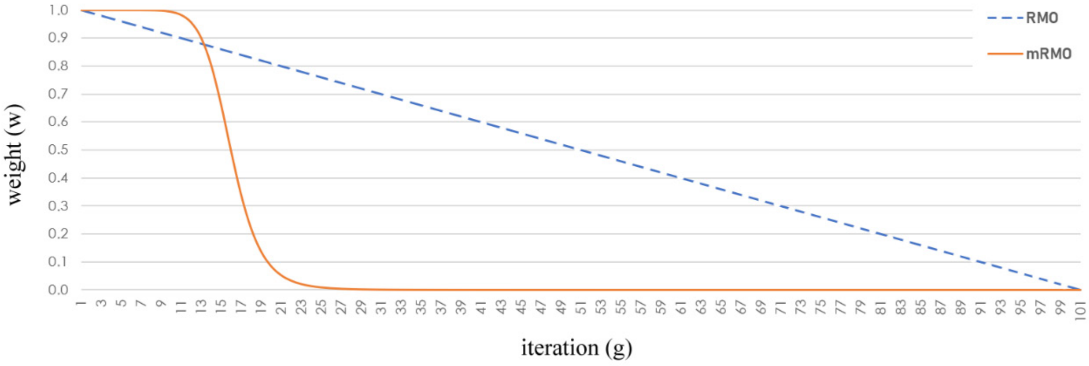

Source: The author.

The effect of this modification is graphically observed when comparing Figure 4.7

against Figure 4.8, where faster convergence is observed with the Lorentzian decaying.

Figure 4.7 – The shrinking of the radius around the center point along 18 iterations with the proposed Lorentzian decaying of the inertia weight.

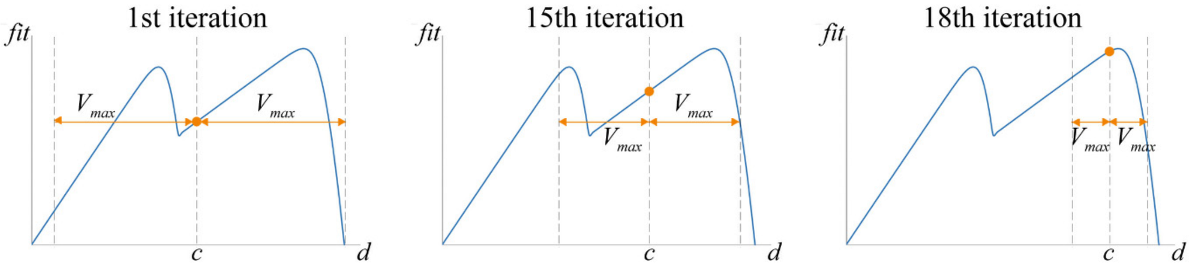

Source: The author.

Figure 4.8 – The shrinking of the radius around the center point along 18 iterations with a linear decaying of the inertia weight as in the original RMO.

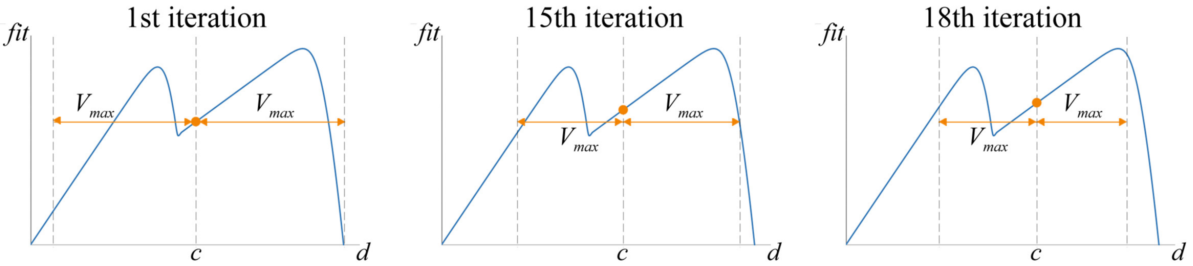

Source: The author.

The last modification proposed is related to the order of execution of the last steps of the algorithm, that is, the update of the center point and the update of the global best particle. In the original proposal, the center location is updated using the information of the global best and the radial best particles, regardless of whether the latter has improved the fitness or not. By exchanging the order of these two steps, whenever a radial best particle improves the fitness, it attracts the center point to its location with increased strength. The behavior remains unchanged for the opposite case.

All these modifications will be assessed in the next chapter, specifically in the section that explains the offline test procedures, when the proposed modification of the RMO will be tested against the original RMO, the PSO and the DE algorithms.

5 SIMULATION RESULTS

In this chapter the methodology used for validating the proposed MPPT in the simulation environment must be introduced before presenting the results.

5.1 Test Methodology

Two approaches were determined to test the proposed intelligent MPPT: the *offline approach*, in which a set of P-V curves representing several environmental conditions are experienced; and the *online approach*, that simulates a real operation of the PV system, where the MPPT should continuously seek for the maximum power point in runtime.

For the offline approach, the P-V curves are stored in memory and represent a fixed condition of irradiance and temperature. Multiple P-V curves denote different environmental circumstances and are useful to validate the algorithms under distinct levels of difficulty. In such approach, there is no need to sense the voltage and current – the power, actually – from the PV array since this information is already available in memory. The idea is to assess the ability of the algorithms in finding the global MPP (GMPP) while neglecting the effect of time. It is like taking a snapshot of the current irradiance and temperature that hit the photovoltaic panels and check whether the GMPP can be properly detected or not. Under uniform irradiance conditions, both classical and intelligent MPPTs are expected to find the MPP without much problem. When PSC occurs, the ability of the classical algorithms in detecting the GMPP is highly dependent on the starting point of the search, a characteristic that the intelligent trackers do not exhibit.

As for the online approach, the whole PV system as depicted in Figure 4.4(a) with the addition of a resistive load at the output of the power converter is implemented in the simulation environment of Simulink®. In this approach, real irradiance and temperature data are used to evaluate the algorithms. These environmental profiles were captured from a cloudy day on March 12, 2018 in Fortaleza, Ceará, at the laboratory of alternative energies of the Federal University of Ceará (LEA/UFC). The idea is to assess the ability of the algorithms[12] in tracking the GMPP under a real operating scenario, where rapid changes in power generation are expected due to stochastic changes in the atmospheric conditions.

---

[12] For the sake of simplicity and conciseness, only mRMO and P&O will have results presented in subsection 5.3. P&O represents one of the most common MPPT techniques commercially available, justifying its usage as the reference tracker in the online test approach.

5.2 Offline Approach

To validate the intelligent and classical algorithms under distinct conditions, a set of P-V curves was captured to portray real circumstances. The proposed algorithm is compared against the original RMO, PSO and DE. The classical P&O and IncCond are also experienced with the same set of curves. These curves are depicted as follows.

The curve in Figure 5.1 represents the ideal scenario for a PV system: A Uniform Irradiance Condition (UIC) that imposes no difficulty for the algorithms, either classical or intelligent ones, to detect the MPP.

Figure 5.1 – P-V curve with a single MPP at 182.4 V and 1503.15 W.

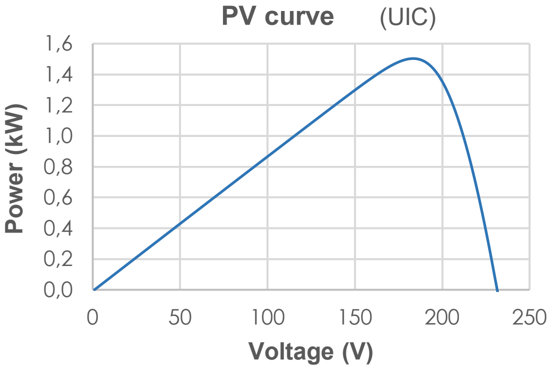

Source: The author.

Figures 5.2 to 5.4 represent, with different degrees of difficulty, the non-ideal scenarios of Partial Shading. Under these conditions, much effort is expected from the execution of the intelligent algorithms. As for the classical ones, whether they will find the GMPP or not is essentially bound to the starting point of the search. This characteristic will be clearly seen with the graphs exposed in the next subsection.

Figure 5.2 – P-V curve with the global MPP at 120.3 V and 990.58 W.

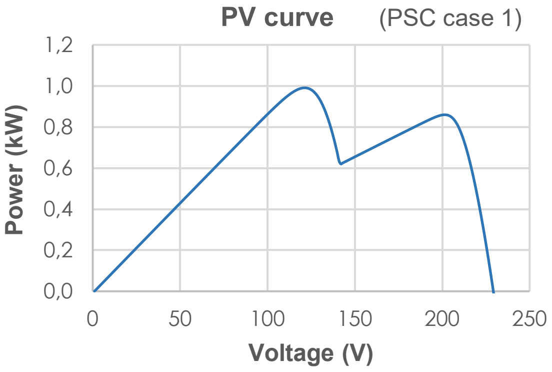

Source: The author.

Figure 5.3 - P-V curve with the global MPP at 128 V and 652.02 W.

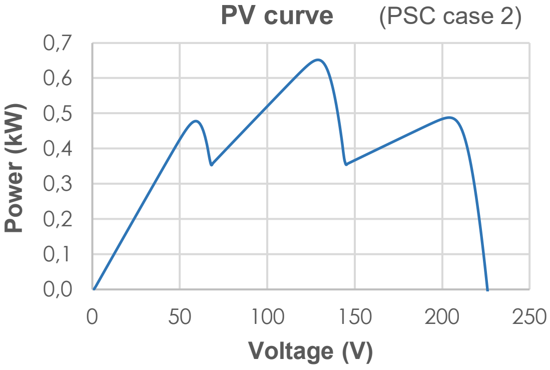

Source: The author.

Figure 5.4 – P-V curve with the global MPP at 58.2 V and 477.98 W.

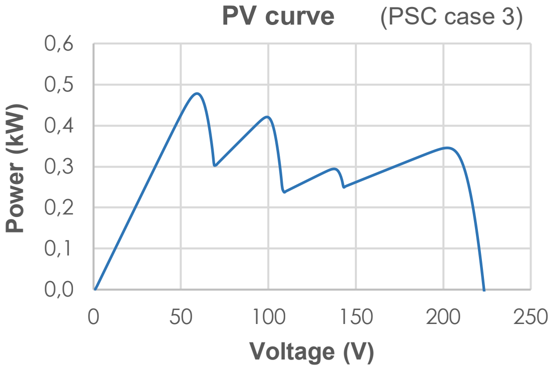

Source: The author.

Figure 5.5 - P-V curve with the global MPP at 59.3 V and 439.74 W.

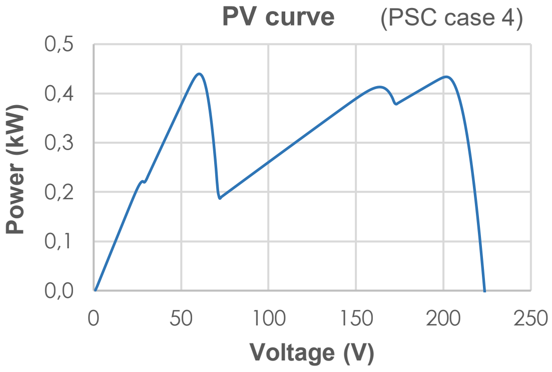

Source: The author.

For the purpose of conciseness, when presenting the results of the simulations with the classical algorithms, only the curves from Figures 5.1 and 5.5 will be exercised with a number of distinct conditions. It is assumed that such strategy should be enough to enlighten the behavior of these algorithms from a simple to a complex test scenario.

The parameters used for the intelligent algorithms are listed in the following tables:

Table 5.1 – Parameters of the proposed algorithm, mRMO.

Parameter	**Value**
Number of particles	10
Global acceleration coefficient	0.4
Radial acceleration coefficient	0.9
Max number of iterations	100
Stop Criterion	Convergence of the global best after the 15th iteration

Source: The author.

Table 5.2 – Parameters of the RMO algorithm.

Parameter	**Value**
Number of particles	10
Global acceleration coefficient	0.4
Radial acceleration coefficient	0.9
Max number of iterations	100
Stop Criterion	Convergence of the global best after the 15th iteration

Source: The author.

Table 5.3 – Parameters of the PSO algorithm.

Parameter	**Value**
Number of particles	10
Social acceleration coefficient	0.4
Cognitive acceleration coefficient	0.9
Inertia weight	0.25
Max number of iterations	100
Stop Criterion	Convergence of the global best after the 15th iteration

Source: The author.

Table 5.4 – Parameters of the DE algorithm

Parameter	**Value**
Number of individuals	10
Crossover factor	0.9
Weight factor	0.25
Max number of iterations	100
Stop Criterion	Convergence of the global best after the 15th iteration

Source: The author.

For all intelligent techniques, the fitness function is the power obtained from the PV array for a given individual/particle. It must be noted that the power is read from memory – the P-V curves in Figs. 5.1 to 5.5 – instead of sensed from the array since it represents the offline approach. The next subsection brings the outcomes of the classical, followed by the intelligent techniques.

5.2.1 Classical Algorithms

The classical algorithms, P&O and IncCond, operate in a well determined manner, that is, should the initial parameters be the same, the outputs will not differ. Therefore, different starting points and perturbation step sizes are exercised and shown in the following figures.

Figure 5.6 – The classical P&O under the UIC of Figure 5.1 starting at 220 V.

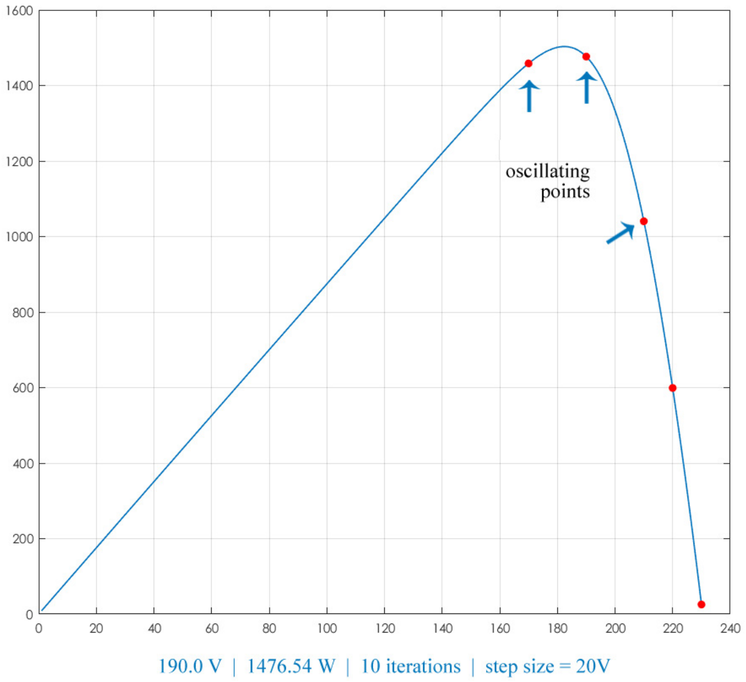

Source: The author.

Figures 5.6 – 5.8 refer to the simplest case of a uniform irradiance condition where the MPP lies around 1503 W. The starting point for all three cases is the same (220 V). The P&O algorithm in Figure 5.6 will impose the PV system to oscillate at those three red points on the curve for a step size of 20 V, obtaining a major power of 1476.54 W. In Figure 5.7, the oscillation is set within a reduced range because of a smaller step size of 10 V adopted, which led the PV system to approach 1500 W at the peak point. A minimum oscillation is observed in Figure 5.8 when the step size is set to 1 V and the MPP is near 1503 W. This benefit in accuracy due to smaller step sizes is balanced with longer convergence time.

Figure 5.7 – The P&O under the UIC of Figure 5.1 for a step size of 10 V.

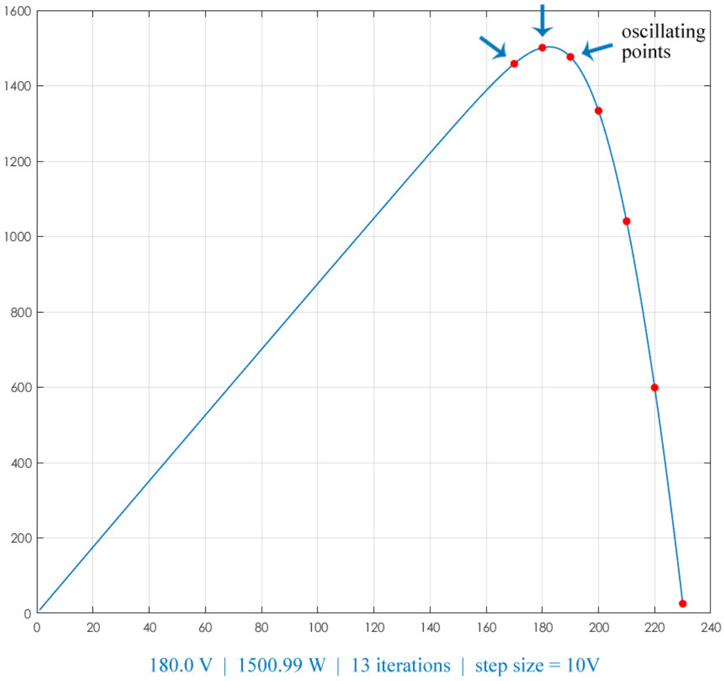

Source: The author.

Figure 5.8 – The performance of P&O with a step size of 1V.

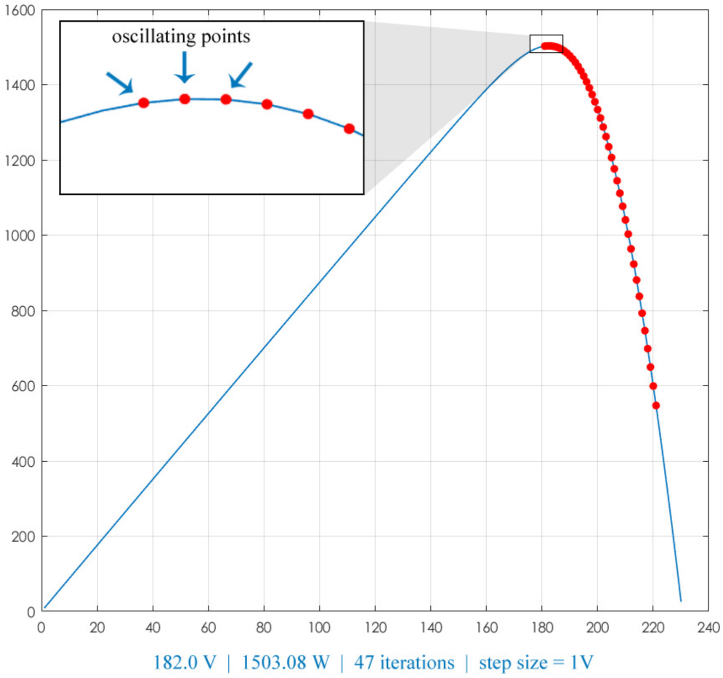

Source: The author.

Figure 5.9 – The P&O under the PSC of Figure 5.5 when starting from 220 V.

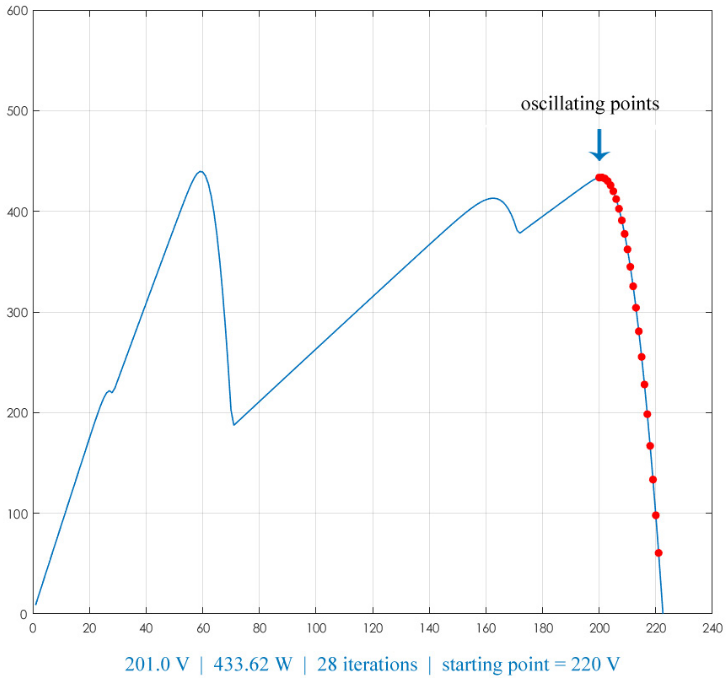

Source: The author.

Figure 5.10 – The P&O in the same PSC of the previous figure, starting from 150 V.

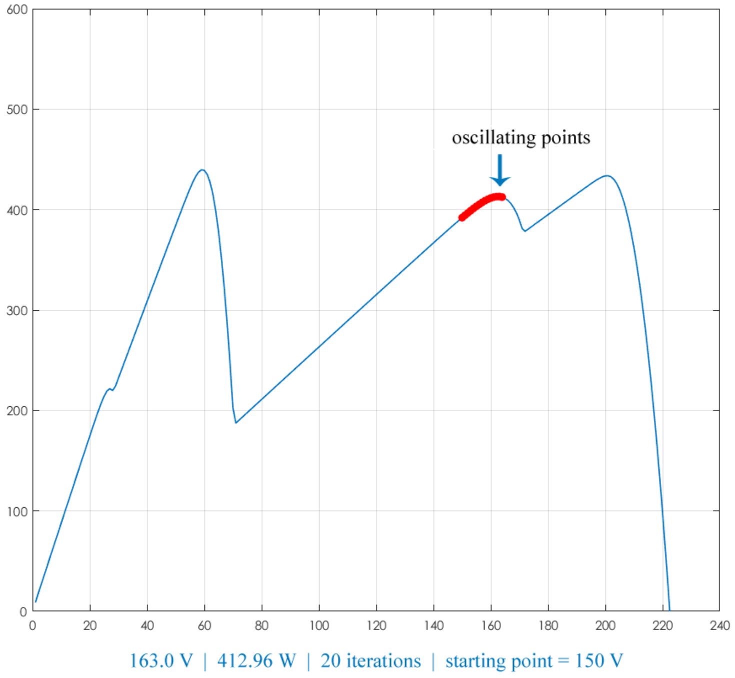

Source: The author.

Figure 5.11 – The P&O in the same PSC of the previous figure, starting from 70 V.

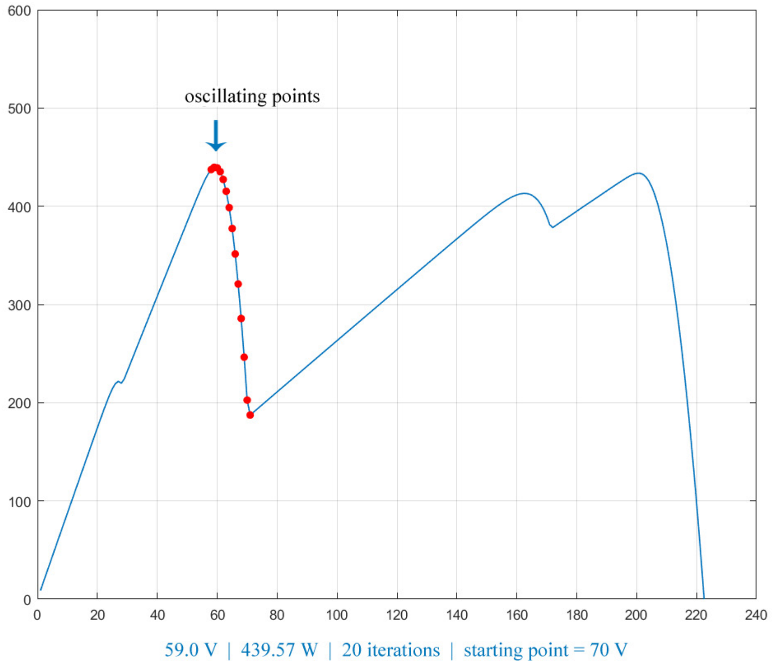

Source: The author.

Figures 5.9 to 5.11 refer to a challenging partial shading condition where the GMPP is found at 439.74 W but two local maxima are also present. The three simulations differ only in the starting point of the P&O algorithm, being the step size fixed at 1 V. The curve in Figure 5.9 indicates that P&O made the PV system to operate around 433 W, oscillating at three points. This, however, corresponds to one of the local maxima, not the desired GMPP. In Figure 5.10, P&O set the operating point to oscillate around 412 W, another local MPP. The GMPP could only be found when the starting point of the P&O algorithm was set to 70 V, as depicted in the curve of Figure 5.11.

The following figures show the results of the simulations for the Incremental Conductance (IncCond) algorithm. Figures 5.12 – 5.14 refer to the simpler case of a uniform irradiance condition where the MPP lies around 1503 W. The starting point for all three cases is the same (220 V). The IncCond algorithm in Figure 5.12 will impose the PV system to operate at a steady point on the curve for a step size of 20 V, obtaining a power of 1476.54 W. In Figure 5.13, the MPP oscillates around 1500 W when a smaller step size of 10 V is adopted. A steady operating point is observed in Figure 5.14, when the step size was set to 1 V and the MPP is found at 1503.08 W. The difference in performance from P&O to IncCond is that the latter can achieve operating points with no oscillations in some circumstances.

Figure 5.12 – The IncCond algorithm under the UIC of Figure 5.1 with a step size of 20 V.

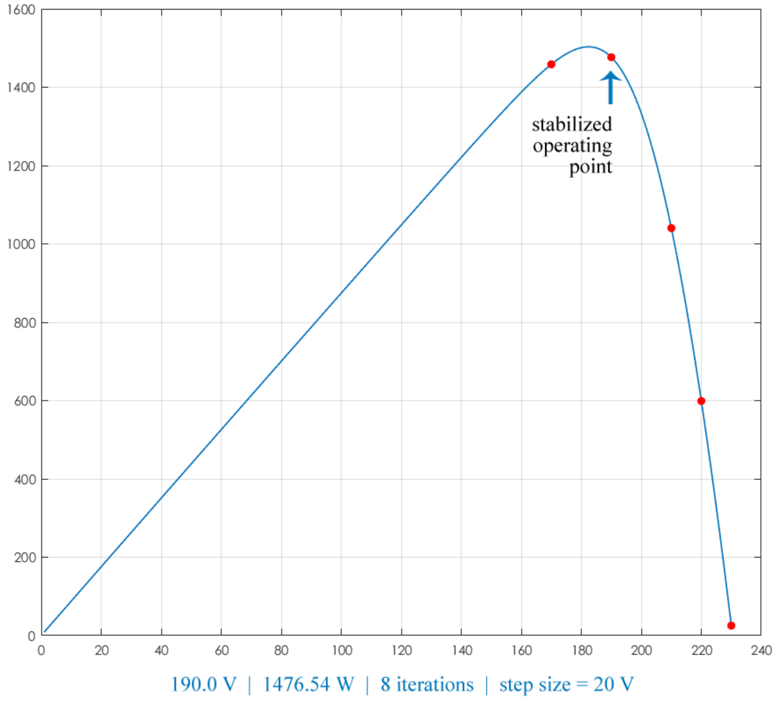

Source: The author.

Figure 5.13 – The IncCond algorithm under the same UIC of the previous figure with a step size of 10 V.

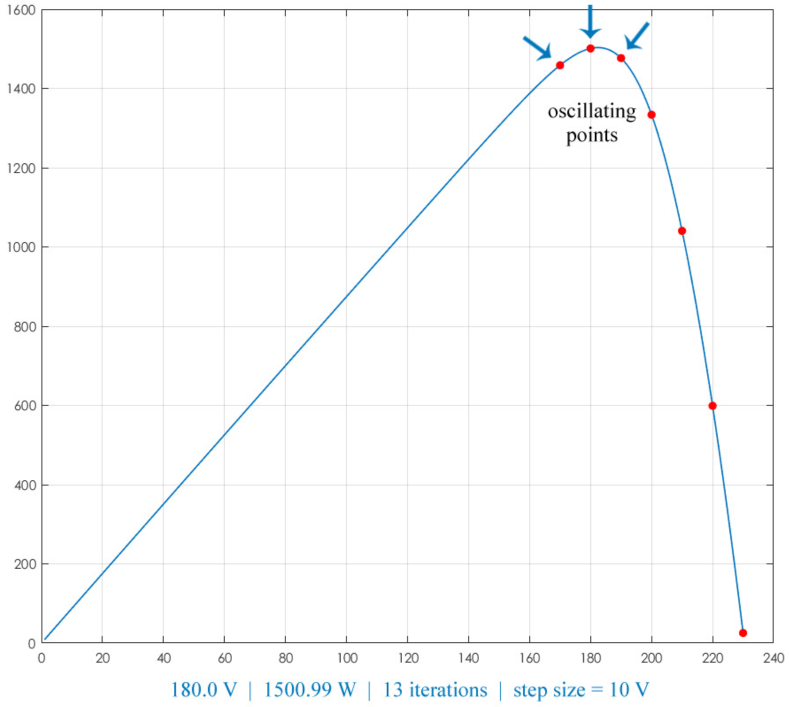

Source: The author.

Figure 5.14 – The IncCond under the same UIC of the previous figure with a step size of 1 V.

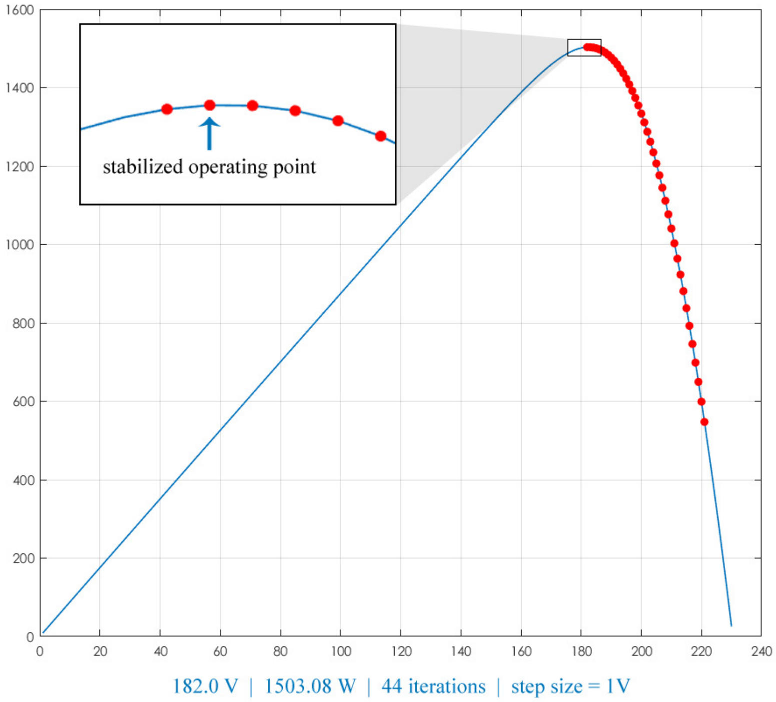

Source: The author.

Figures 5.15 to 5.17 refer to the challenging partial shading condition where the GMPP is found at 439.74 W but two local maxima are present. The three simulations differ only in the starting point of the IncCond algorithm, being the step size fixed at 1 V. The curve in Figure 5.15 indicates that IncCond made the PV system to operate at 433.53 W. This, however, corresponds to one of the local maxima, not the desired GMPP. In Figure 5.16, IncCond set the operating point to 412.96 W, another local MPP. The GMPP could only be found when the starting point of the algorithm was set to 70 V, as depicted in the curve of Figure 5.17.

Figure 5.15 – The IncCond algorithm under the PSC of Figure 5.5, starting from 220 V.

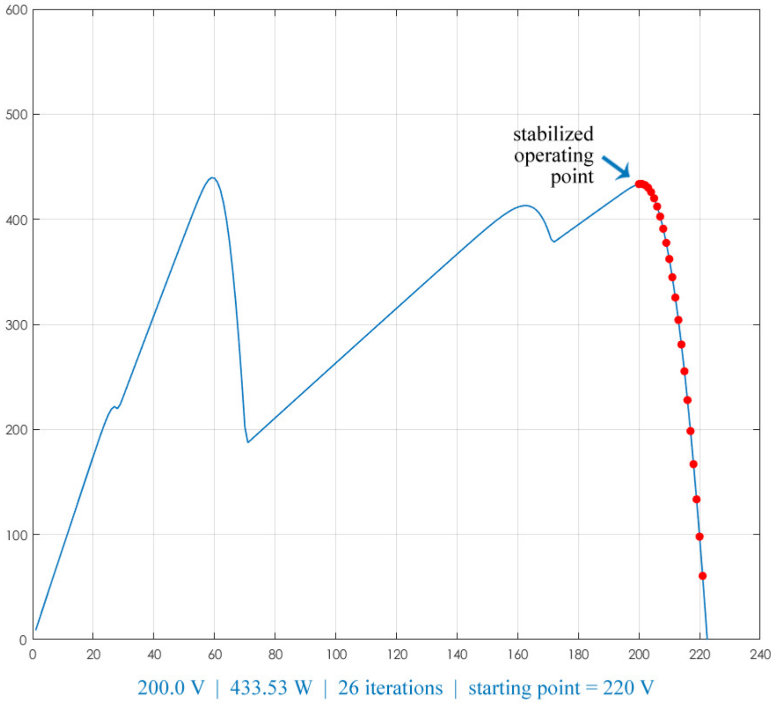

Source: The author.

Figure 5.16 – The IncCond algorithm under the same PSC as in the previous figure, but starting from 150 V.

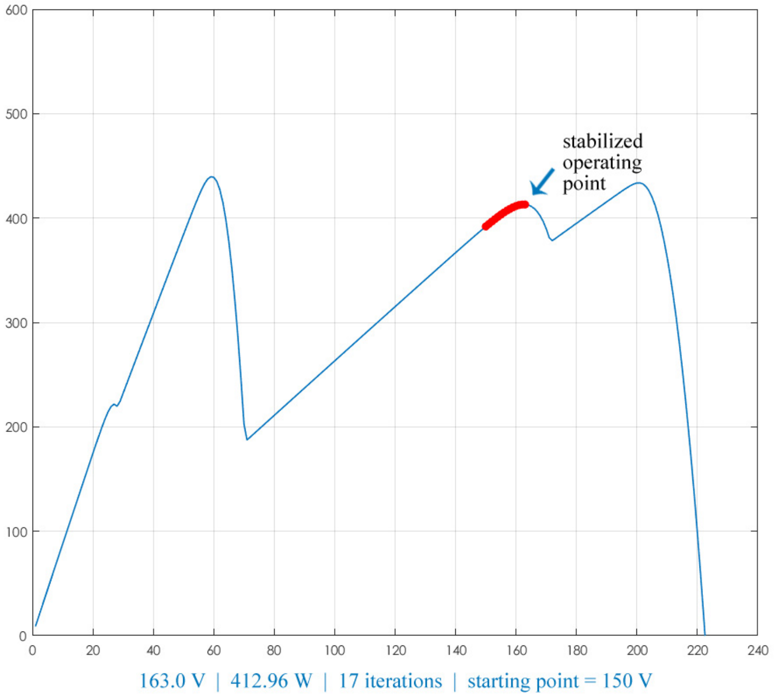

Source: The author.

Figure 5.17 – The IncCond algorithm under the same PSC as in the previous figure, but starting from 70 V.

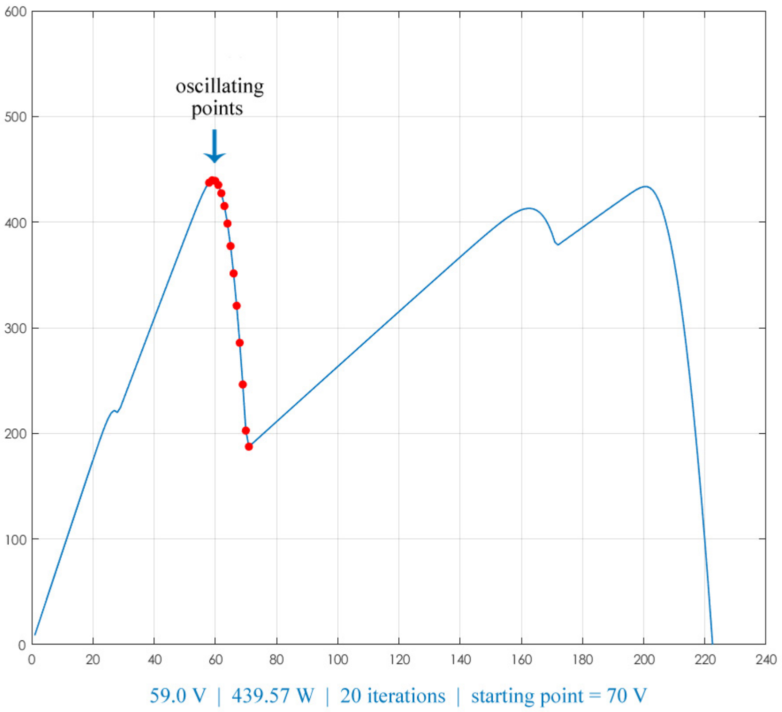

Source: The author.

5.2.2 *Intelligent Algorithms*

The intelligent algorithms involve random procedures in their operation, hence, to properly validate these techniques, they must be exercised for many runs as possible, with statistical metrics being extracted. These outcomes are expressed in the tables[13] that follow.

The efficiency of the algorithms is also presented and is calculated as:

$$\text{Efficiency} = \left(1 - \frac{abs(P_{obtained} - P_{GMPP})}{P_{GMPP}}\right) \times 100\,. \tag{5.1}$$

Table 5.5 – The performance of the proposed algorithm, mRMO, under the UIC of Figure 5.1 for 500 simulations. Low standard deviations mean high accuracies.

Metric	**Voltage**	**Power**	**Number of iterations**
Mean (μ)	182.51	1502.74	17.13
Standard Deviation (σ)	1.021	1.001	2.127
Efficiency		99.97%	

Source: The author.

---

[13] There is no use exposing 500 figures for each tested algorithm, therefore, tables are employed since they better suit the nature of the information. As tables are concise, all test scenarios from Figures 5.1 to 5.5 are presented.

Table 5.6 – The performance of the proposed algorithm, mRMO, under the PSC of Figure 5.2 for 500 simulations. Low standard deviations mean high accuracies.

Metric	**Voltage**	**Power**	**Number of iterations**
Mean (μ)	120.31	990.04	17.12
Standard Deviation (σ)	0.972	1.298	2.561
Efficiency		99.94%	

Source: The author.

Table 5.7 – The performance of the proposed algorithm, mRMO, under the PSC of Figure 5.3 for 500 simulations. Low standard deviations mean high accuracies.

Metric	**Voltage**	**Power**	**Number of iterations**
Mean (μ)	127.85	651.45	17.18
Standard Deviation (σ)	0.922	0.923	2.295
Efficiency		99.91%	

Source: The author.

Table 5.8 – The performance of the proposed algorithm, mRMO, under the PSC of Figure 5.4 for 500 simulations.

Metric	**Voltage**	**Power**	**Number of iterations**
Mean (μ)	98.86	437.34	17.17
Standard Deviation (σ)	63.56	2.710	2.169
Efficiency		99.45%	

Source: The author.

Table 5.9 – The performance of the proposed algorithm, mRMO, under the PSC of Figure 5.5 for 500 simulations. Low standard deviations mean high accuracies.

Metric	**Voltage**	**Power**	**Number of iterations**
Mean (μ)	58.11	476.82	17.56
Standard Deviation (σ)	1.01	2.433	2.908
Efficiency		99.75%	

Source: The author.

From Table 5.8, the high standard deviation in the voltage means that for some simulation runs, the algorithm may have reached local MPPs at 162 V (413 W) or 200 V (433 W), although the mean voltage at 98.86 V means that most of the resulting output power was at the GMPP of 59.3 V (439.74 W).

It is seen from the charts that the proposed mRMO algorithm reveals remarkable accuracy and relatively fast tracking ability of the GMPP in terms of the iterations needed to converge. The low standard deviations of the voltage, power and number of iterations ensure that even depending on random procedures, the algorithm reliability remains high. The next charts bring the outcomes of the original RMO algorithm.

Table 5.10 – The performance of the RMO algorithm under the UIC of Figure 5.1 for 500 simulations. Standard deviations valued at zero mean high deterministic behavior.

Metric	**Voltage**	**Power**	**Number of iterations**
Mean (μ)	188.18	1488.78	16
Standard Deviation (σ)	0.000	0.000	0.000
Efficiency		99.04%	

Source: The author.

Table 5.11 – The performance of the RMO algorithm under the PSC of Figure 5.2 for 500 simulations. Standard deviations valued at zero mean high deterministic behavior.

Metric	**Voltage**	**Power**	**Number of iterations**
Mean (μ)	125.45	972.51	16
Standard Deviation (σ)	0.000	0.000	0.000
Efficiency		98.17%	

Source: The author.

Table 5.12 – The performance of the RMO algorithm under the PSC of Figure 5.3 for 500 simulations. Low standard deviations mean high accuracies.

Metric	**Voltage**	**Power**	**Number of iterations**
Mean (μ)	126.35	649.18	16
Standard Deviation (σ)	1.389	1.538	0.000
Efficiency		99.56%	

Source: The author.

Table 5.13 – The performance of the RMO algorithm under the PSC of Figure 5.4 for 500 simulations.

Metric	**Voltage**	**Power**	**Number of iterations**
Mean (μ)	200.04	431.74	16.01
Standard Deviation (σ)	2.228	2.685	0.205
Efficiency		98.18%	

Source: The author.

Table 5.14 – The performance of the RMO algorithm under the PSC of Figure 5.5 for 500 simulations. Standard deviations valued at zero mean high deterministic behavior.

Metric	**Voltage**	**Power**	**Number of iterations**
Mean (μ)	62.73	446.59	16
Standard Deviation (σ)	0.000	0.000	0.000
Efficiency		93.43%	

Source: The author.

From Table 5.13, the low standard deviation in the voltage means that the algorithm stuck at the local MPP of 200 V (433 W), probably never reaching the global MPP at 59.3 V (439.74 W).

From the charts, the original RMO algorithm presents slightly faster convergence when compared to the modified version proposed in this work. This, however, implies a loss in accuracy of the MPP obtained and, for some scenarios, the inability of the algorithm in finding the GMPP which directly impact the overall efficiency. Continuing with the comparisons, the next charts will present the performances of the PSO algorithm.

Table 5.15 – The performance of the PSO algorithm under the UIC of Figure 5.1 for 500 simulations. Low standard deviations mean high accuracies.

Metric	**Voltage**	**Power**	**Number of iterations**
Mean (μ)	181.16	1503.08	37.23
Standard Deviation (σ)	0.180	0.000	4.511
Efficiency		99.99%	

Source: The author.

Table 5.16 – The performance of the PSO algorithm under the PSC of Figure 5.2 for 500 simulations. Low standard deviations mean high accuracies.

Metric	**Voltage**	**Power**	**Number of iterations**
Mean (μ)	119.18	990.53	36.62
Standard Deviation (σ)	0.182	0.000	4.340
Efficiency		99.99%	

Source: The author.

Table 5.17 – The performance of the PSO algorithm under the PSC of Figure 5.3 for 500 simulations. Low standard deviations mean high accuracies.

Metric	**Voltage**	**Power**	**Number of iterations**
Mean (μ)	127.12	652.02	39.17
Standard Deviation (σ)	0.144	0.050	5.448
Efficiency		100%	

Source: The author.

Table 5.18 – The performance of the PSO algorithm under the PSC of Figure 5.4 for 500 simulations.

Metric	**Voltage**	**Power**	**Number of iterations**
Mean (μ)	74.41	438.46	37.25
Standard Deviation (σ)	44.567	3.427	7.686
Efficiency		99.70%	

Source: The author.

Table 5.19 – The performance of the PSO algorithm under the PSC of Figure 5.5 for 500 simulations. Low standard deviations mean high accuracies.

Metric	**Voltage**	**Power**	**Number of iterations**
Mean (μ)	57.22	477.94	35.60
Standard Deviation (σ)	0.195	0.000	4.232
Efficiency		99.99%	

Source: The author.

From Table 5.18, the high standard deviation in the voltage means that the algorithm may have reached the local MPPs at 162 V (413 W) or 200 V (433 W) for a number of times, but the mean voltage of 74.41 V indicates that the dominant result from the execution of the algorithm is around the GMPP, that is, 59.3 V (439.74 W).

PSO presents higher efficiencies when compared to both RMO and the modified version, mRMO, but to the detriment of speed of convergence. It takes more than twice the number of iterations needed to reach the GMPP when compared to the other algorithms, with higher standard deviation, which means an increase in uncertainty of the tracking velocity. To finish this comparison, the performances of the DE algorithm are shown in the following tables.

Table 5.20 – The performance of the DE algorithm under the UIC of Figure 5.1 for 500 simulations. Low standard deviations mean high accuracies.

Metric	**Voltage**	**Power**	**Number of iterations**
Mean (μ)	181.31	1503.08	84.61
Standard Deviation (σ)	0.284	0.000	25.047
Efficiency		99.99%	

Source: The author.

Table 5.21 – The performance of the DE algorithm under the PSC of Figure 5.2 for 500 simulations. Low standard deviations mean high accuracies.

Metric	**Voltage**	**Power**	**Number of iterations**
Mean (μ)	119.48	990.53	35.67
Standard Deviation (σ)	0.340	0.062	26.410
Efficiency		99.99%	

Source: The author.

Table 5.22 – The performance of the DE algorithm under the PSC of Figure 5.3 for 500 simulations. Low standard deviations mean high accuracies.

Metric	**Voltage**	**Power**	**Number of iterations**
Mean (μ)	127.44	652.01	37.42
Standard Deviation (σ)	0.329	0.135	28.888
Efficiency		99.99%	

Source: The author.

Table 5.23 – The performance of the DE algorithm under the PSC of Figure 5.4 for 500 simulations.

Metric	**Voltage**	**Power**	**Iterations**
Mean (μ)	62.53	439.16	20.39
Standard Deviation (σ)	23.362	1.154	8.564
Efficiency		99.86%	

Source: The author.

Table 5.24 – The performance of the DE algorithm under the PSC of Figure 5.5 for 500 simulations. Low standard deviations mean high accuracies.

Metric	**Voltage**	**Power**	**Iterations**
Mean (μ)	57.51	477.87	26.97
Standard Deviation (σ)	0.398	0.663	18.234
Efficiency		99.97%	

Source: The author.

Table 5.23 indicates a high standard deviation in the voltage, which means that the algorithm may have reached the local MPPs at 162 V (413 W) or 200 V (433 W) for a number of times, but the mean voltage of 62.53 V indicates that the dominant result from the execution of the algorithm is around the GMPP (59.3 V; 439.74 W).

From the last five charts, the DE algorithm reveals high accuracies with relative slower convergence to the GMPP. It is generally faster than PSO and slower than the radial movement algorithms. The main drawback of this technique is its high standard deviation in the number of iterations needed to reach the maxima, which indicates considerable uncertainty in the tracking velocity. Therefore, the modified RMO proposed in this research work seems to better conform to the requirements of a suitable MPPT as exposed in subsection 2.3.2, simultaneously exhibiting high accuracy, fast operation and simple implementation.

While the offline test approach validates the performance of the algorithms under many pre-determined scenarios, the online approach will expose the MPPTs to real operating conditions where the algorithms must continuously track the GMPP under the influence of the attached buck-boost converter.

5.3 Online Approach

For the online test procedure, the whole system including the power converter, the PV array and the load must be developed in the simulation environment of Simulink®. Figure 5.18 depicts these components.

Figure 5.18 – The PV system comprising an array, a buck-boost DC/DC converter and a resistive load.

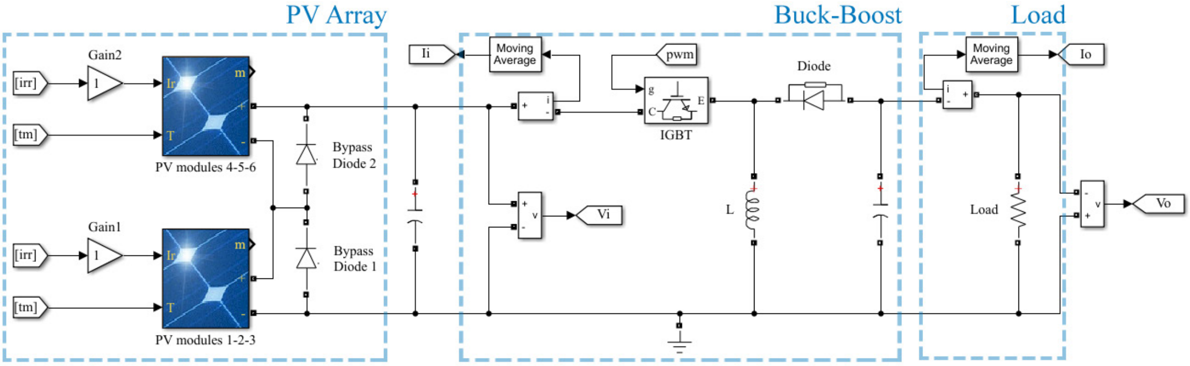

Source: The author.

The PV array emulates the one available at LEA/UFC with additional bypass diodes. Two diodes were inserted protecting each group of 3 modules. Ideally, six bypass diodes would be used but this represents additional cost and is, thus, a practice that is avoided in commercially available solutions.

The load is a resistance valued at 18 ohms which nearly matches the maximum power point of the PV source at 1000 W/m² of input irradiance and cell temperatures of 25 ºC. This means that if the PV array was directly attached to the load, it would operate almost on the MPP. This impedance matching represents an old technique employed before the advent of MPPT strategies (MESSENGER *et al.*, 2010).

The buck-boost converter parameters are detailed in Table 5.25.

Table 5.25 – Buck-boost parameters.

Parameter	**Value**
Inductance	4 mH
Output Capacitance	20 μF
Diode Forward Voltage	0.8 V
IGBT Switching Frequency	30 kHz
IGBT Forward Voltage	0.05 V

Source: The author.

The MPPT techniques evaluated in this online approach was implemented with the *S-Function* module in Simulink® with basically the voltage and current of the PV array as the inputs, and the duty cycle as the output of the MPP trackers. Figure 5.19 illustrates the MPPT integrated in the circuit of Figure 5.18.

Figure 5.19 – The PV system with an MPPT driving a PWM generator.

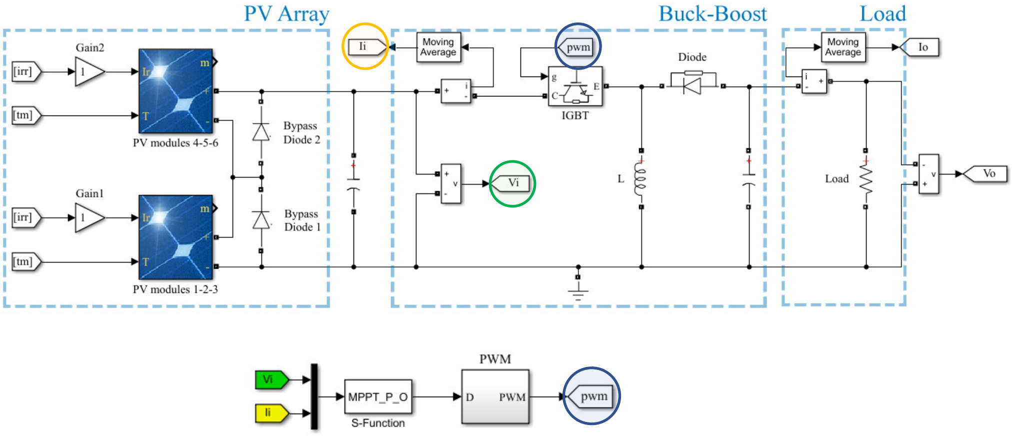

Source: The author.

The real data regarding input irradiance and cell temperature, collected from the PV string available at LEA/UFC on March 12th, 2018 is depicted in Figure 5.20.

Figure 5.20 – Real input data collected on 12th Mar, 2018. (a) Irradiance in W/m² and (b) cell temperature in Celsius degrees.

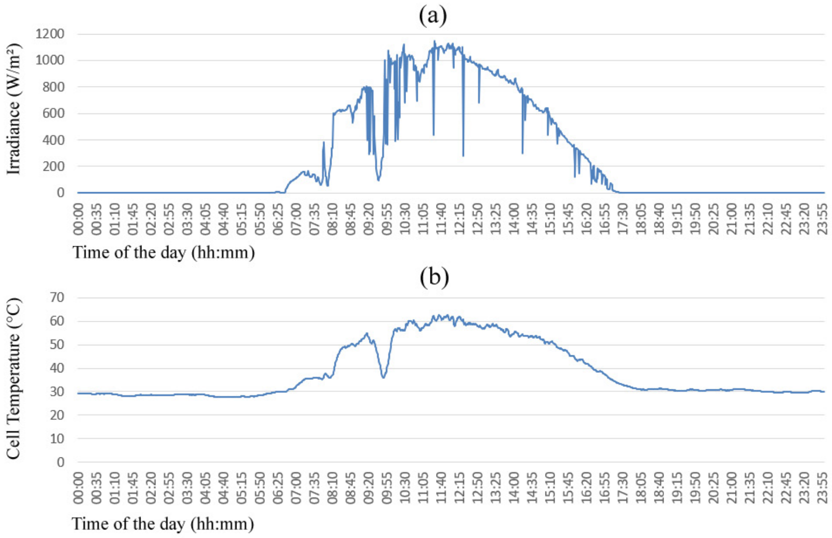

Source: The author.

The data can be stored in memory and provided to the inputs of the PV array as in Figure 5.18. In the same figure, it is seen that gains are added to the irradiance input of the modules. The idea is to simulate PSC by changing the gain values for each group of modules.

Another consideration for the online test procedure is related to the settling time of the PV array voltage and/or current after a modification is imposed by the MPP tracking algorithm. Depending on the step value and the instantaneous voltage sensed from the array, large overshoots and undershoots are experienced in the transient response. It is not reasonable to sense the power from the array at these moments, thus a waiting period should be set.

An empirical method can be adopted to adjust a fixed settling time that is sufficiently large to cover both the fastest and the slowest transient responses, although it is obviously not an optimal solution. To determine the right moment for sensing the power from the array, the variance of the voltage can be used in a way that when below a certain threshold value, the power can be safely sampled, and the algorithm can move on with the tracking procedure. Empirical analysis must be used to determine the threshold value which in this work was set to 0.35.

With these considerations, a set of test scenarios will be evaluated as follows.

5.3.1 First Scenario

In this scenario, uniform irradiance condition is imposed to the PV string, and a single point in the curves of Figure 5.20 representing fixed irradiance and cell temperature is considered. The idea is to check the performance of the proposed algorithm under a trivial case.

Table 5.26 – Configuration of the first scenario.

Parameter	**Value**
Irradiance	1089 W/m²
Cell Temperature	60.71 °C
Maximum Power	1373.9 W
Voltage at Maximum Power	153.7 V

Source: The author.

Figure 5.21 – The observation point of the first scenario in the curves of irradiance and temperature of Figure 5.20.

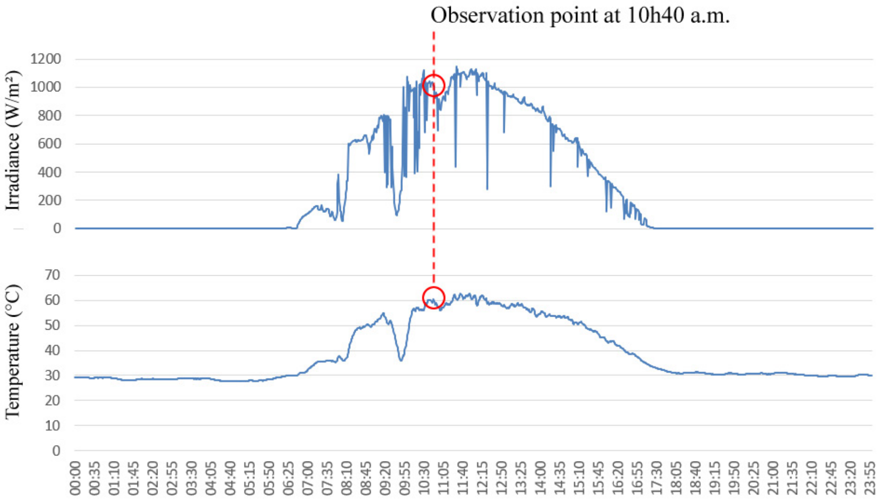

Source: The author.

Table 5.27 – Performance of the classical P&O on the first scenario.

Parameter	**Value**
Maximum Power	1360 – 1380 W
Voltage at Maximum Power	156 – 161 V
Tracking time	0.1 s

Source: The author.

Table 5.28 – Performance of the mRMO algorithm on the first scenario.

Parameter	**Value**
Maximum Power	1371.2 W
Voltage at Maximum Power	149.2 V
Tracking time	0.91 s

Source: The author.

With this UIC scenario, both algorithms were able to locate the MPP with relevant accuracy. P&O performs about 9 times faster than mRMO, but presents oscillations of 20 W in the output power, representing an average efficiency of 99.7% (considering an average power of 1370 W). The modified RMO offers a steady operation after locating the MPP with an efficiency of 99.8%.

5.3.2 Second Scenario

In this scenario, the same point in the curves of Figure 5.21 is considered, but forcing a partial shading condition by setting the input gain of the modules 1-3 to 0.5 (refer to Figure 5.18 to identify the modules 1-3). This non-uniformity of the irradiance hitting the string causes the P-V curve to exhibit two maximum points. The proposed MPPT is expected to track the global maximum without much problem.

Table 5.29 – Configuration of the second scenario.

Parameter	**Value**
Irradiance	1089 W/m²
Cell Temperature	60.71 °C
Global Maximum Power	779.33 W
Voltage at Maximum Power	167 V

Source: The author.

Figure 5.22 – The observation point of the second scenario and an illustration of the partial shading affecting the PV string.

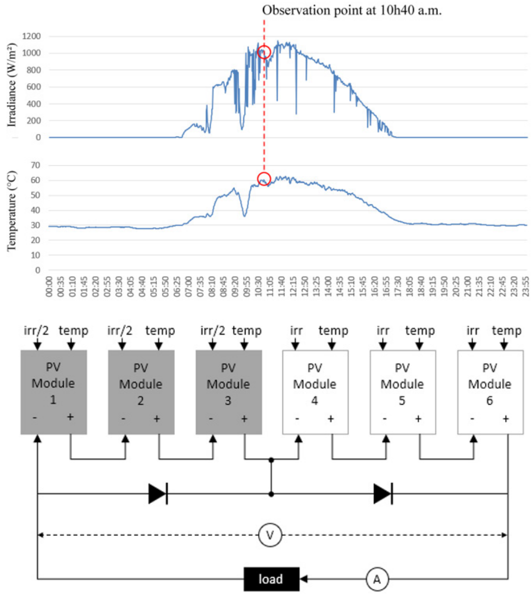

Source: The author.

Table 5.30 – Performance of the classical P&O on the second scenario.

Parameter	Value
Maximum Power	640 – 690 W
Voltage at Maximum Power	77 – 84 V
Tracking time	0.15 s

Source: The author.

Table 5.31 – Performance of the mRMO algorithm on the second scenario.

Parameter	Value
Maximum Power	770.68 W
Voltage at Maximum Power	161.7 V
Tracking time	1.2 s

Source: The author.

In this PSC scenario, P&O did not manage to locate the GMPP, instead, it oscillated around a local maximum at 665 W, representing an efficiency of 85.3%. The modified RMO, although 8 times slower than P&O, was able to locate the GMPP with an efficiency of 98.9%.

5.3.3 Third Scenario

A slice of time is taken from the curves of Figure 5.20 with a severe change in the input irradiance. The idea is to analyze the performance of the algorithms in tracking the MPP over a period of time. The slice of time considered is illustrated in Figure 5.23.

Figure 5.23 – Slice of time in the irradiance curve showing the two operating points. The MPP in #1 is 1372.5 W (152.8 V), and 558.62 W (155.5 V) for the point #2.

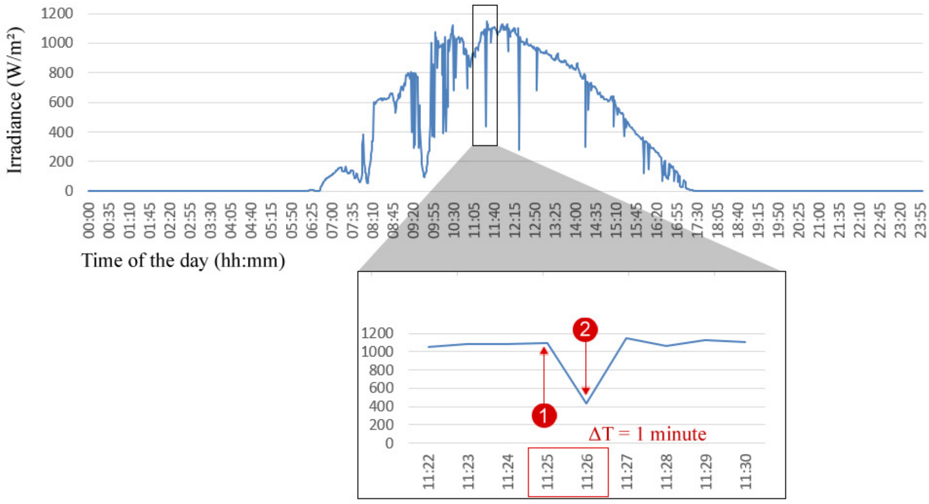

Source: The author.

It is expected that the algorithms, firstly operating at the point #1, set the MPP as close as possible to 1372.5 W (152.8 V) and then, when the input irradiance drastically drops to around 400 W/m² at the operating point #2, the MPPTs manage to set the maximum power point at 558.62 W (155.5 V). Figures 5.24 and 5.25 respectively depict the performances of the P&O and the modified RMO on this scenario.

Figure 5.24 – Performance of the classical P&O on the third scenario.

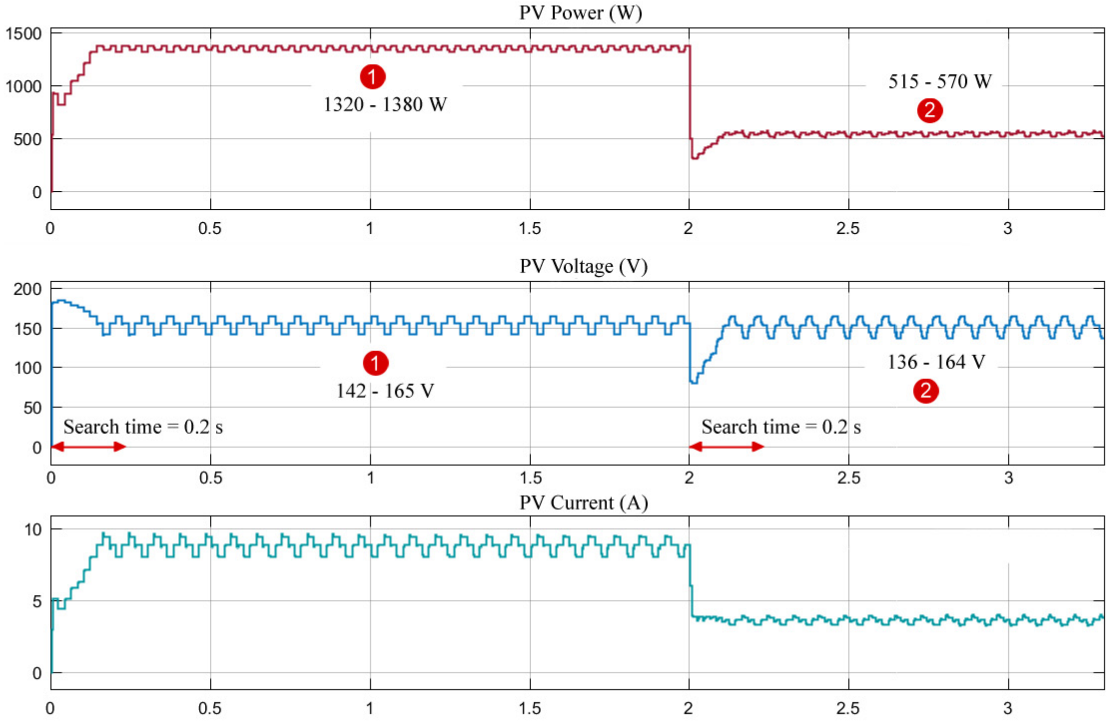

Source: The author.

At the operating point #1, P&O sets the PV system to oscillate in a range of 60 W around an average power point of 1350 W, representing an efficiency of 98.3%. The voltage curve at the bottom shows an oscillation range of about 20 V for the operating point #1, and 30 V for #2. Since the input irradiance intensively reduced, which reflected a drop in power as observed from the graphs, the output current of the PV system is responsible for the large drop, once the voltage remained practically the same.

Figure 5.25 – Performance of the proposed mRMO on the third scenario.

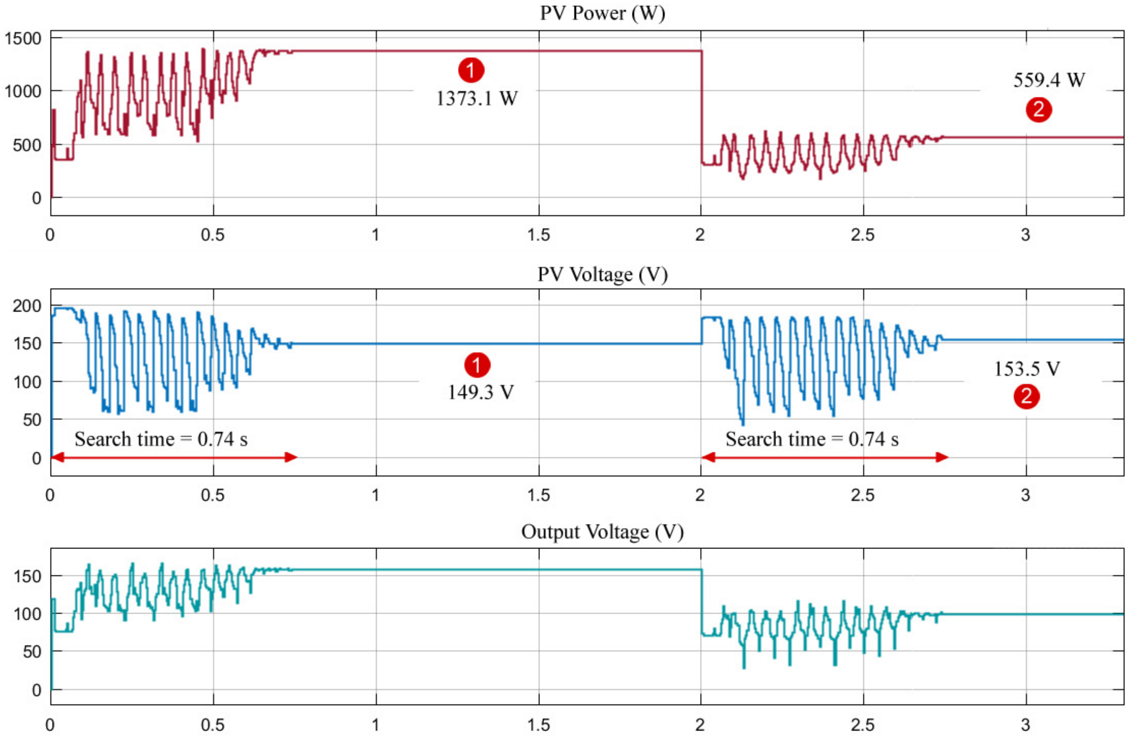

Source: The author.

As observed in Figure 5.25, mRMO is four times slower than the classical P&O for this scenario, but provides steady outputs after locating the MPP. At the point #1, its efficiency reaches 99.9%, while at the second point it is 99.8%.

5.3.4 Fourth Scenario

In this scenario, a slice of time of 140 minutes is taken from the curves of Figure 5.20 as depicted in Figure 5.26. The idea is to analyze the performance of both techniques, P&O and mRMO, in capturing and converting solar energy as much as possible during a greater period of time, simulating the actual operation of these systems.

The scenario is divided into two strategies: a) The PV array is composed of two bypass diodes; b) A third bypass diode is inserted. Figure 5.27 depicts these compositions.

Figure 5.26 – Slice of the irradiance and temperature curves used in the fourth scenario. Energy would be accumulated and compared along 140 minutes. Partial shading is simulated to occur stochastically.

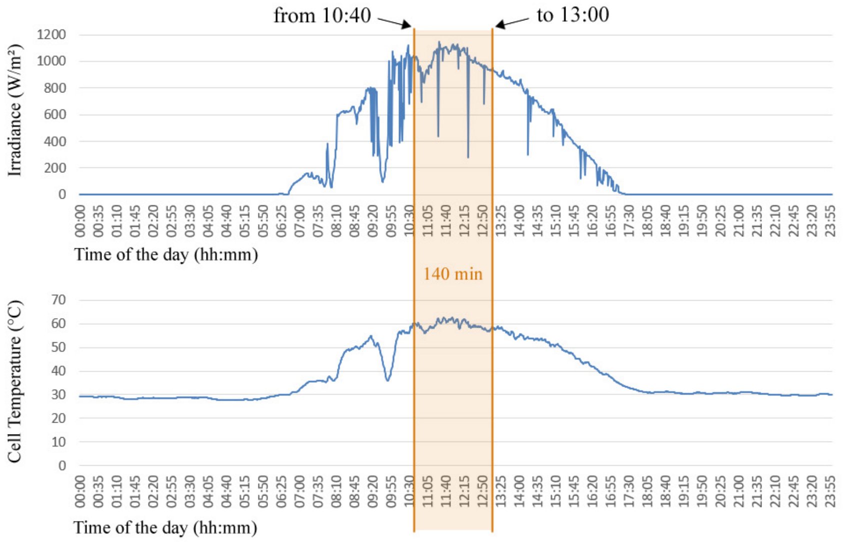

Source: The author.

Figure 5.27 – The PV string composed of (a) two and (b) three bypass diodes.

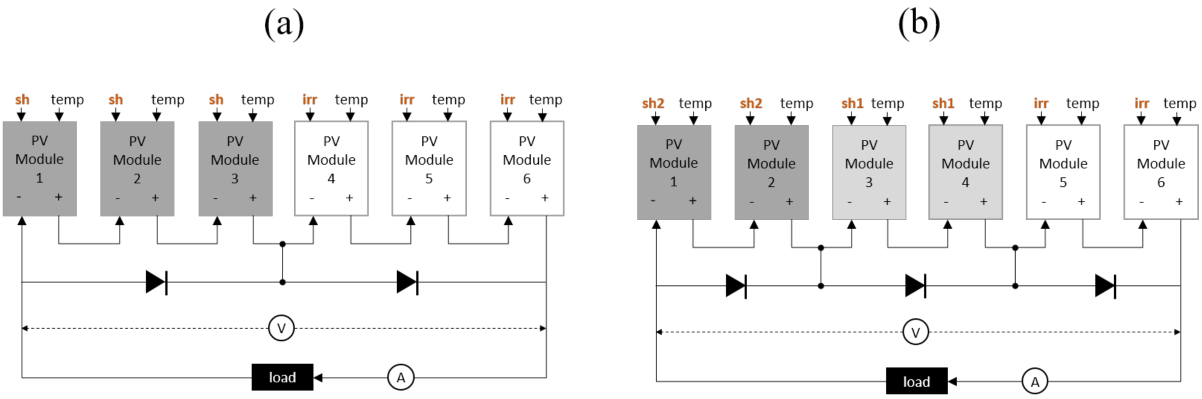

Source: The author.

Figure 5.28 – Random shading occurring at modules 1-3 (bottom) simulating a PSC at the PV system with 2 bypass diodes. Modules 4-6 perceive the full irradiance (top).

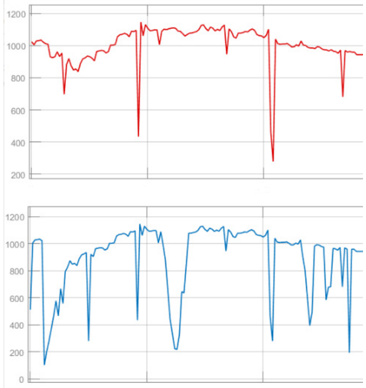

Source: The author.

Figure 5.29 – Different random shading occurring at modules 1 and 2 (bottom), and 3 and 4 (center) simulating a PSC at the PV system with 3 bypass diodes. Modules 5 and 6 perceive the full irradiance (top).

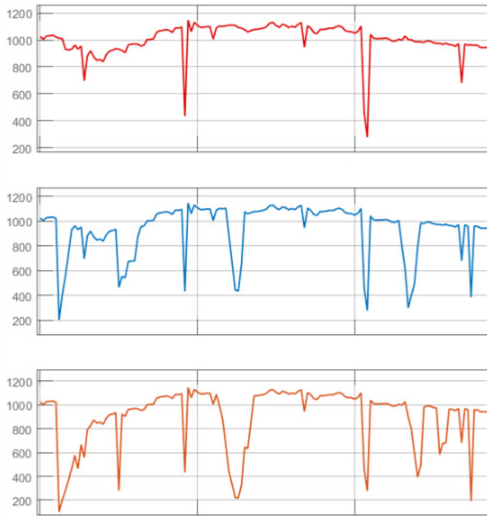

Source: The author.

5.3.4.1 *Strategy A: 2 bypass diodes*

Considering Figure 5.27a, the PV string has been stimulated with the irradiance curves shown in Figure 5.28, which means that at particular random periods, the irradiance hitting modules 1-3 is not the same as the one perceived by the other modules, which defines a partial shading condition. We thereby have to run both algorithms and perform a comparison between them in order to check which one converted the most part of the solar energy after the whole period of 140 minutes[14]. Figures 5.30 and 5.31 bring the output curves of both MPPTs.

Figure 5.30 – Power curves captured between the 15th and 40th minutes for both algorithms.

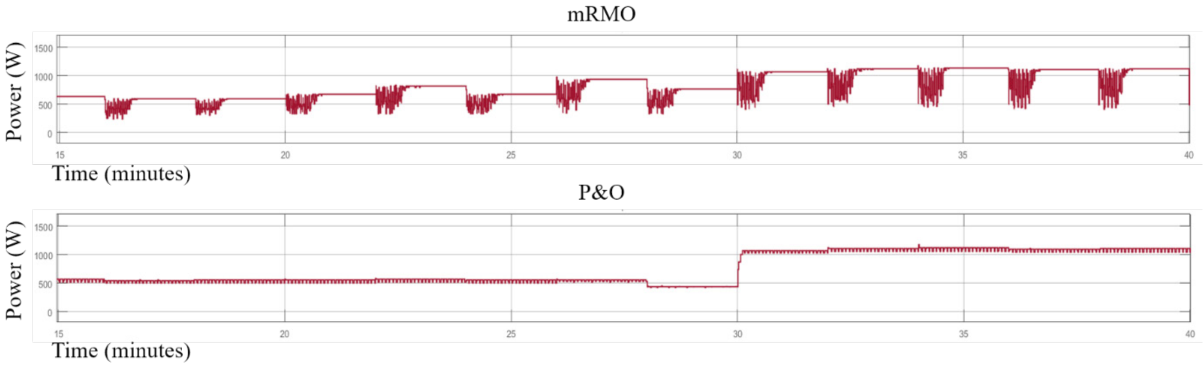
mRMO

P&O

Source: The author.

---

[14] It is important to mention that the timescale in the curves of Figures 5.30 to 5.34, as well as in Figure 5.25 are somewhat distorted. To increase the speed of the simulations, the change in irradiance was anticipated to occur every two seconds instead of every minute of real time. From the curves, it looks like mRMO takes about 30 seconds to find the GMPP which is not true. It really takes less than a second, but the change in irradiance occurs one second after so we do not need to wait for a whole minute of simulation time.

Figure 5.31 – Power curves captured from minute 57 to 70 for both algorithms.

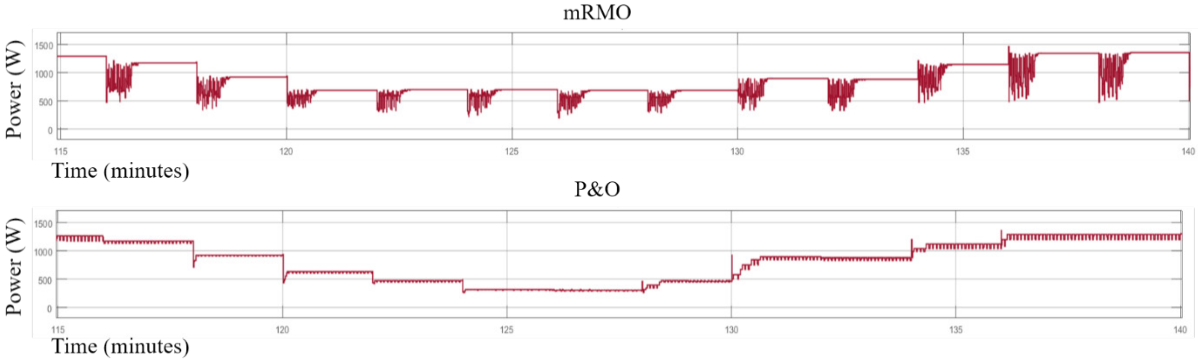

Source: The author.

It is visually noticeable from the figures that at particular moments, mRMO could achieve better results in terms of produced power. This can be ensured by the information on Table 5.32:

Table 5.32 – The amount of energy produced by both algorithms in the case of the 4th scenario, considering two bypass diodes in the PV string. The percentage is relative to P&O's result.

MPPT	**Produced Energy**	
	kWh	**%**
mRMO	1205	+ 4.78
P&O	1150	--

Source: The author.

5.3.4.2 Strategy B: 3 bypass diodes

Now considering the circuit diagram depicted in Figure 5.27b, the PV string has been stimulated with the irradiance curves shown in Figure 5.29, which means that at particular random periods, the irradiance hitting modules 1-2 or 3-4 is not the same as the one perceived by the other modules, which defines a more complex partial shading condition. We thereby have to run both algorithms and perform a comparison between them in order to check which one captured and converted the most part of the solar energy after the whole period of 140 minutes. Figures 5.32 to 5.34 bring the output curves of both MPPT algorithms. Table 5.33 summarizes the information about the amount of energy produced by them in this particular situation.

Figure 5.32 – Power curves captured for the first 7 minutes for both algorithms.

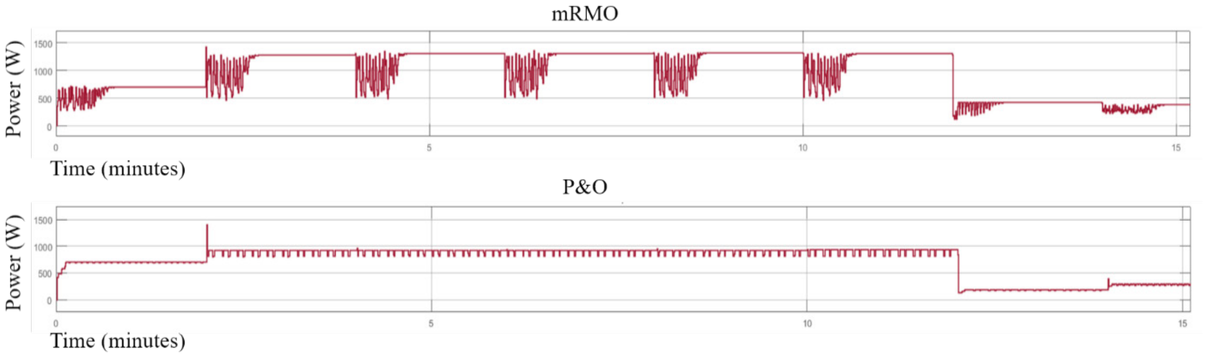

Source: The author.

Figure 5.33 – Power curves captured between the minutes 40 and 55 for both algorithms.

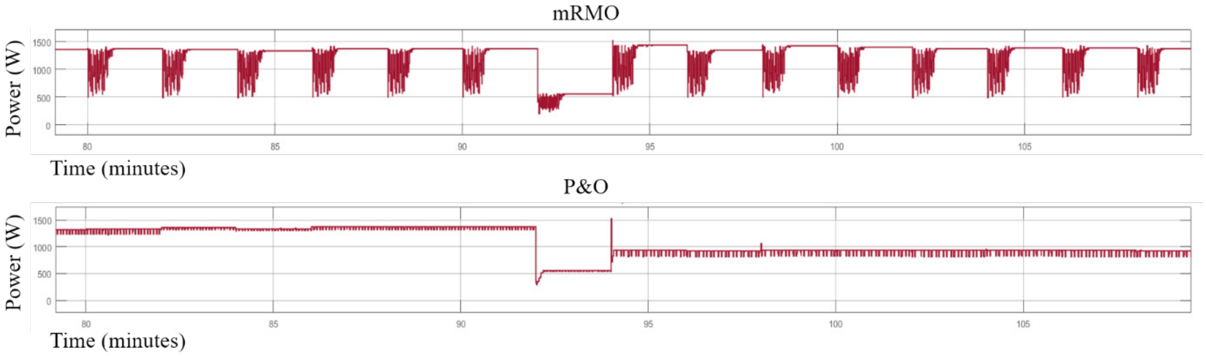

Source: The author.

Figure 5.34 – Power curves captured between the minutes 125 and 140 for both algorithms.

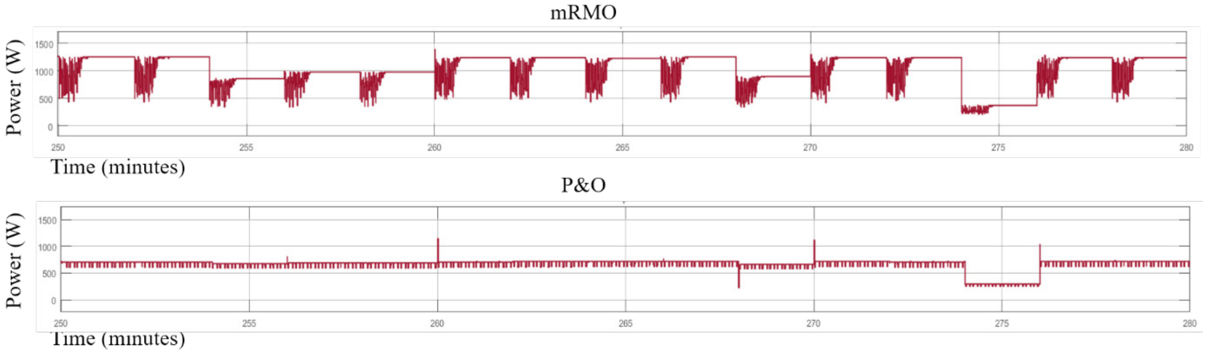

Source: The author.

In this scenario, it is visually noticeable that mRMO performs better in not rare moments. With three bypass diodes, the P-V curves show multiple maxima with distant power values from each other. It is more evident the advantage of the proposed algorithm over the conventional P&O. Table 5.33 summarizes this information.

Table 5.33 – The amount of energy produced by both algorithms in the case of the 4th scenario, with three bypass diodes in the PV string. The percentage is relative to P&O's result.

MPPT	**Produced Energy**	
	kWh	**%**
mRMO	1178	+ 44.36
P&O	816	--

Source: The author.

It is clearly seen from the charts and figures that the modified RMO provides accurate tracking with slower speed, whereas the classical P&O shows fast convergence with oscillating outputs. In not rare situations, P&O converges to a local MPP instead of the GMPP, as exposed in Table 5.30 and in various moments shown in Figures 5.30 to 5.34. This makes it clear that when dealing with non-uniform irradiance conditions, techniques based on the hill climbing method are not enough for delivering the most out of the energy conversion system.

5.4 Summary of the results

The following tables present a summary of the results obtained along this section:

5.4.1 Offline approach

Table 5.34 – Summary of the results for the offline test approach.

MPPT technique	**Comments**
P&O	Fast to find the MPP, depending on the step size. Always presented oscillations around the MPP. Under PSC, finding the GMPP depended on the starting point of the control variable (which in real operation is not configurable).
IncCond	Same speed as P&O to find the MPP, also depending on the step size. Oscillations around the MPP occurred in some situations (2 out of 6). As with P&O, under PSC, finding the GMPP depended on the starting point of the control variable (which in real operation is not configurable).
mRMO	Took an average of 17 iterations, with very low variance, to find the MPP with no oscillations after reaching it. GMPP has always been found with very high efficiency.
RMO	Took an average of 16 iterations, with almost no variance, to find the MPP with no oscillations after reaching it. GMPP has always been found, but with considerably less efficiency when compared to mRMO.
PSO	Took an average of 37 iterations, with small variance, to find the MPP with no oscillations after reaching it. GMPP has not always been found, but when found, the efficiency was the highest.
DE	Took an average of 40 iterations, with significant variance, to find the MPP with no oscillations after reaching it. GMPP has not always been found, but when found, the efficiency was slightly higher than mRMO but lower than PSO.

Source: The author.

5.4.2 Online approach

Table 5.35 – Summary of the results for the online test approach.

MPPT technique	**Comments**
P&O	In the first scenario was able to track the MPP very fast. Presented oscillations of 20 W in the output power. During the second scenario, was not able to find the GMPP, drifting around a local maximum of 665 W. In the third scenario, found the MPPs within 0.2 seconds, but with oscillations of 60 W around them. Finally, in the fourth scenario, fell on local maxima a number of times within the 140 minutes observed, which decreased the amount of energy produced.
mRMO	In the first scenario was able to track the MPP 9 times slower than P&O. Presented no oscillations in the output power. During the second scenario, was able to find the GMPP, rather than a local maximum, around 1 second. In the third scenario, found the MPPs only 4 times slower than P&O, but with no oscillations around them. Finally, in the fourth scenario, never reached a local maximum within the 140 minutes observed (always found the GMPPs), which increased the amount of energy produced by 5-44% when compared to the classical P&O.

Source: The author.

6 CONCLUDING NOTES

6.1 General and Specific Contributions

This research work proposed the implementation and validation of an MPPT for photovoltaic systems based on a recent computational intelligence technique that could be simultaneously accurate and relatively fast, while being robust to partial shading phenomena. The literature is overgrown on the subject but some of the proposals do not represent economically viable solutions or are hard to deploy on existing PV plants. It was expected that the solution proposed in this work could overcome these limitations by not requiring excessive auxiliary subsystems, such as expensive pyranometers to help predicting P-V curves under partial shading situations, nor demanding array rearrangement which would render infeasible.

Accuracy and velocity of the solution is demonstrated by extensive offline test runs with different degrees of difficulty in the simulated non-uniform irradiance scenarios. The proposed MPPT was able to distinguish and detect the global maximum power point in challenging conditions with high efficiency and within few iterations. This represents an advantage over the classical and intelligent techniques available in the literature, which ensures the contributions of the proposed solution.

Real operation was possible to be investigated through online test procedures which revealed remarkable performance of the proposed solution against the classical P&O method when subjected to real irradiance and temperature conditions, under the influence of the employed power converter. With slightly greater time demand, the intelligent MPPT is able to find the GMPP while P&O shows an impractical dependency to reach this operating point. In addition, P&O presents an unavoidable oscillation in the produced power when reaching the MPP (occasionally the GMPP) due to the nature of its operation. As it continuously imposes a change in the control variable, there is no stop condition for the algorithm. mRMO, in contrast, takes less than one second during the search for the GMPP and has a stop condition, which makes the produced power not to present oscillations once at the GMPP, and remains steady as long as the next search procedure does not happen.

There is one drawback with the intelligent tracker: due to its nature, during the search procedure (and only there), the algorithm imposes severe changes in the control variable that result in higher power oscillations. Although smoother transients can be achieved by adjusting the algorithm, such adjustment will negatively impact the efficiency of the technique in finding the GMPP when partial shading occurs.

Dependence on system-specific parameters was reduced by operating on the duty cycle of the power converter instead of on the voltage of the PV array. The range of operation varies for each system when the voltage is the control variable. The duty cycle, on the other hand, has a pre-determined range of operation. This allows the proposed MPPT to be ported to different PV systems with minimal adaptation required.

Having explored the subject, from the basic concepts to the application in a real problem, represented a step forward in the scientific knowledge and improved expertise in the domain of such a promising renewable energy source like the solar photovoltaic energy. This document is also expected to serve as the fundamental guide to further researches as it systematically presents the concepts over a wide range of knowledge fields, and also discusses the limitations of the techniques employed, leaving considerable room for improvements. Some of these improvements are listed as follows.

6.2 Guidance for Improvements

As a first suggestion, the implementation of the proposed solution into a low-cost microcontroller would be an important improvement concerning the validation of the technique in a real device, allowing hardware-software co-simulation to be used for the online test procedures. The interested researcher could further develop the whole system, that is, the MPPT along with the DC/DC power converter, and apply the complete hardware solution in a real PV plant, extending the software validation approaches.

The proposed algorithm is also suitable for implementation into FPGA devices since the parallel nature of these chips would result in greater performance and diminished time required to track the global maximum points. Extra logic could be added to the design, incorporating, for example, the PWM signal generator from the duty cycle information available at the output of the MPPT module.

Another relevant contribution to extend the scope of the present research would be the adoption of a voltage controller interfacing the MPPT and the power converter. That would allow an increase in the tracking speed since transient responses on the voltage of the PV array could be significantly reduced. This, however, would impose the control variable to be the voltage of the PV array instead of the duty cycle of the converter, leading the solution to a more system-dependent one.

Concerning partial shading phenomena, artificial intelligence techniques could be employed to help mitigating the effects of such impairment. For instance, prediction of the P-V curves for a given input irradiance and temperature condition would accelerate the tracking speed since there would be no need to wait for the PV array settlement to proceed with the tracking procedure. It is evident that under partial shading conditions, the input irradiance information should be available for every PV module in the array, or at least for the number of bypass diodes that are present. The use of low-cost illumination sensors as opposed to the high-cost pyranometers would help in reducing the cost of this solution to the detriment of the accuracy in the prediction. Intelligent tools such as Fuzzy Logic are known to better dealing with uncertain information. The investigation of such approach applied into this problem would be a relevant scientific contribution.

Lastly, the voltage controller previously mentioned could be substituted by a neural controller, i.e., a controller based on purely neural or hybrid neuro-fuzzy networks. Such controller could be incorporated in the complete solution embedded into an FPGA device.

REFERENCES

ABSOLAR. Associação Brasileira de Energia Solar Fotovoltaica. **Brasil deve alcançar a marca de 2 GW em energia solar instalada em 2018**. 2018. Available at: <http://www.absolar.org.br/noticia/noticias-externas/brasil-deve-alcancar-a-marca-de-2-gw-em-energia-solar-instalada-em-2018.html>. Accessed on: 16 May 2018.

AL NABULSI, A.; DHAOUADI, R. Efficiency Optimization of a DSP-Based Standalone PV System using Fuzzy Logic and Dual-MPPT Control. **IEEE Trans. Ind. Informatics**, vol. 8, n. 3, p. 1–12, 2012.

ALONSO-GARCÍA, M. C.; RUIZ, J. M.; CHENLO, F. Experimental study of mismatch and shading effects in the I-V characteristic of a photovoltaic module, **Solar Energy Materials & Solar Cells**, v. 90, n. 3, p. 329–340, 2006.

BARAGIOLA, R. **Electronic Structure of Surfaces**. University of Virginia. 2002a. Available at: <http://www.virginia.edu/ep/SurfaceScience/electron.html>. Accessed on: 21 May 2018.

BARAGIOLA, R. **Photoelectric Emission**. University of Virginia. 2002b. Available at: <http://www.virginia.edu/ep/SurfaceScience/PEE.html>. Accessed on: 21 May 2018.

BELHACHAT, F.; LARBES, C. Global maximum power point tracking based on ANFIS approach for PV array configurations under partial shading conditions. **Renewable and Sustainable Energy Reviews**, v. 77 (2017), p. 875–889, 2017.

BELHAOUAS, N.; AIT CHEIKH, M.-S.; AGATHOKLIS, P.; OULARBI, M.-R.; AMROUCHE, B.; SEDRAOUI, K.; DJILALI, N. PV array power output maximization under partial shading using new shifted PV array arrangements, **Applied Energy**, v. 187, p. 326–337, 2017.

BIANCHI, L.; DORIGO, M.; GAMBARDELLA, L. M.; GUTJAHR, W. J. A survey on metaheuristics for stochastic combinatorial optimization, **Natural Computing: an international journal**, v. 8, n. 2, p. 239–287, 2009. DOI:10.1007/s11047-008-9098-4.

BRADAI, R.; BOUKENOUI, R.; KHELDOUN, A.; SALHI, H.; GHANES, M.; BARBOT, J-P.; MELLIT, A. Experimental assessment of new fast MPPT algorithm for PV systems under non-uniform irradiance conditions. **Applied Energy**, v. 199, p. 416–429, 2017.

BULOVIC, V.; LUNT, R. R. **Transparent Photovoltaic Cells**. U.S. Patent, US 20180019421 A1, issued January 18, 2018. Available at: <https://patentimages.storage.googleapis.com/11/aa/98/3900fb44307b0a/US20180019421A1.pdf>. Accessed on: 24 May 2018.

ÇELIK, Ö.; TEKE, A. A Hybrid MPPT method for grid connected photovoltaic systems under rapidly changing atmospheric conditions. **Electric Power Systems Research**, v. 152, p. 194–210, 2017.

CHAIEB, H.; SAKLY, A. A novel MPPT method for photovoltaic application under partial shaded conditions. **Solar Energy**, v. 159, p. 291–299, 2018.

CHEKIRED, F.; MELLIT, A.; KALOGIROU, S. A.; LARBES, C. Intelligent maximum power point trackers for photovoltaic applications using FPGA chip: a comparative study. **Solar Energy**, v. 101, p. 83–99, 2014.

CHOWDHURY, S. R.; SAHA, H. Maximum power point tracking of partially shaded solar photovoltaic arrays, **Solar Energy Materials & Solar Cells**, v. 94, p. 1441–1447, 2010.

COELHO, R. F.; CONCER, F. M.; MARTINS, D. C. A study of the basic DC-DC converters applied in maximum power point tracking. **2009 Power Electronics Conference** (COBEP'09), p. 673–678, 2009.

COELHO, R. F.; CONCER, F. M.; MARTINS, D. C. Analytical and experimental analysis of DC-DC converters in photovoltaic maximum Power Point Tracking applications. **36th IEEE Industrial Electronics Society Annual Conference** (IECON'2010), p. 2778–2783, 2010.

DI PIAZZA, M. C.; VITALE, G. **Photovoltaic Sources:** Modeling and Emulation. Springer-Verlag. London, 2013. https://doi.org/10.1007/978-1-4471-4378-9_1.

EIA. U.S. Energy Information and Administration. **Photovoltaics and Electricity.** 2017b. Available at: <https://www.eia.gov/energyexplained/index.php?page=solar_photovoltaics>. Accessed on: 15 May 2018.

EIA. U.S. Energy Information and Administration. **What is renewable energy?** 2017a. Available at: <https://www.eia.gov/energyexplained/index.php?page=renewable_home>. Accessed on: 13 May 2018.

ELGENDY, M. A.; ZAHAWI, B.; ATKINSON, D. J. Evaluation of perturb and observe MPPT algorithm implementation techniques. **6th IET International Conference on Power Electronics, Machines and Drives** (PEMD 2012), p. 110-116, 2012. DOI: 10.1049/cp.2012.0156.

ENGELBRECHT, A. P. **Computational Intelligence: an introduction,** 2nd ed., John Wiley & Sons Ltd., 2007.

ENRIQUE, J. M.; DURÁN, E.; SIDRACH-DE-CARDONA, M.; ANDÚJAR, J. M. Theoretical assessment of the maximum power point tracking efficiency of photovoltaic facilities with different converter topologies. **Solar Energy**, v. 81, n. 1, p. 31–38, 2007.

GENT, E. **The Huge Promise of Transparent Solar Cells**: Turning the World's Glass Surfaces into Solar Panels. October 31, 2017. Available at: <https://singularityhub.com/2017/10/31/the-promise-of-transparent-solar-cells-turning-the-worlds-glass-surfaces-into-solar-panels>. Accessed on: 24 May 2018.

GOKSENLI, N.; AKBABA, M. Development of a new microcontroller based MPPT method for photovoltaic generators using Akbaba model with implementation and simulation. **Solar Energy**, v. 136, p. 622–628, 2016.

GREACEN, C.; GREEN, D. The role of bypass diodes in the failure of solar battery charging stations in Thailand, **Solar Energy Materials & Solar Cells**, v. 70, n. 2, p. 141–149, 2001.

GREEN, M. A.; HISHIKAWA, Y.; DUNLOP, E. D.; LEVI, D. H.; HOHL-EBINGER, J.; HO-BAILLIE, A. W. Y. **Solar cell efficiency tables (version 51)**. Prog. Photovolt. Res. Appl. 2018; v. 26, p. 3-12. https://doi.org/10.1002/pip.2978.

IEA. International Energy Agency. **Renewables 2017: A new era for solar power**. 2017. Available at: <https://www.iea.org/publications/renewables2017/>. Accessed on: 14 May 2018.

IPCC. Intergovernmental Panel on Climate Change. **Renewable Energy Sources and Climate Change Mitigation:** Summary for Policymakers and Technical Summary. Special Report. 2012. Available at: <https://www.ipcc.ch/pdf/special-reports/srren/SRREN_FD_SPM_final.pdf>. Accessed on: 19 May 2018.

ISHAQUE, K.; SALAM, Z.; A deterministic particle swarm optimization maximum power point tracker for photovoltaic system under partial shading condition, **IEEE Transactions on Industrial Electronics**., v. 60, n. 8, p. 3195–3206, Aug. 2013.

ISHAQUE, K.; SALAM, Z.; Amjad, M.; Mekhilef, S. An improved particle swarm optimization (PSO)–based MPPT for PV with reduced steady-state oscillation, **IEEE Transactions on Power Electronics**, v. 27, n. 8, p. 3627–3638, Aug. 2012.

KIMBALL, J. W.; KREIN, P. T. Discrete-Time Ripple Correlation Control for Maximum Power Point Tracking, **IEEE Transactions on Power Electronics**, v. 23, n. 5, p. 2353–2362, 2008.

LIAN, K. L.; JHANG, J. H.; Tian, I. S. A maximum power point tracking method based on perturb-and-observe combined with particle swarm optimization, **IEEE Photovoltaics**, vol. 4, no. 2, p. 626–633, Mar. 2014.

LYDEN, S.; HAQUE, M. E.; MAHMUD, M. A. Maximum Power Point Tracking Methods for PV Systems. *In*: ISLAM, M. R.; Rahman, F.; Xu, W. **Advances in Solar Power Plants**, Springer, p. 79-105, 2016.

MAO, M.; ZHANG, L.; DUAN, P.; DUAN, Q.; YANG, M. Grid-connected modular PV-Converter system with shuffled frog leaping algorithm based DMPPT controller. **Energy**, v. 143, p. 181–190, 2018.

MESSENGER, R. A.; VENTRE, J. **Photovoltaic Systems Engineering**. 3rd ed. CRC Press. Boca Raton, 2010.

NDIAYE, A.; KÉBÉ, C. M. F.; NDIAYE, P. A.; CHARKI, A.; KOBI, A.; SAMBOU, V. Impact of dust on the photovoltaic (PV) modules characteristics after an exposition year in Sahelian environment: The case of Senegal**. International Journal of Physical Sciences**, v. 8(21), n. 21, p. 1166–1173, 2013.

OCRAN, T. A.; Cao, J.; Cao, B.; Sun, X. Artificial neural network maximum power point tracker for solar electric vehicle, **Tsinghua Science and Technology**, v. 10, n. 2, p. 204–208, 2005.

OLIVEIRA JUNIOR, J. L. W. **Desenvolvimento de plataforma emuladora de turbina eólica para estudos de algoritmos de MPPT eólicos inteligentes.** Master thesis. Federal University of Ceará, Fortaleza, 2016.

OURWORLDINDATA. Our World in Data. **Renewables**. 2017. Available at: <https://ourworldindata.org/renewables>. Accessed on: 13 May 2018.

PATEL, H.; AGARWAL, V. Maximum power point tracking scheme for PV systems operating under partially shaded conditions, **IEEE Transactions on Industrial Electronics**, v. 55, n. 4, p. 1689–1698, 2008.

PINHO, J. T.; GALDINO, M. A. **Manual de Engenharia para Sistemas Fotovoltaicos**. Rio de Janeiro, 2014.

QUASCHNING, V.; HANITSCH, R. Numerical simulation of current-voltage characteristics of photovoltaic systems with shaded solar cells, *In*: **Solar Energy**, v. 56, n. 6, p. 513–520, 1996.

RAHMANI, R.; YUSOF, R. A new simple, fast and efficient algorithm for global optimization over continuous search-space problems: Radial Movement Optimization. **Applied Mathematics and Computation**, v. 248, p. 287–300, 2014.

SEYEDMAHMOUDIAN, M.; HORAN, B.; RAHMANI, R.; THAN OO, A. M.; STOJCEVSKI, A. Efficient photovoltaic system maximum power point tracking using a new technique. **Energies**, v. 9, n. 3, p. 1–18, 2016.

SEYEDMAHMOUDIAN, M.; RAHMANI, R.; MEKHILEF, S.; THAN OO, A. M.; STOJCEVSKI, A.; SOON, T. K.; GHANDHARI, A. S. Simulation and Hardware Implementation of New Maximum Power Point Tracking Technique for Partially Shaded PV System Using Hybrid DEPSO Method. **IEEE Transactions on Sustainable Energy**, v. 6, n. 3, p. 850–862, 2015.

SHUKLA, A. K.; SUDHAKAR, K.; BAREDAR, P. Recent advancement in BIPV product technologies: A review. *In*: **Energy and Buildings**, v. 140, p. 188-195, 2017. https://doi.org/10.1016/j.enbuild.2017.02.015.

SILVESTRE, S.; BORONAT, A.; CHOUDER, A. Study of bypass diodes configuration on PV modules. *In*: **Applied Energy**, v. 86, n. 9, p. 1632–1640, 2009. https://doi.org/10.1016/j.apenergy.2009.01.020.

SOLTANI, S.; KOUHANJANI, M. J. Fuzzy logic type-2 controller design for MPPT in photovoltaic system. **2017 Electrical Power Distribution Networks Conference**, EPDC 2017, p. 149–155, 2017.

SRI VASTAV, B. K.; NEMA, S.; SWARNKAR, P.; RAJESH, D. Automatic solar tracking system using DELTA PLC. *In*: **International Conference on Electrical Power and Energy Systems** (ICEPES). Bhopal, India, 2016. Available at: <https://www.researchgate.net/publication/316906193>. Accessed on: 21 May 2018.

SRIDHAR, R.; JEEVANANTHAN, S.; DASH, S. S.; VISHNURAM, P. A new maximum power tracking in PV system during partially shaded conditions based on shuffled frog leap algorithm. **Journal of Experimental and Theoretical Artificial Intelligence**, v. 29, n. 3, p. 481–493, 2017.

SULAIMAN, S. A.; HUSSAIN, H. H.; NIK LEH, N. S. H.; RAZALI, M. S. I. Effects of Dust on the Performance of PV Panels. *In*: **International Journal of Mechanical, Aerospace, Industrial, Mechatronic and Manufacturing Engineering**, v. 5, n. 10, p. 2028-2033, 2011. Available at: <http://citeseerx.ist.psu.edu/viewdoc/download?doi=10.1.1.986.5516&rep=rep1&type=pdf>. Accessed on: 22 May 2018.

SYAFARUDDIN; KARATEPE, E.; HIYAMA, T. Artificial neural network-polar coordinated fuzzy controller based maximum power point tracking control under partially shaded conditions. **IET Renewable Power Generation**, v. 3, n. 2, p. 239-253, 2009.

VANITHASRI, M.; BALAMURUGAN, R.; LAKSHMINARASIMMAN, L. Modified radial movement optimization (MRMO) technique for estimating the parameters of fuel cost function in thermal power plants. **Engineering Science and Technology, an International Journal**, v. 19, n. 4, p. 2035–2042, 2016.

VANITHASRI, M.; BALAMURUGAN, R.; LAKSHMINARASIMMAN, L. Radial movement optimization (RMO) technique for solving unit commitment problem in power systems. **Journal of Electrical Systems and Information Technology**, v. 16, n. 7, p. 1-11, 2017. http://dx.doi.org/10.1016/j.jesit.2017.05.003.

VILLALVA, M. G. **Conversor Eletrônico de Potência Trifásico para Sistema Fotovoltaico Conectado à Rede Elétrica**. PhD thesis. State University of Campinas, Campinas, 2010.

WABLE, S. S.; GANIGER, S. Design & Manufacturing of Solar Panels Cleaning System. *In*: **International Journal for Research in Applied Science & Engineering Technology** (IJRASET), v. 5, n. 7, p. 191-197, 2017. Available at: <https://www.ijraset.com/fileserve.php?FID=8733>. Accessed on: 22 May 2018.

WANG, U. **Perovskite Offers Shot at Cheaper Solar Energy**. The Wall Street Journal. 2014. Available at: <https://www.wsj.com/articles/perovskite-offers-shot-at-cheaper-solar-energy-1411937799>. Accessed on: 23 May 2018.

WORLDENERGY. World Energy. **Energy Resources: Marine**. 2017. Available at: <https://www.worldenergy.org/data/resources/resource/marine/>. Accessed on: 14 May 2018.

YINGLY SOLAR. **YGE 60 cell series datasheet**: YGE60CellSeries2013_EN_201301_V01. 2013.

ZAKI DIAB, A. A.; REZK, H. Global MPPT based on flower pollination and differential evolution algorithms to mitigate partial shading in building integrated PV system. **Solar Energy**, v. 157, p. 171–186, 2017.